6-2007

Critical Life Prediction Research on Boron-enhanced Ti-6Al-4V

Kevin A. Schwendiman

CRITICAL LIFE PREDICTION RESEARCH ON BORON-ENHANCED Ti-6Al-4V

THESIS

Kevin A. Schwendiman, First Lieutenant, USAF

AFIT/GAE/ENY/07-J24

DEPARTMENT OF THE AIR FORCE
AIR UNIVERSITY

AIR FORCE INSTITUTE OF TECHNOLOGY

Wright-Patterson Air Force Base, Ohio

The views expressed in this thesis are those of the author and do not reflect the official policy or position of the United States Air Force, Department of Defense, or the United States Government.

AFIT/GAE/ENY/07-J24

CRITICAL LIFE PREDICTION RESEARCH ON BORON-ENHANCED Ti-6Al-4V

THESIS

Presented to the Faculty

Department of Aeronautics and Astronautics

Graduate School of Engineering and Management

Air Force Institute of Technology

Air University

Air Education and Training Command

In Partial Fulfillment of the Requirements for the

Degree of Master of Science in Aeronautical Engineering

Kevin A. Schwendiman, BS

First Lieutenant, USAF

May 2007

AFIT/GAE/ENY/07-J24

CRITICAL LIFE PREDICTION RESEARCH ON BORON-ENHANCED Ti-6Al-4V

Kevin A. Schwendiman, BS
First Lieutenant, USAF

Approved:

Dr. Shankar Mall, Chairman	date
Dr. Vinod Jain	date
Dr. Stephan M. Russ	date

AFIT/GAE/ENY/07-J24

Abstract

Research on boron-enhanced Ti-6-4 has demonstrated the following improvements to the Ti-6-4 alloy: up to 40% increase in ultimate tensile strength, up to 30% increase in modulus/stiffness, while maintaining greater than 10% ductility at RT conditions. The increased properties are attributed to small additions of boron (≤1 wt %), which refine the microstructure and result in a small volume fraction (~6 vol %) of fine TiB whiskers. Previous research indicates potential for substantial improvements in fatigue, fatigue crack growth, and fracture toughness. However, uncertainty regarding these "second-tier" mechanical properties is currently limiting implementation of this class of titanium alloys. This study of fatigue variability of a powder-metallurgy, boron-enhanced Ti-6-4 alloy identifies the most prevalent damage mechanism and elucidates the impact on fatigue design limits. The alloy was produced via a unique prealloyed powder-metallurgy process. The powder mesh size used was -35, which equates to powder particles with a diameter of 500 μm and smaller. Specimens were ultimately machined from a rolled plate. The mean fatigue behavior compared favorably with available data on conventional Ti-6-4, both wrought and powder-metallurgy product forms. However, inclusions in the material were responsible for a few poor fatigue results, which ultimately govern the fatigue design limits. Variability assessment and fatigue crack growth analyses indicate that if the frequency and size of inclusions can be reduced, this material could become a more viable alternative for select turbine engine and aircraft applications.

Acknowledgments

Several people deserve my sincere gratitude for accepting and fulfilling roles to support me in completing this research project and realizing my ambition of achieving a master's degree while serving my country.

First, I am grateful to my thesis advisor, Dr. Stephan Russ, for his guidance, encouragement, and optimism throughout the course of this thesis effort. He has also been my military supervisor since I started my Air Force career at the Air Force Research Laboratory (AFRL) three years ago. Steve has invested a great deal of energy in helping me find my compass and niche in the workplace. I would, also, like to thank my faculty advisor, Dr. Shankar Mall, from the Air Force Institute of Technology (AFIT) for the education he provided to me for both my required course work and this endeavor.

At the Materials and Manufacturing Directorate (ML), many technicians, scientists, and professionals, both government employees as well as contractors from UDRI and UES, spent their valuable time explaining processes, procedures and analyses. Many of these persons seemingly endured trials of faith with the testing equipment, scheduling, and bringing me up to speed to be capable of this project. Special thanks go to Mr. Philip Blosser, Mr. Dale Osborne, Dr. Reji John, Dr. Andy Rosenberger, Dr. Sesh Tamirisa, Dr. Rollie Dutton, Dr. Chuck Ward, Dr. Dan Miracle and Dr. Jonathan Spowart. In addition, I need to thank Colonel Tim Sakulich, who although he is no longer Director at ML, made the funding for this project available through a program he started: the Company Grade Officer Initiative Fund (CGOI Fund). He started the CGOI fund because he wanted to develop the Air Force's newest officers. His investment has made a great difference in my career thus far.

The most important person during this project has been my sweetheart, my wife. She has shown great patience, affection, concern, and encouragement to me. Supporting my military career has been challenging for her at times but she has consistently reminded me that the pursuit of this degree sooner rather than later sets a great example for our family and emphasizes my dedication to serving my country. During my time as a part-time AFIT student, she has delivered and started raising our first child. They have been a great inspiration to me. They are my life.

Kevin A. Schwendiman

Table of Contents

List of Figures

Page

Page

Page

List of Tables

List of Symbols

Symbol	Explanation
a	crack length
a_f	final crack length
a_i *or* a_0	initial crack length
a-N	plot of crack length versus cycles
Avg	average
da	crack growth increment
da/dN	fatigue crack growth rate per cycle
B	specimen thickness
$C_1 - C_4$	constants for hyperbolic arctangent fatigue crack growth equation
E	elongation or ductility
E	Young's modulus
h	notch height of the compact tension specimen
H	half the average height of the compact tension specimen
2H	average height of the compact tension specimen
K	stress intensity
K_{max}	maximum stress intensity
K_{min}	minimum stress intensity
ΔK	stress intensity range
$\Delta K_{applied}$	applied stress intensity range
ΔK_{eff}	effective stress intensity range
N	cycle count

ΔN	step size in number of cycles
P	load
P_{max}	maximum load
P_{min}	minimum load
R	stress ratio
SD	standard deviation
UTS or σ_{uts}	ultimate tensile strength
W	distance between load line and back face of compact tension specimen
YS or σ_y	yield stress
x_0	distance between load line and front face of compact tension specimen

CRITICAL LIFE PREDICTION RESEARCH ON BORON-ENHANCED Ti-6Al-4V

I. Introduction

Background

Titanium alloys are considered a much younger structural material compared to steel or aluminum alloys. The first titanium alloys were commercially developed in the 1940s in the United States (Dowling, 1999:66). Attractive properties such as high specific strength and corrosion resistance have made titanium alloys mainstays in the aerospace industry. In addition, the aerospace industry has exploited the tailorability of titanium alloys utilizing chemistry and thermomechanical processing to arrive at desirable combinations of density, strength, corrosion resistance and high temperature stability, whereas such attempts with aluminum, steel or nickel-based superalloys have been insufficient. Production of titanium has remained expensive. However, the benefits of titanium in the material selection process have increasingly outweighed its economical shortcomings so much so that, percentage-wise, more and more titanium is being used in aerospace. By weight percentage, the range is from 7% in airframes to 36% in engines to up to 95% in the case of the entire Blackbird SR-71 (Peters and others, 2003:420).

Ti-6Al-4V (Ti64) is the most important and widely used titanium alloy in the aerospace industry. It can be readily welded, forged and machined, and is available in a wide variety of forms such as sheet, extrusions, wire, and rod. Applications range from

rocket motor cases, blades and disks for turbine engine fans and compressors, pumps, cryogenic parts, structural forgings and fasteners, actuators, and pressure vessels (Donachie, 2000:203-205).

Research on enhancing Ti64 through small additions of boron has been underway since 2000 at the Air Force Research Laboratory's (AFRL) Materials and Manufacturing Directorate (ML). Initial results on powder metallurgy produced Ti64+B demonstrated that strength and stiffness increases of 40% and 30%, respectively, were achievable (Tamirisakandala and others, 2004:63). More recently, Miracle and Tamirisakandala have reported Boron-related improvements of: up to 75% increase in ultimate tensile strength, up to 35% increase in modulus/stiffness, while maintaining greater than 10% ductility/elongation at room temperature (Presentation at "A Workshop on Titanium Alloys Modified with Boron", 2005). It is important to note that the initial results corresponded to boron compositions of 1.6 and 2.9 weight %, and the more recent data is for a composition with only 1.0 weight % boron. Compositions with greater than 1.5 weight % boron, the eutectic composition, lead to large titanium-boride (TiB) particles and/or whiskers, which severely degrade ductility. Small amounts of boron (≤1 weight %) refine the microstructure and augment microstructural stability, which leads to the property increases reported to date and offers anticipated improvements in fatigue life, fatigue crack growth, fracture toughness, and creep (Tamirisakandala and others, 2004:60). However, to date, little if any fatigue, fracture, or creep results have been generated on the compositions of interest, i.e. Ti64+1B.

Research on time related properties of fatigue, creep, crack propagation and temperature effects is currently the pre-eminent issue limiting implementation of these boron enhanced titanium alloys. The design community has expressed that the foremost need is to better understand the above-mentioned properties to better assess the potential service life of envisioned Ti-B components. Hence, a study of fatigue variability is essential to the technical progression and evolution of this material system.

This research provides much needed fatigue data and insight for making an informed decision about the input powder size of Ti64+1B. Financial reasons exist for selecting the coarsest powder possible for fabrication of components; coarser powder equates to lower cost. On the other hand, the mesh or input powder size also controls the size of any potential contaminants or inclusions that are introduced during the powder-making and sifting process:

> In spite of all precautions, it is impossible to obtain an inclusion-free powder. But, drawing a parallel with other systems, it is likely only large particles will degrade properties; those below a certain size will be innocuous. If the inclusions are small enough not to affect mechanical properties then they can be accepted. If they do degrade mechanical properties, four options suggest themselves: change to a more defect-tolerant alloy, manipulate the microstructure so that it becomes more accommodating to the foreign particles, remove the contaminants by cleaning, or define the extent to which properties are degraded and see if the levels are acceptable (Kelto and others, 1980:13).

Given these attributes of powder metallurgy, it is necessary to assess the possibly degrading effect of any contaminants upon the lower limit of the fatigue life and determine whether the Ti64+1B's degree of damage resistance is adequate for specific applications.

Furthermore, whenever dramatic tensile property improvements are reported, technical fears and suspicions abound concerning ductility, fatigue, and fracture

characteristics. In the case of Ti64+1B, many titanium experts would merely assume severe debits in the abovementioned material characteristics compared to the parent alloy and prematurely bury it in an alloy graveyard before acknowledging the remarkable grain refinement as a significant counterargument.

Problem Statement

Although the tensile property improvements of Ti64+1B over Ti64 are substantial, little is known as to how well the alloy can be expected to perform in fatigue critical applications. AFRL and a small number of industrial partners have begun characterizing the larger suite of mechanical properties, which govern useful life of components where Ti64+1B would potentially be considered. In that frame of mind, this thesis proposes a unique start by searching for answers to the following problems: How does the enhanced material compare to conventional Ti64? What mechanisms govern the variation in properties concerning the serviceable life? What can or can't be concluded about the presence of TiB particles in relation to the fatigue life? Is the material validated enough for more rigorous testing and an expanded spectrum of applications? Finally, what are the next steps in its development and implementation in the aerospace and other industrial sectors?

Research Objectives

The goal of the current research is to increase the understanding of variability in fatigue and identify failure mechanisms in a powder metallurgy version of Ti64+1B related to the effects of boron. More succinctly, the following research objectives were planned:

- Assess the variability in fatigue life at three stresses each representing a targeted range of life cycles and compare the behavior to more conventional Ti64,
- Identify the dominant failure mechanisms culminating in an adjusted lower limit prediction, and
- Offer recommendations/inputs to the material manufacturer concerning powder size and the control of variability effects.

Research Focus

The focus of this thesis is the study of fatigue variability of Ti64+1B alloy, manufactured via a powder metallurgy, to confirm the improvement in fatigue life over the parent Ti64 alloy, identify the mechanisms controlling the lower limit in fatigue behavior, and recommend a course of action to improve Ti64+1B's manufacturing and performance.

Methodology and Assumptions

The Ti64+1B material was requested by AFRL/ML from FMW Composites, Inc. in West Virginia and Crucible Research in Pennsylvania. These two companies, along with AFRL, are the major stakeholders in this research and have previously patented a powder metallurgy based method for obtaining high microstructural refinement in titanium alloys (International Patent application of Miracle and others). Gas-atomized Ti64+1B powder was hot-isostatically pressed (HIP) and then rolled to plate. Cylindrical dog-bone specimens for fatigue testing were machined from the rolled plate. Specifics about the patented powder production method and preparation of the rolled plate are provided in more detail in Chapter 2 and 3.

This thesis focuses exclusively on the Ti64+1B alloy. It should be noted that that boron additions to other Ti-based alloys, such as Ti-6Al-2Sn-4Zr-6Mo, Ti-5Al-2.5Sn, and Ti-22 Al-26Nb are being concurrently studied at AFRL and elsewhere. It is assumed that the resulting study on the effect of Boron enhancement on the Ti64 alloy will provide great insight that will impact the direction of the broader family of boron-modified titanium alloys being considered for a range of applications, spanning from cryogenic to high speed-high temperature. Additionally, the selected composition, Ti64 with one percent weight boron and processing route, represents the strongest candidate for study because of the amount of information known about its properties and microstructure.

For this fatigue variability study, the stress at which the fatigue testing was done was the independent variable. The stress ratio, R, was controlled at 0.1 and the test temperature was room temperature. Three stresses were selected targeting fatigue lives ranging from 10^4 to 10^7 cycles. The cycles-to-failure was the dependent variable. Breaking things down further into variability in life, this study was more than a simple independent variable with a few dependent variables:

> The existence of scatter in fatigue test results is common and deserving of considerable attention, since engineering design decisions must be based on recognition of statistical character of the fatigue process. The origins of test scatter are manifold. They include variations in testing environment, preparation of the specimen surface, alignment of the test machine, and a number of metallurgical variables (Hertzberg, 1983:462).

For a single stress with an outlying low-life result compared to a median result or high result, the composition and appearance of the fracture/failure initial sites in addition to the cause of the fracture were substantially different. Correlations were made between

the statistical character of the fatigue process and the various metallurgical variables during the study of fatigue variability and confirmed through a separate fatigue crack growth analysis.

Implications

Success in studying fatigue variability (in parallel with current tensile property variability studies) will inevitably lead to lighter weight airframe and engine components with improved performance, processability and affordability. A market of numerous Department of Defense and Industry programs are awaiting the results of this research to make decisions regarding whether investment in creation of a large material properties database and testing for a larger family of applications for the boron modified titanium alloys are justified.

Preview

A literature review, provided in the second chapter, includes a brief history of the research into boron additions to conventional titanium alloys as well as the recent work on compositions, processing, characterization, and properties that have culminated in the material used for this study. Fatigue life and crack growth prediction methods and an approach to variability analysis were provided to lay the foundation for interpreting the test results. The literature review discusses how previous researchers analyzed the same or similar materials with a specific look into the prevalent damage mechanisms and failure modes discovered during their testing and subsequent fractography and microscopy. Some insight is given into the current related research, programs and applications for the Ti64-Boron alloys.

Chapter 3, Procedures, explains how the Ti64-boron material was made and prepared for testing. The testing methods from tensile to fatigue and fatigue crack growth are explained in accordance with appropriate testing standards. The probability and statistical analysis methods, used to analyze the fatigue variability, are explained. Insight is given into metallography and fractography procedures.

Chapter 4, Results and Discussion, provides the tensile, fatigue (Stress-Life), and fatigue crack growth results including observed micrographs and fractographs. Possible trends and sources of variability are deduced based upon the fractography, EDS, and other proven methods. The variability analysis is presented here. The relevance and impact of the current investigation is discussed along with comparisons/contrasts with competing materials. Emphasis is placed upon reconciling the uncertainty in understanding the fatigue and fracture properties of Ti64 with boron.

Chapter 5, Conclusions, summarizes the key results and insights from this research project. Guidance/recommendations are provided for follow-on material development.

An Appendix, containing additional images and explanations from the fracture surfaces of specimens used in fatigue variability testing, is included at the very end of this thesis.

II. Literature Review

Interest in titanium and its alloys in general began in earnest in the late 1940s and early 1950s when the alloys became known for their potential as high strength-to-weight ratio, high temperature materials for aerospace applications including both airframe and engine components. Following on the heels of the aerospace sector, chemical and related industries began taking advantage of its corrosion resistance by the 1970s. In 1972, approximately 30 commercial alloys were available in mill product form. The Ti-6Al-4V (Ti64) alloy was and still is amongst the most favored compositions. This alloy exhibits good fabricability, high room temperature strength and moderate elevated temperature strength, but can be difficult to form (Collings, 1984:1-3).

Boron's Influence on Microstructures of Titanium Alloys

Ti-6Al-4V (Ti64), a near-α alloy, is a widely used alloy for aerospace applications partially because it combines the advantages of both α and β stabilizers in the alloy. Mechanical properties of $\alpha+\beta$ alloys can be controlled through thermomechanical processing and are used to affect the morphology of the α and β phases. The addition of aluminum (Al), a α stabilizer, provides solid-solution strengthening and raises the $\beta/(\alpha+\beta)$ transus. Vanadium (V), a β stabilizer, addition lowers the $\beta/(\alpha+\beta)$ transus (Collings, 1984: 3-4, 62-63).

In $(\alpha+\beta)$ alloys, an important microstructural parameter impacting the mechanical properties is the primary α size. When the primary α size is changed, yield stress,

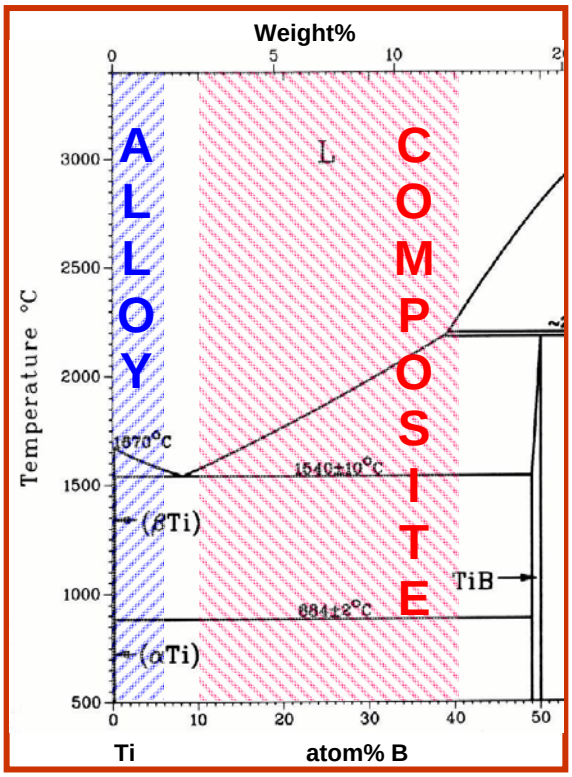

Figure 2.1: Phase diagram for boron modified Ti64 alloy and composite materials.

ductility and fatigue strength are affected. The primary α size is dependent upon the cooling rate from the β phase field and on the β grain size limiting the maximum dimensions of the primary α colony (Luetjering, 1998: 43-44). In the case of pre-alloyed Ti64+B alloys, for which the phase diagram is shown in Figure 2.1, "the presence of TiB not only restricts grain growth at high temperatures but also assists in the particle-stimulated nucleation of the α phase from the β phase" (Tamirisakandala, 2003:62-63). Further information from the Miracle et al. patent application states:

> First, the absence of grain growth after processing at very high temperatures, including temperatures above the beta transus, clearly shows that the borides effectively pin the grain boundaries. In the absence of borides, rapid grain coarsening occurs above the beta transus. Second, the presence of equiaxed grain morphology rather than a lamellar microstructure typically observed using other methods, even after cooling from temperatures above the beta transus, is a clear indication of the influence of borides on the phase transformation kinetics in titanium alloys. It is believed that fine second phase precipitates (titanium borides

in the present case) not only act as heterogeneous nucleation sites, but also generate large amount of dislocations in the matrix, which further stimulate heterogeneous nucleation of the alpha phase and lead to the formation of equiaxed grains.

Classification: Alloy vs. Composite

The microstructures and material behaviors depend on boron concentration and the processing path. Referring to Figure 2.1, the hypereutectic compositions can be classified as discontinuously reinforced titanium matrix composites (TMCs) because these compositions have significant volume fractions of TiB produced in them and the microstructures, processing and balance of properties are similar to other discontinuously reinforced TMCs. The hypoeutectic compositions can be classified as boron-modified titanium alloys because they have smaller (< 10 %) volume fractions of TiB and resemble particle strengthened titanium alloys (Miracle and others, introductory presentation at "A Workshop on Titanium Alloys Modified with Boron", 2005).

Historical Perspectives on Ti-B alloys

The earliest studies involving the alloying of titanium with boron occurred in the mid 1950s at the Armour Research Foundation and in the late 1950s at the Royal Aircraft Establishment. Their main objective was to increase stiffness. They found boron to be highly effective, with 0.5 weight % boron addition having an equivalent effect to adding 6.5 weight % aluminum. Little else was published between then and the 1980s, but it can be surmised that difficulties arose that degraded other important material properties (Miracle and others, Presentation).

In the early 1980s, Dynamet Technologies, Inc. focused on strengthening titanium alloys with reinforcements of titanium carbide (TiC) particles, titanium boride (TiB) or

titanium diboride (TiB_2). They used a cold and hot isostatic pressing (CHIP) process to compact their metal powders (Miracle, 2005: Workshop Presentation). Isostatic pressing uses uniformity of pressure from all directions with the absence of die wall-friction to achieve fully-dense compacts of nearly uniform grain structure and density regardless of shape (Kalpakjian and Schmid, 2001: 449-451).

Figure 2.2 provides a good description of Dynamet's CHIP process. The first step, blending, involves the selection of raw material powders at proper weight percents. Blending of the particulate reinforcement, in this case TiB, with a matrix material, Ti64, that is in either particulate or liquid form makes blended elemental Ti64-xB where x is the atomic weight percent. These powders are blended to achieve a desired final chemical composition. Cold isostatic pressing (CIP) follows. With CIP, the powders are pressed at room temperature using high pressures to make a green or pressed powder. In

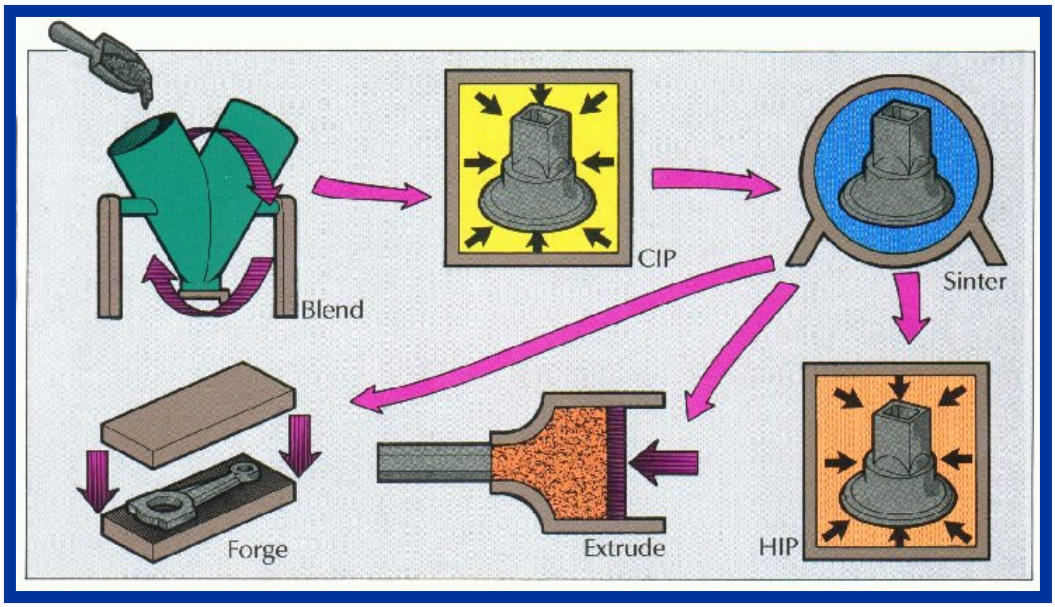

Figure 2.2: CHIP Process used by Dynamet Technologies, Inc. Ref: Dynamet website.

sintering, the preform is transferred to a vacuum furnace where it is processed at carefully controlled heat-up and cool-down rates and prescribed times and temperatures. Sintering

densifies the material and facilitates alloying via solid-state diffusion. Hot isostatic pressing (HIP) further densifies the material, closes small residual porosity, and improves the alloy's mechanical properties. Forging and extrusion are two options for subsequent processing (Dynamet Technology, Inc: Website).

Throughout the 1990s, Dynamet continued to develop its own Ti-B reinforced titanium alloys and introduced them to the government and industry through several patents. A picture of a TiB whisker from a 1990 Dynamet patent is shown in Figure 2.3. The mechanical properties of the most recent Ti-B alloy from Dynamet using the CHIP powder metallurgy process are approximately 965 MPa ultimate tensile strength, 896 MPa yield strength, and 14 % elongation (Abkowitz and Abkowitz, 2005 Workshop Presentation).

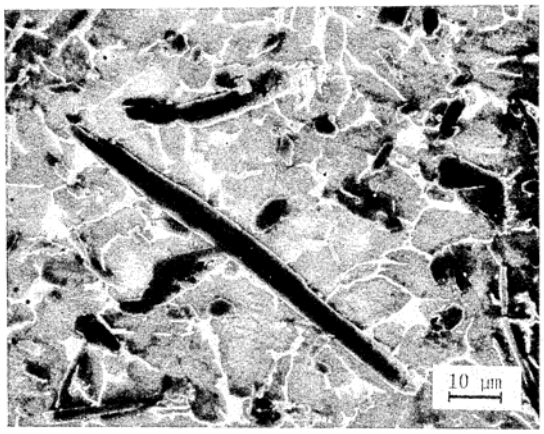

Figure 2.3: TiB Whisker shown Ti-6Al-4V matrix. Ref: Abkowitz and Abkowitz at 2005 Workshop, from Dynamet's U.S. Patent # 4,968,348 obtained on Nov. 6, 1990.

In the next major effort to push titanium technology, NASA collaborated with Boeing in the mid 1990s on the High Speed Civil Transport (HSCT) effort. The chief goal of the HSCT High Modulus Subtask was to improve the HSCT aircraft structural efficiency by developing an advance alloy with increased modulus while maintaining

acceptable durability, ductility and damage tolerance properties for wing spar caps. Titanium matrix composites with boron enhancement were one of many candidates. The principal matrix materials under consideration were lightweight alloys of aluminum, magnesium and titanium. The study included establishing the feasibility of extruded blended elemental powder metallurgy parts and extruded, large cast parts (Dillon, 1991).

The HSCT High Modulus subtask had three phases. During the first phase, several titanium alloys, including conventional Ti64, were cast into 3.0" diameter billets and extruded to 0.75" diameter. The results of the extrusion, depicted in Table 2.1, showed 10 % increase in both modulus and strength with no reduction in ductility. The high cycle fatigue performance of the alloys was also better than Ti-6Al-4V. Building upon this success, five second-phase alloys were selected and extruded to the same diameter. The five second-phase alloys extruded with little difficulty with smoother surface quality, good dimensions and lower flow stresses than baseline Ti64.

Table 2.1: Mechanical properties from first generation alloy data for High Speed Civil Transport Extrusion Subtask. Ref. *High Speed Research-Airframe Technology Report*.

Titanium Alloy	Heat Treatment	Modulus (GPa)	Ultimate Tensile Strength (MPa)	Yield Strength (MPa)	Elong. %	Fracture Toughness (MPa*sqrt(m))
Ti-6Al-4V (Baseline)	Annealed	110	1000	924	10	77
Ti-6Al-4V-0.5B	Annealed	124	1076	986	10	N/A
Ti-6Al-4V-0.5B	STA	126	1282	1186	7	N/A
Ti-21S (Baseline)	STA	101	1234	1179	7	N/A
Ti-21S-0.5B	STA	112	1276	1220	7	N/A
Ti-6-22-22 (Baseline)	Annealed	116	1096	1007	10	83
Ti-6-22-22-0.5B	Annealed	126	1219	1087	8.1	50
Ti-6-22-22-0.8B	Annealed	129	1271	1163	6.2	50
Ti-62S-0.5B	Annealed	135	1128	1075	6.1	41
Ti-62S-0.8B	Annealed	136	1129	1071	7.2	45
Ti-8Al-.05Pd -.01Y-0.05B	Annealed	139	1125	1113	0.3	24

Figure 2.4 shows two extrusions from one of the second phase alloys. The left extrusion in Figure 2.4 is from the third phase. Although one boron modified alloy (Ti-62S-0.6B), a compromise in boron content between the 0.5 and 0.8 weight percent alloys) survived to the third generation in the down-selection process, work was discontinued because of poor transverse mechanical properties, lower fatigue initiation characteristics, and difficulty machining. It was recommended that research continue only on Ti-6-22-22

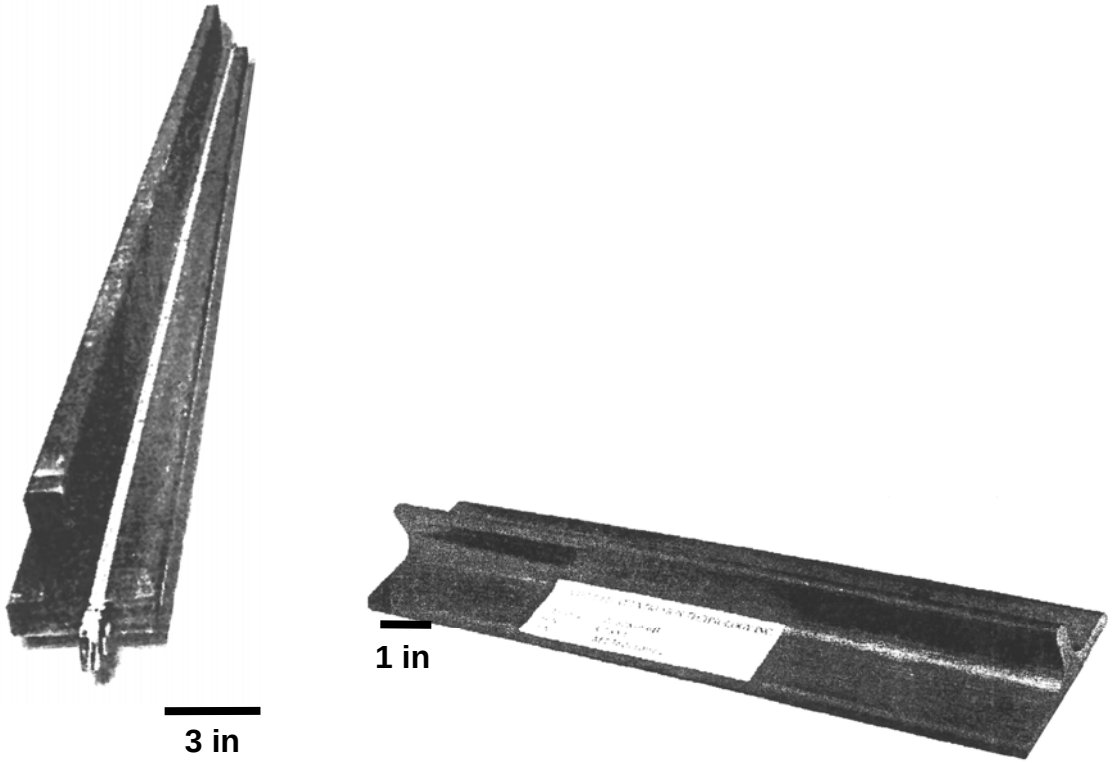

Figure 2.4: High Modulus Ti-6Al-2Fe-0.1Si-0.6B "T" Extrusions for HSCT program. Ref. Government Contract No. NASI-20220: High Speed Research-Airframe Technology report.

with the focus turning mostly to processing conditions; i.e. heat treatments and extrusion temperatures. Both alloys exhibited slower crack growth rates than baseline Ti-6Al-4V (Government Contract No. NASI-20220, High Speed Research-Airframe Technology Report, 1997: 3-5, 14, 26).

In the 1990s, Toyota Motor Corporation led a focused major effort to more affordably produce automotive components from titanium alloys. Despite superior performance in areas of high specific strength, fatigue, creep resistance and oxidation resistance at room temperature, auto makers were deterred by the high processing cost compared to steel alloys and inferior wear resistance, heat resistance, and rigidity. They

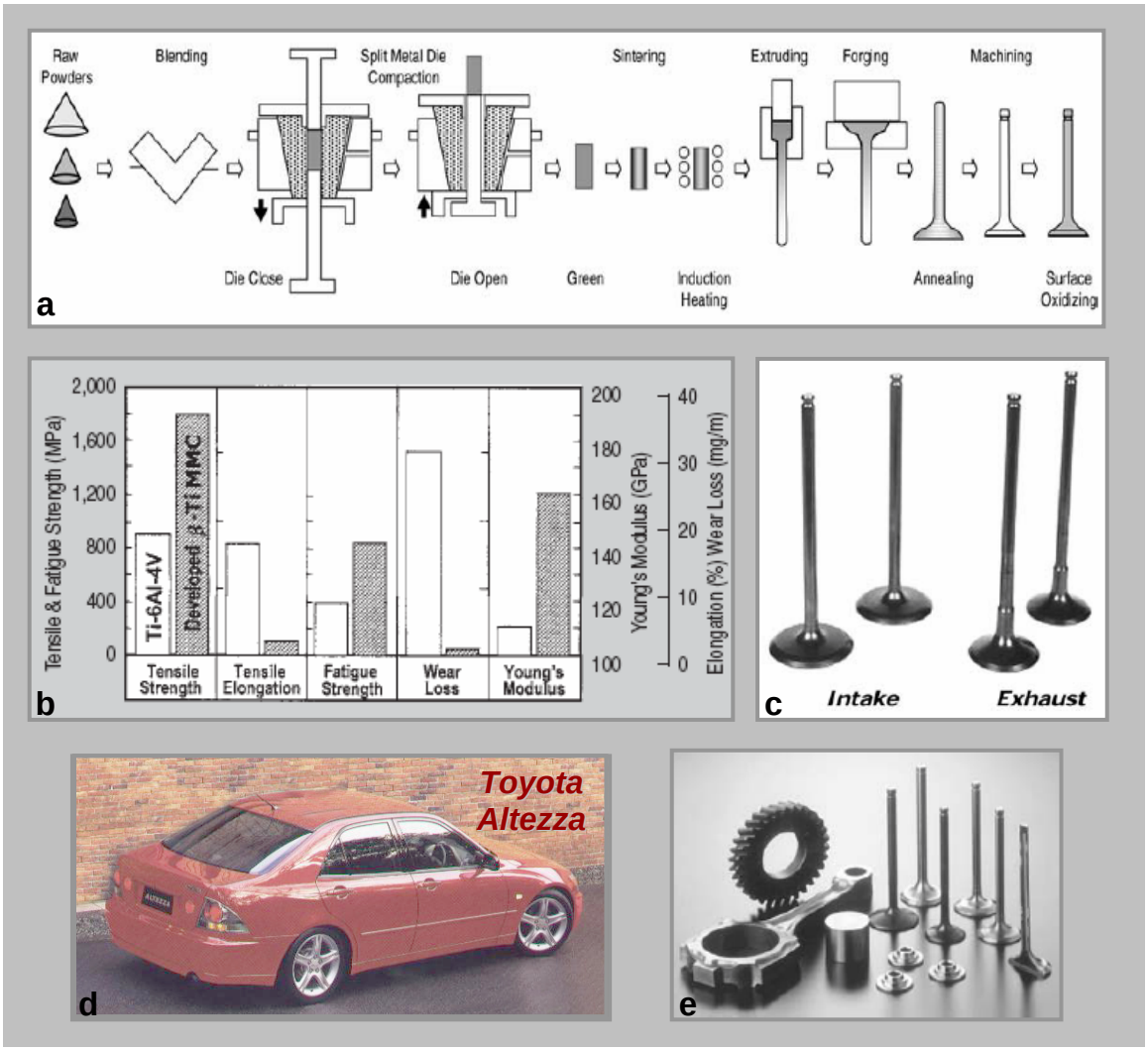

Figure 2.5: a. Processing steps for the blended elemental Ti-MMC valve production, b. mechanical properties of the developed TiB-particle-reinforced beta matrix Ti-MMC (20 vol. %TiB/Ti-7Mo-4Fe-2Al-2V), c. appearance of developed valves with TiB enhancement, d. Toyota Altezza vehicle, and e. various titanium metal matrix composite components for automobiles produce via blended elemental powder metallurgy. Ref: Tamiriskandala and others, 2003:60-61.

investigated processes for both continuously and discontinuously reinforced titanium alloys (i.e. Ti/SiC, Ti/TiC, and Ti/TiB_2). Based upon their findings, the blended elemental powder metallurgy process, depicted in Figure 2.5a, had the most promise for low cost manufacturing of titanium parts. The process allowed the use of low-cost titanium sponge. Toyota overcame the technical inferiorities with the optimum reinforcing compound of titanium monoboride (TiB), which far outperformed existing reinforcing compounds such as SiC, TiC, TiB_2, B_4C, TiN, SiN_4 and Al_3O_4. The optimal amount of TiB particle was determined to be 5 volume %. A comparison of the mechanical properties of the alloy with baseline Ti-6Al-4V is shown is Figure 2.5b. The composition with 20 volume % boron had a tensile strength doubling that of baseline Ti64, a decrease in elongation from 15 % to 2 %, doubled fatigue strength from ~400 MPa to ~800 MPa, and a stiffness increase from 110 to 160 GPa.

Toyota replaced its intake and exhaust valves (Figure 2.4c) and the results compared to steel proved to be 40% lighter also resulting in 16% lighter spring valve weight, 30% noise reduction, 20% camshaft driving torque reduction and an increase in maximum revolutions of 700rpm culminating in high performance and low fuel consumption. These parts, some of which are shown in Figures 2.5c and 2.5e, have been mass-produced by Toyota since 1998 and the first car to include the parts was the six-cylinder version of the Toyota Altezza (Figure 2.5d) in 1999 (Saito, 2004:33-35).

From 2000 to 2003, Miracle, Gorsse and Bhat investigated the effect of TiB within the Ti64 alloy matrix. They studied the relationship of mechanical properties to orientation, alignment and size of TiB reinforcements (Gorsse, 2003). They developed

processing maps for the blended powder metallurgy material and then compared the processing, properties and microstructure of the pre-alloyed material.

> Another way of making a discontinuously reinforced titanium-matrix composite is the in-situ method where the reinforcement is produced by formation or precipitation of a compound. This is the method used to make the pre-alloyed powder reinforced with titanium boride (TiB) and/or titanium carbide (TiC)…To produce the in-situ reinforced pre-alloyed titanium powder, boron and/or carbon are added to a titanium alloy melt. These elements have complete solubility in the liquid but limited solubility in the solid (Yolton, 2003: 56).

The research of Miracle, Gorsse and Bhat was strongly geared towards determining the feasibility of using either method for developing Ti-B components for military aerospace technology. They explored a wide range of processing paths (Figure 2.5) to achieve Ti-B

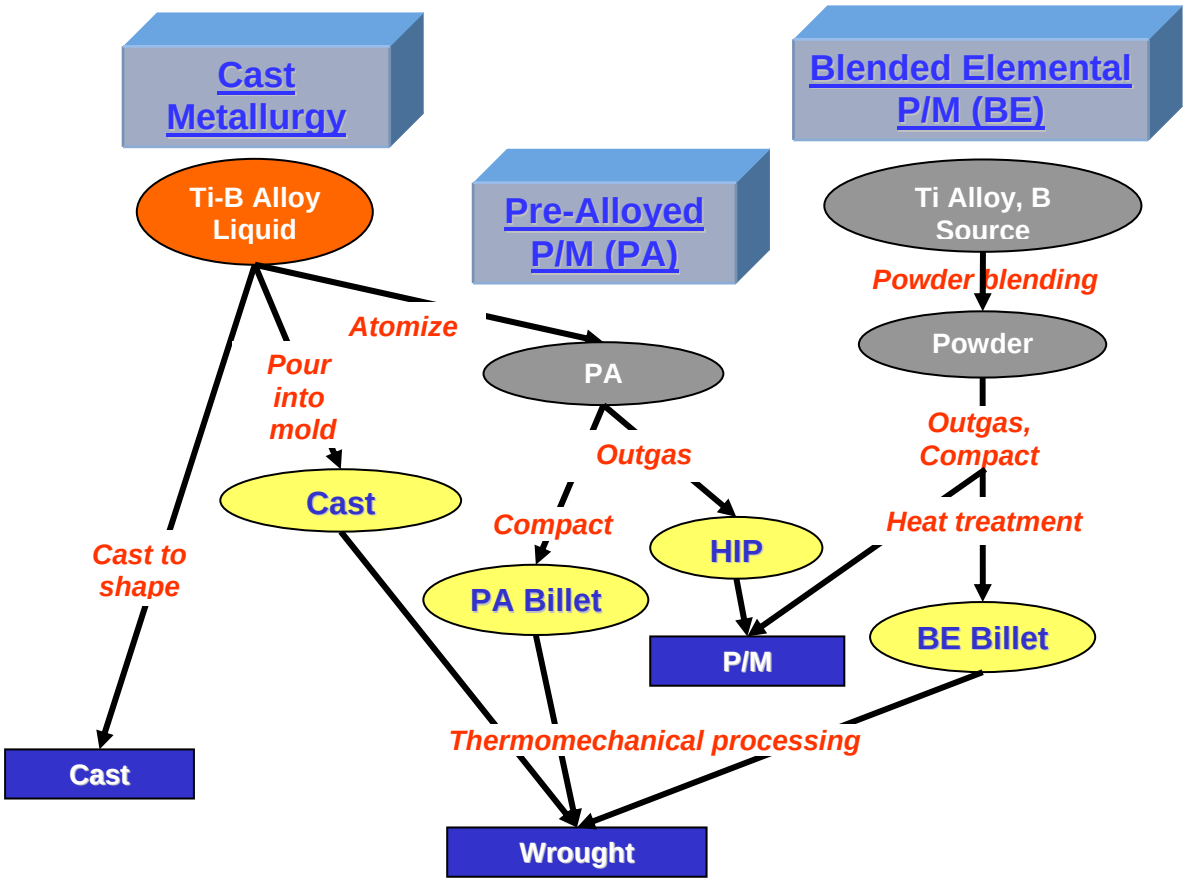

Figure 2.6: Flow Chart showing typical processing methods to produce Ti-B alloys.

alloyed products: cast, cast and wrought, pre-alloyed powder metallurgy, and blended elemental powder metallurgy. The blended elemental approach, though proven in the automotive industry, was insufficient for meeting the needs of aerospace where the requirements for microstructural refinement, ductility, fatigue resistance, and creep resistance are much more rigorous. Tamirisakandala compared the two powder metallurgy approaches and summarized their advantages:

> The PA approach has the advantage of producing finer scale microstructural features due to rapid solidification, but is limited to hypoeutectic compositions to avoid the formation of large, primary TiB in the liquid metal phase. The BE approach extends the compositions to obtain higher volume fractions of TiB without the formation of primary TiB since processing is conducted in the solid state. However, the BE approach is less economical due to additional processing steps required, and the microstructural features are usually coarser compared to PA powder material (Tamirisakandala and others, 2004: 61).

Crucible Research Corporation, Pittsburgh, PA, played a key role in the late 1990s in developing a unique powder metallurgy based approach that opened the door for developing boron modified titanium alloys within the aerospace industry. After demonstrating significant mechanical property improvements, they collaborated with FMW Composites, Inc. and the Air Force Research Lab, Materials and Manufacturing Directorate to further refine their method. An international patent was filed in April 2003 entitled, "Titanium Alloy Microstructural Refinement Method and High Temperature, High Strain Rate Superplastic Forming of Titanium Alloys."

Ti-B Alloys at AFRL

The Air Force Research Laboratory (AFRL) is currently leading the development of affordable boron-modified titanium alloys. With a team of suppliers, fabricators, end users, academia and Government partners, AFRL researchers have strived to demonstrate

approaches for cast, wrought, pre-alloyed powder metallurgy, rolled plate, and superplastic forming processes. Although only a small number of Ti-B products presently exist, AFRL programs have been assessing the excellent first-tier (i.e. strength and stiffness) and highly anticipated second tier (i.e. fatigue life) property improvements Ti-B alloys could offer to open the door for a wide variety of military applications.

The current approach has been to enhance titanium alloys through in-situ precipitation of TiB during processing and resolve the primary issues such as limited ductility, processing defects, fatigue and creep. Encouraging feasibility and basic property studies enabled this thesis within the vehicle of an AFRL, in-house funded program specifically targeting the effect of material defects upon fatigue life.

Scientists at FMW Composites, Inc. tackled the ductility limitation issue using a statistical design-of-experiment (DOE) analysis. Figure 2.7 compares the HIP processing with HIP+extrusion processing on the Ti64+1B alloy. For the first DOE, the HIP

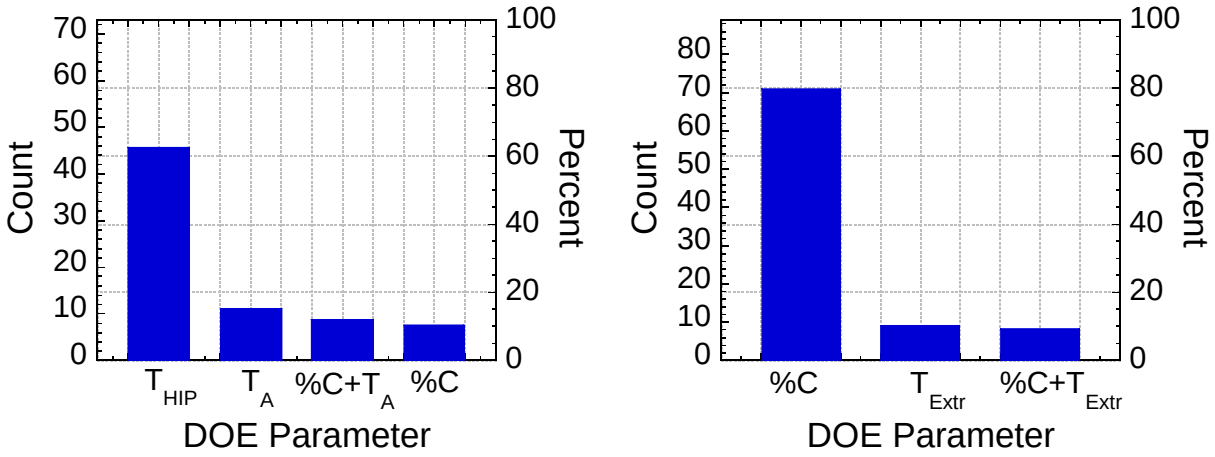

Figure 2.7: Left-DOE analysis for HIP process on Ti64+1B alloy and right-DOE analysis for extrusion process on Ti64+1B alloy.

temperature was the most sensitive parameter affecting the ductility. The result of the extrusion DOE was that carbon content most strongly controlled the ductility. It was

concluded based on these studies that the process conditions, in particular temperature and carbon content, were very important for ductility and quality control. This study was used to guide further process optimization, heat treatment, and composition conditions for boron-modified titanium alloys. Figure 2.8 demonstrates the achieved improvements in tensile properties, stiffness and ductility over non-enhanced Ti64 alloy. The optimal conditions for the plate rolling of Ti64+1B used for this thesis are not provided until later but the mechanical properties were similar.

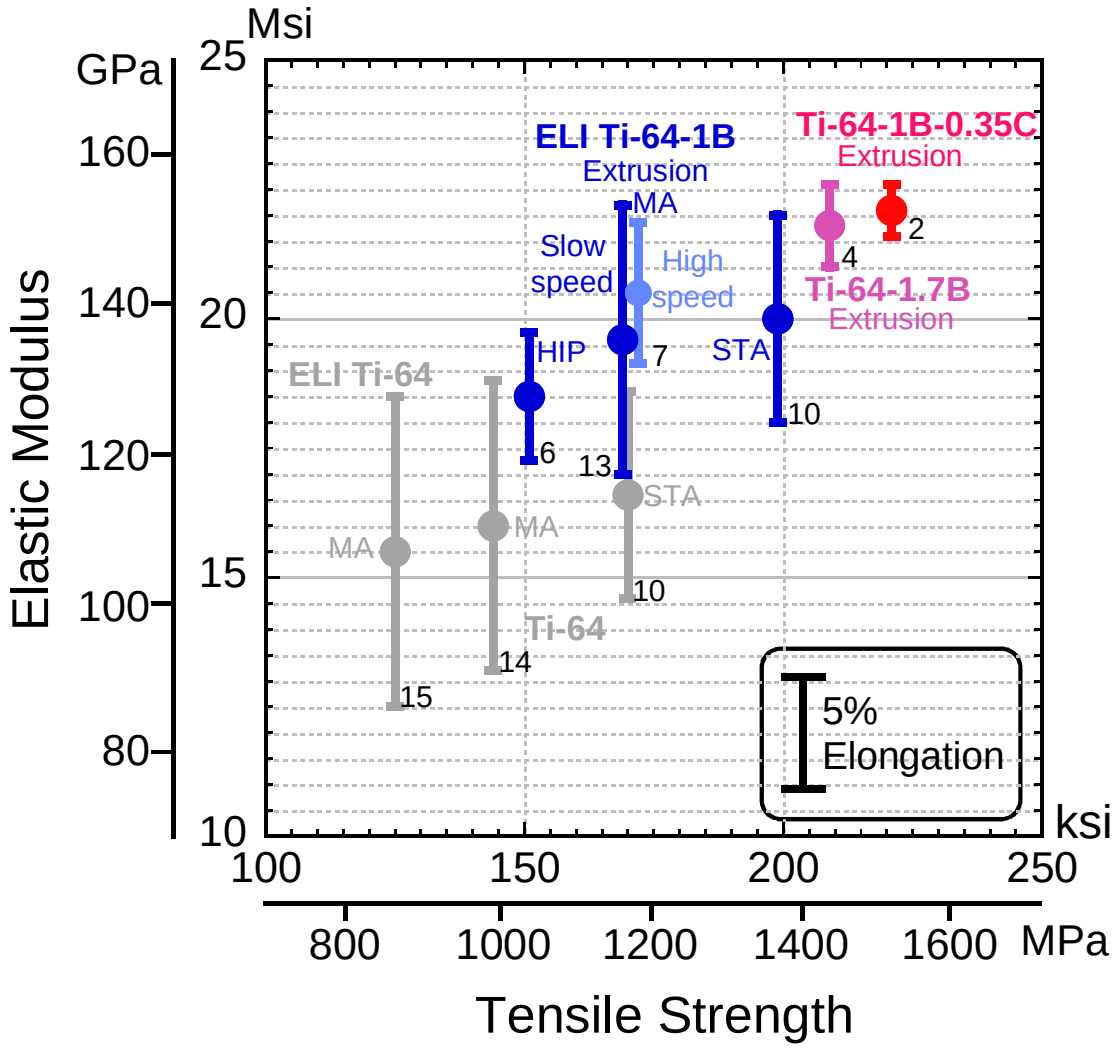

Figure 2.8: Mechanical properties of various TiB alloys tested at FMW Composites, Inc. ELI stands for extra low interstitial grade with characteristics of low oxygen and iron content.

Another area of emphasis within AFRL is the casting of boron-modified titanium alloys. Similar to powder metallurgy Ti-B alloys, significant performance enhancements can be achieved with a composition at or less than one weight percent boron. These improvements include grain refinement (Figure 2.9) and up to 30% strength and stiffness increases (Figures 2.10 and 2.11). The strength enhancements due to boron addition are maintained at elevated temperatures offering the potential for higher temperature capability (Figure 2.12). Based upon these results, a significant tradeoff exists between strength/stiffness and ductility when boron concentration is the variable being changed.

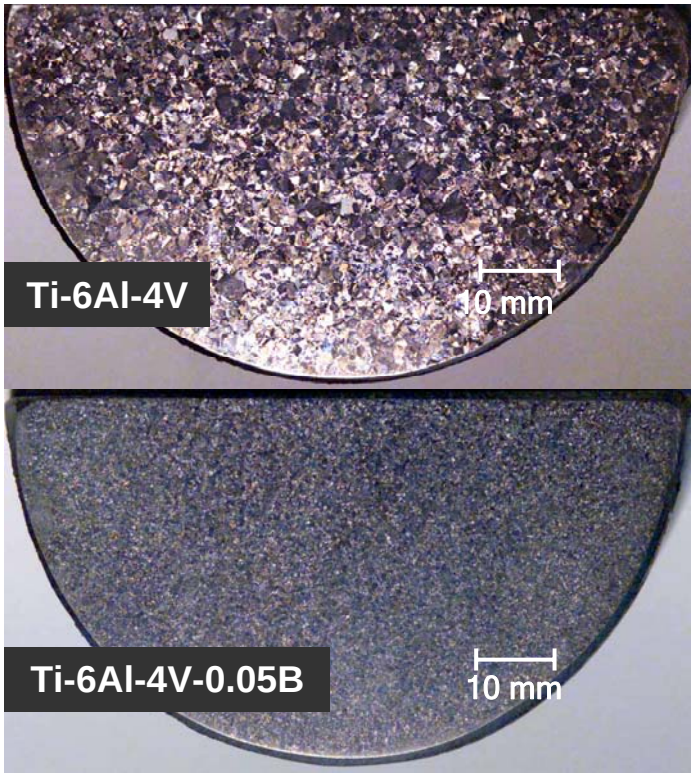

Figure 2.9: Grain refinement capability of boron demonstrated by comparison between un-enhanced (top) and enhanced (bottom) cast Ti-6Al-4V alloy.

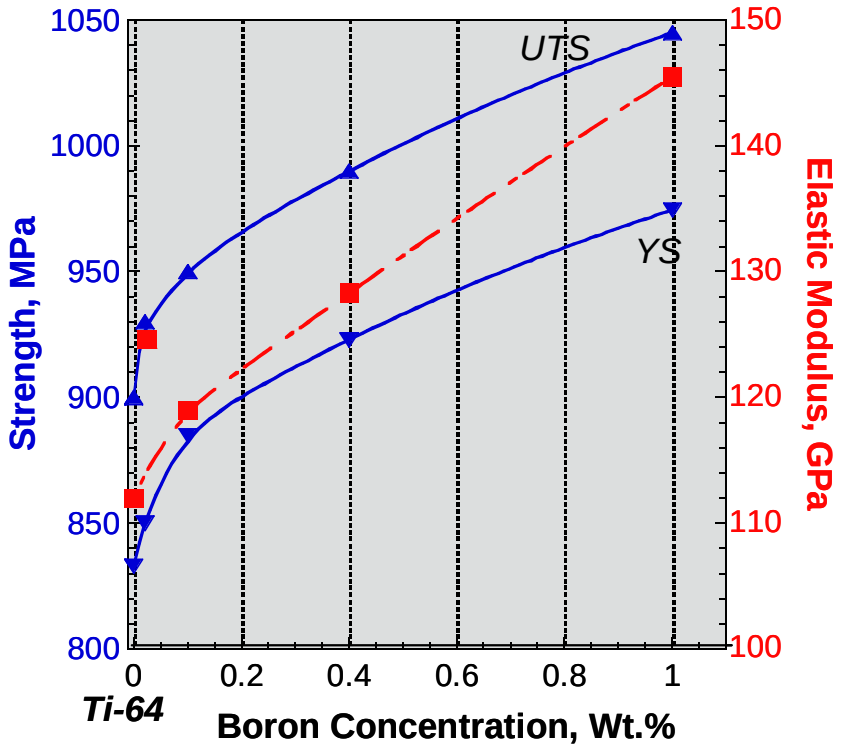

Figure 2.10: Mechanical properties of boron modified Ti-6Al-4V alloys at room temperature.

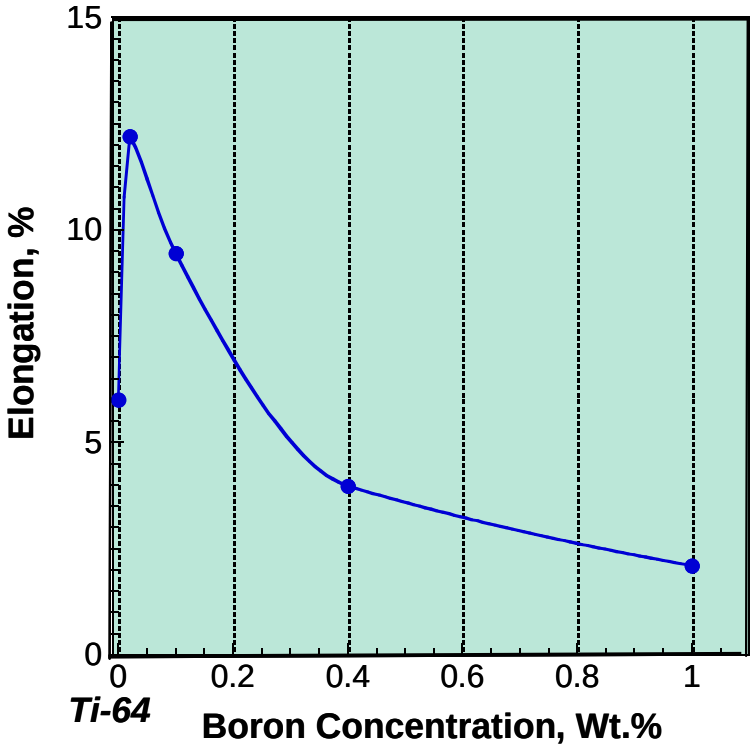

Figure 2.11: Ductility of boron modified Ti-6Al-4V alloys at room temperature.

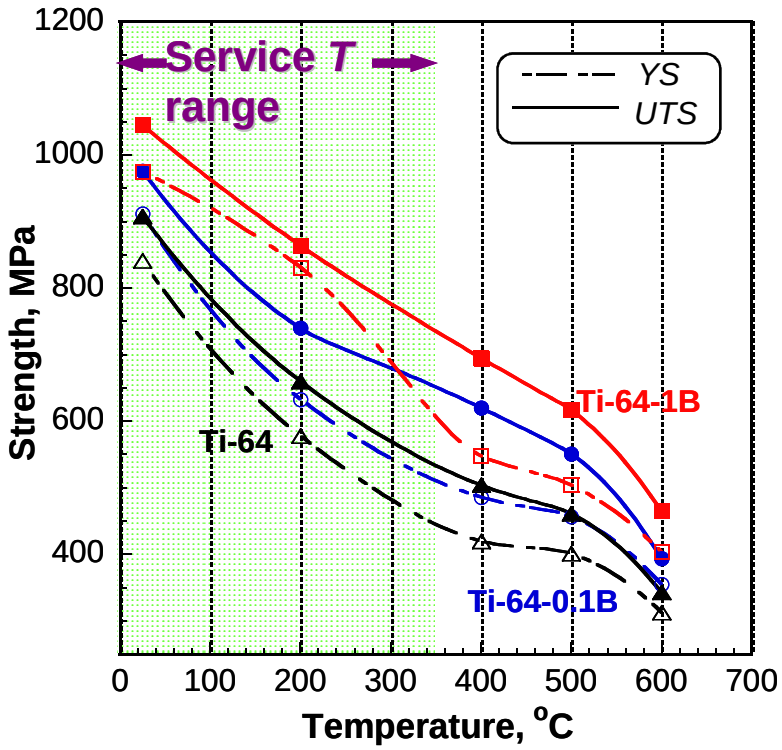

Figure 2.12: Mechanical Properties of boron modified Ti-6Al-4V alloys at elevated temperatures.

Pre-Alloyed Powder Metallurgy Processing

The production of in-situ Ti-B powder requires addition of boron during the titanium alloy melt. Boron is soluble in the liquid phase of titanium but has limited solubility in the solid α and β titanium phases. The TiB phase, in the form of reinforcing particulates and/or whiskers, is created during cooling from the liquid phase field. Conventional ingot metallurgy produces relatively coarse and unevenly distributed precipitates because of the slow cooling rate of large ingots. Atomization (Figure 2.13) is characterized by very high cooling rates, which results in the production of uniformly distributed, fine TiB particulates and/or whiskers (Yolton, 56-57). The atomization procedure is discussed in chapter 3 since it the same for the Ti64+1B material employed in this study.

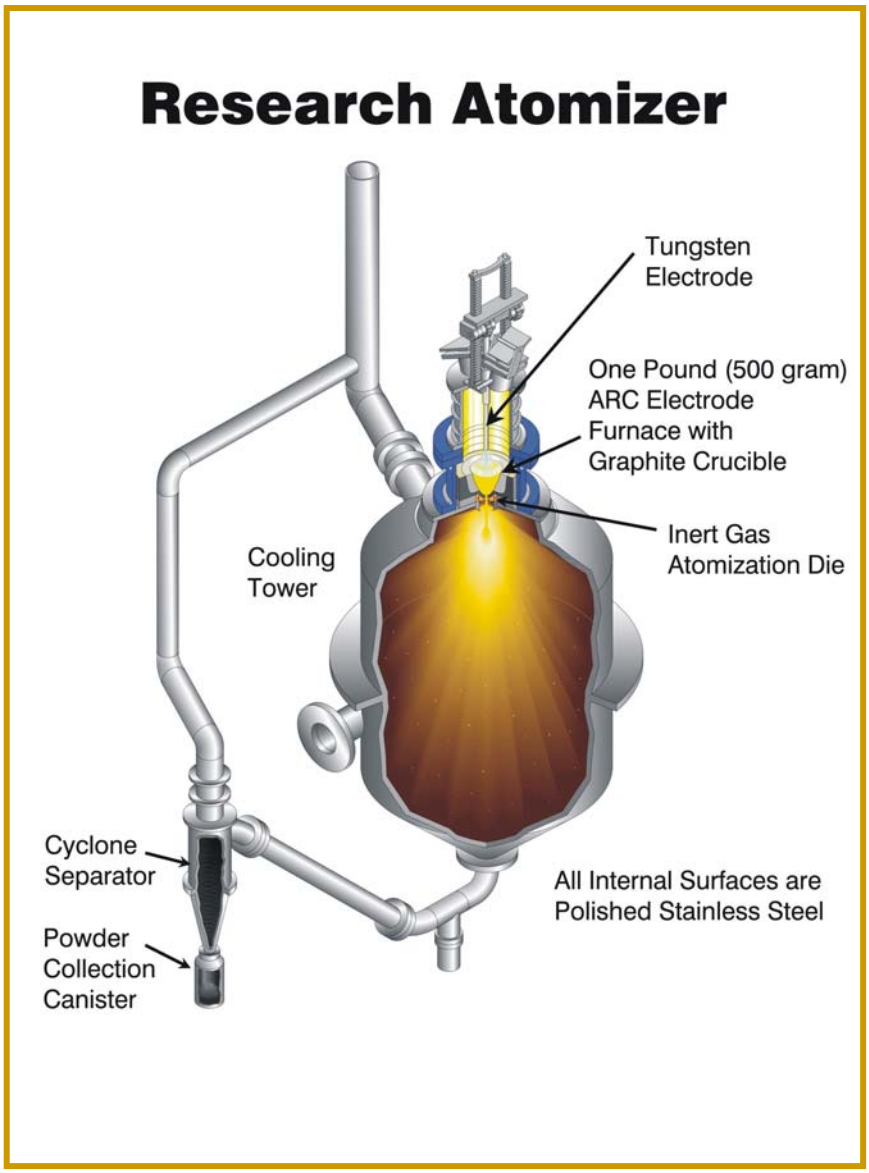

Figure 2.13: Model of 45kg bottom-pour titanium gas atomization unit used in pre-alloyed approach. Ref. Yolton.

Figures 2.14 and 2.15 are secondary images of Ti64+1B powder collected via scanning electron microscopy. This powder had a mesh size of -35. Accordingly, the spherically shaped powder shown in Figure 2.14 appears to have diameters not greater than 500 microns. In Figure 2.15, a closer look at one of the powder particles reveals that the TiB whiskers are equally disbursed in random orientations throughout the alloy (McEldowney, 2006).

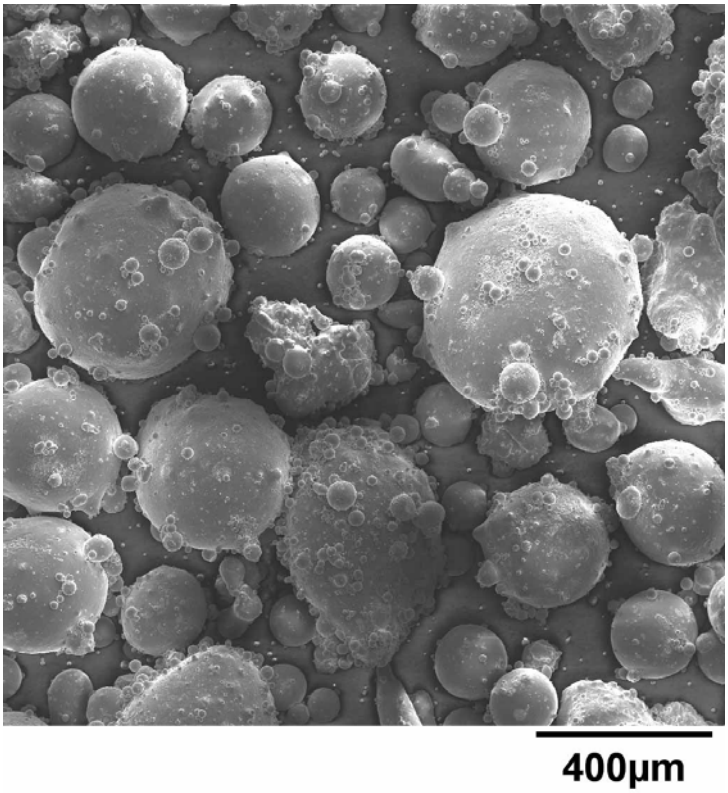

Figure 2.14: SEM micrograph of -35 mesh as atomized Ti-6Al-4V-1B powder. Ref: McEldowney, PHD Dissertation.

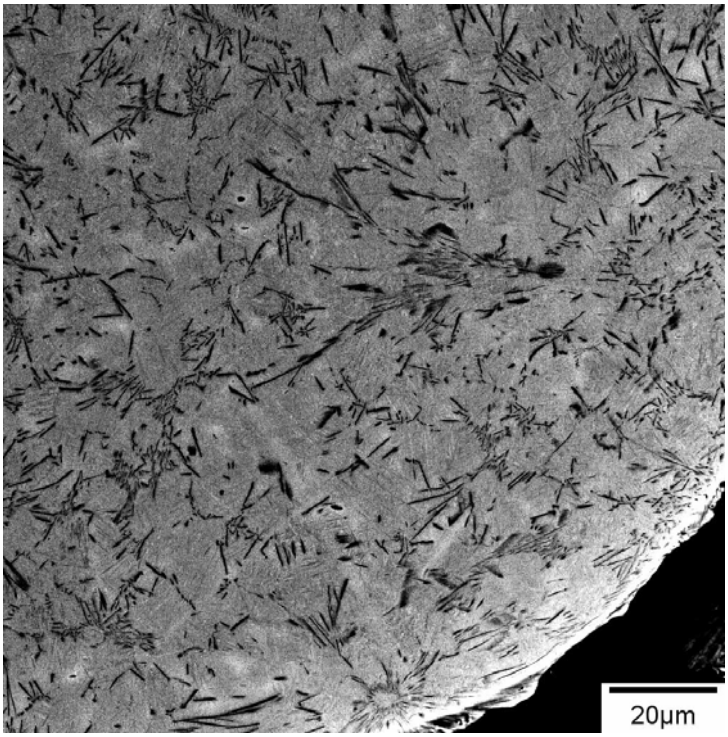

Figure 2.15: SEM micrograph of TiB whiskers from -35 mesh as atomized Ti-6Al-4V-1B powder. Ref: McEldowney, PHD Dissertation.

Thermomechanical Processing

Thermomechanical processing encompasses an entire sequence of operations. Factors that must be considered include the starting microstructure, the start and finish temperatures, the extent of deformation, and the rate at which deformation takes place. For achieving the final desired microstructure, two additional thermal factors are important for adjustment and control: the rate of cooling from the final working operation and the final heat treatment (Collings, 1984: 167-168).

Exploiting the influence of TiB precipitates to achieve microstructural refinement and possibly reduce the many timely thermomechanical processing steps has been hypothesized by Miracle and others. Titanium alloys usually require several steps for conventional ingot breakdown and billet conversion operations. Innovation reduces the lead time considerably and improves the affordability of titanium alloy products (2004: presentation). The specifics of the PA/PM approach are in Figure 2.15. The material described in prealloyed powder metallurgy journal articles by Tamirisakandala from AFRL (2003:60-63) and Yolton from Crucible Research Corportation (56-59) was Ti64-1.6B. The same process was used to make the pre-alloyed Ti64+1B powder studied in this thesis and is therefore discussed in material procedure of chapter 3.

HIP vs. Extrusion

A comparison of microstructures for HIP-ed versus extruded Ti64 and boron modified Ti64 alloys is in Figure 2.16. HIP and Extrusion are the two methods used to consolidate the titanium alloy powder. As HIP-ed powders have isostropic properties. Powders consolidated via extrusion are not isotropic. This is attributed to the alignment of Ti-B particles during the extrusion process. It results in enhanced mechanical

properties in the extrusion direction, which would be a desirable effect in select components (Yolton, 2003:58).

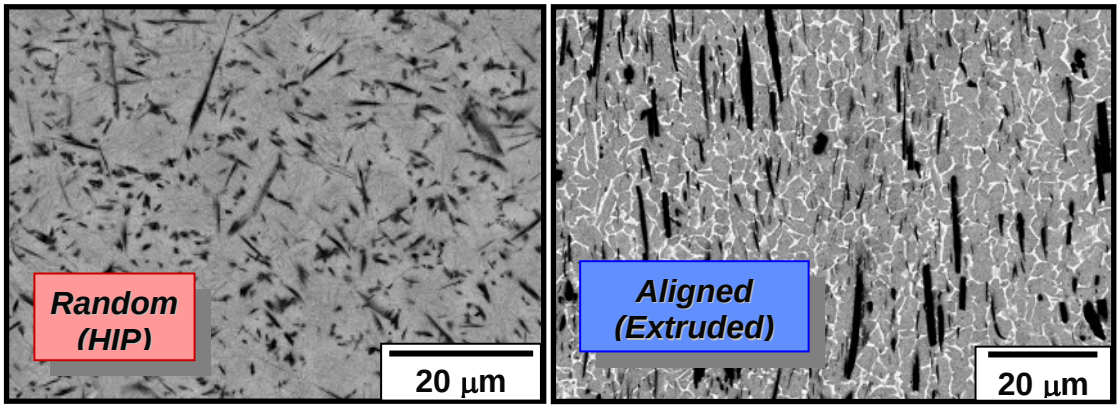

Figure 2.16: Microstructures of HIP and Extrusion Ti-6Al-4V-1.6B alloy. Ref: Tamirisakandala.

Mesh Size

The convention for sieve mesh size is well understood in industry but is worth reviewing here to understand the typical size of the powders screened for the consolidation/compaction process. This is especially important because it can limit the size of foreign matter that can contaminate the material. Inclusion initiation is the most frequent type of crack initiation mechanism found in fully dense prealloyed materials. Inclusions frequently come with sever debits in fatigue performance and can be limiting for fracture critical aerospace structural components made with the material under consideration, and overcoming inclusion problems can be costly (Eylon and others, 1980:94).

The mesh size for the materials evaluated by Miracle et al. was -35. Based on Table 2.2, the powder size was typically 500 microns and smaller. A similar powder size was employed in the material tested in this study.

Table 2.2: Standard sieve designations and nominal sieve opening sizes for fine chemicals. Ref: Aldrich's Catalog Handbook of Fine Chemicals, 2002: 1878.

Sieve Designation		Nominal Sieve Opening		
Standard	***Mesh***	***inches***	***mm***	***Microns***
500 μm	No. 35	0.0197	0.500	500
420 μm	No. 40	0.0165	0.420	420
354 μm	No. 45	0.0139	0.354	354
297 μm	No. 50	0.0117	0.297	297
250 μm	No. 60	0.0098	0.250	250
210 μm	No. 70	0.0083	0.210	210
177 μm	No. 80	0.0070	0.177	177
149 μm	No. 100	0.0059	0.149	149

Mechanical Properties

This section is designed to quickly review and compare the mechanical properties of various titanium alloys including and similar to Ti64 with boron modified versions of the same alloys. The tables are recreated from a few sources of data for TiB alloys. Tables 2.3 and 2.4 explain common heat treatments used on Ti64 and are borrowed from Donachie's guide (2000: 210-211).

Table 2.3: Ti64 mechanical properties vs. heat treatment. Ref: Donachie, 211.

Ti-6Al-4V: Mechanical Properties vs. Heat treatment				
Heat Treatment	Ultimate Tensile Strength MPa	Tensile Yield Strength MPa	Elongation %	Fracture Toughness MPa*sqrt(m)
Mill Anneal	1020	951	N/A	43
	930	869	15	N/A
	930	860	10	55
Solution Heat Treatment and Overaging (STOA)				
ELI	1000	895	12	60
STD	1000	938	N/A	47
Recrystallize Anneal				
ELI	930	860	10	83
STD	1000	931	N/A	56
Beta Anneal				
ELI	860	795	8	99
STD	990	910	11	95
Duplex Anneal				
ELI, forged	892	814	12	124
STD, plate	931	903	16	N/A
ELI, sheet	945	895	15	176
STD, bar	1014	903	17	N/A
ELI, bar	934	832	13	90
Beta, STOA				
ELI	938	860	11	134
STD	972	900	9	99
BETA STA, STD	1172	1069	8	N/A
Solution Treat and Age	1270	1181	16	N/A
	1186	1069	16	N/A
Solution Treat	1117	951	17	N/A

Table 2.4: Typical heat treatments for Ti64. Ref: Donachie, 210.

Ti-6Al-4V Heat Treatments		
Heat Treatment	Procedure	Comments
Stress Relief Annealing	2 to 4 h 595°C (1100°F), air cool	Relieves residual stresses from welding, forming, etc. This cycle only provides a partial stress relief. A full anneal must be used for full stress relief. Low strength, good ductility.
Full Annealing (Mil Annealing)	2 h, 735°C +/- 15°C (1355°F +/- 25°F), air cool	Most common heat treatment, has good overall property combinations. Low strength, good ductility.
Solution Heat Treatment and Overaging (STOA)	10 min, 940°C (1725°F), water quench, plus 4 h, 675°C (1245°F), air cool	Strength intermediated between annealed and solution heat treated and aged (STA), but improved ductility and damage tolerance compared to STA
Recrystallization Annealing	4 or more h, 925°C (1695°F), furnace cool to 760°C (1400°F) at 55°C (100°F)/h (or slower), cool to 480°C (900°F) at 370°C (700°F)/h (or faster), air cool	Usually used for ELI material. Strength comparable to above conditions, but improved damage tolerance (fracture toughness, stress-corrosion resistance, reduced crack growth rates). Strength lower for ELI material.
Beta Annealing	30 min., 1035°C (1895°F), air cool, plus 2 h 730°C (1345°F), air cool	Used to maximize damage tolerance properties. These properties are attained with a slight loss of ductility and a significant fatigue loss. A preliminary treatment follows such as annealing.
Duplex Annealing	10 min., 940°C (1725°F), air cool, plus 4 h 675°C (1245°F), air cool	Improved Damage Tolerance
Beta STOA	30 min, 1035°C (1895°F), water quench, plus 2 to 4 h, 675°C to 730°C (1245 to 1345°F), air cool	Similar to beta anneal with improvement in fatigue performance. May be preferable to beta anneal because of improved fatigue properties, but at a cost in damage tolerance properties.
Beta STA	30 min, 1035°C (1895°F), water quench, plus 4 h, 510°C to 680°C (950 to 1250°F),	N/A
Solution Treat and Age (STA)	10 min, 940°C (1725°F), water quench, plus 4 h, 510°C to 540°C (950 to 1000°F), air cool	Highest strength condition, but less ductility, stress corrosion resistance, and fracture toughness than annealed
Solution Treat (ST)	10 min, 940°C (1725°F), water quench	Used as an intermediate step for forming material ultimately to be used in the STA condition. Not to be used as a final condition due to instability.

Soboyejo et al. researched the effect of TiB whiskers in several alloys. Similar to the results in the HSCT program, strength increased appreciably with increasing boron content but was accompanied by severe debit to ductility (1995: 171).

Table 2.5: Mechanical properties of various in-situ boron modified titanium alloys after stabilization annealing at 704°C for 24 hours and tensile testing at room temperature. Ref: Soboyejo, 1995: 171.

Alloy	Yield Stress	Modulus	Elongation
	MPa	GPa	%
Ti-6Al-0.5B	1055	128	8.1
Ti-6Al-1.4V-0.5B	1000	121	7.1
Ti-6Al-1.0B	1158	137	1.5
Ti-7.5Al-4V-0.5B	1227	117	7.2
Ti-6Al-4V (Baseline)	986	110	11.0

AFRL's research for comparing the properties of prealloyed and blended elemental powder metallurgy yielded important data concerning the effect of Ti-B on titanium alloys. Two types of TiB showed up in the prealloyed material: (1) eutectic TiB of approximately 8 volume % ranging in width from 1 to 2 microns with aspect ratios from 8 to 12 and (2) nanometer TiB of about 2 volume % with average length of 500 nm and average diameter of 50 nm. The matrix for the prealloyed powder had a fine grained (3 micron) equiaxed alpha microstructure. The prealloyed powder had 1.6 weight % boron. In contrast, the blended elemental material had TiB particles occupying over 20 volume % having lengths from 20 to 50 microns, aspect ratios from 5 to 15, and a relatively coarse-grained microstructure. The blended elemental powder also had a higher boron content of 2.9% (Tamirisakandala: 2003: 62-63). The data from that research is shown in Figure 2.17.

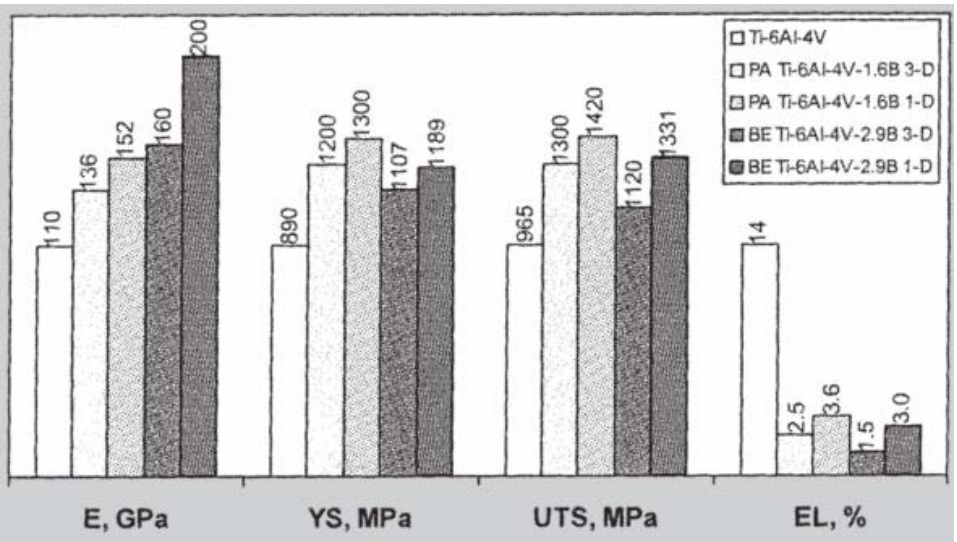

Figure 2.17: Mechanical properties of Ti64-xB alloys at room temperature. Ref: Tamirisakandala.

Fatigue: Stress-Life (S-N) Variability

Variability refers to the degree of scatter within a set of data. The variability in fatigue life for some materials can be substantial and the design based upon the lower limit for the data may give an inaccurate picture of the material's capability. Unfortunately, the fatigue S-N approach doesn't distinguish between initiation and propagation, the effects of which have been historically avoided by using a variety of empirical modeling approaches. This approach offers limited insight into the damage mechanisms (Bannantine and others, 1990:1-2, 235). Multiple methods are employed in this research including a much more in depth look at fatigue crack growth behavior to elucidate the variability results obtained using the stress-life approach.

The first set of S-N data from the ASM Metals Handbook (Figure 2.18) compares fatigue ranges of ingot metallurgy and powder metallurgy products. The prealloyed (PA) powder metallurgy band will be used for comparison with the S-N data for the Ti64+1B alloy studied in this thesis. The PA data shows up in Chapter 3 as a digitized envelope.

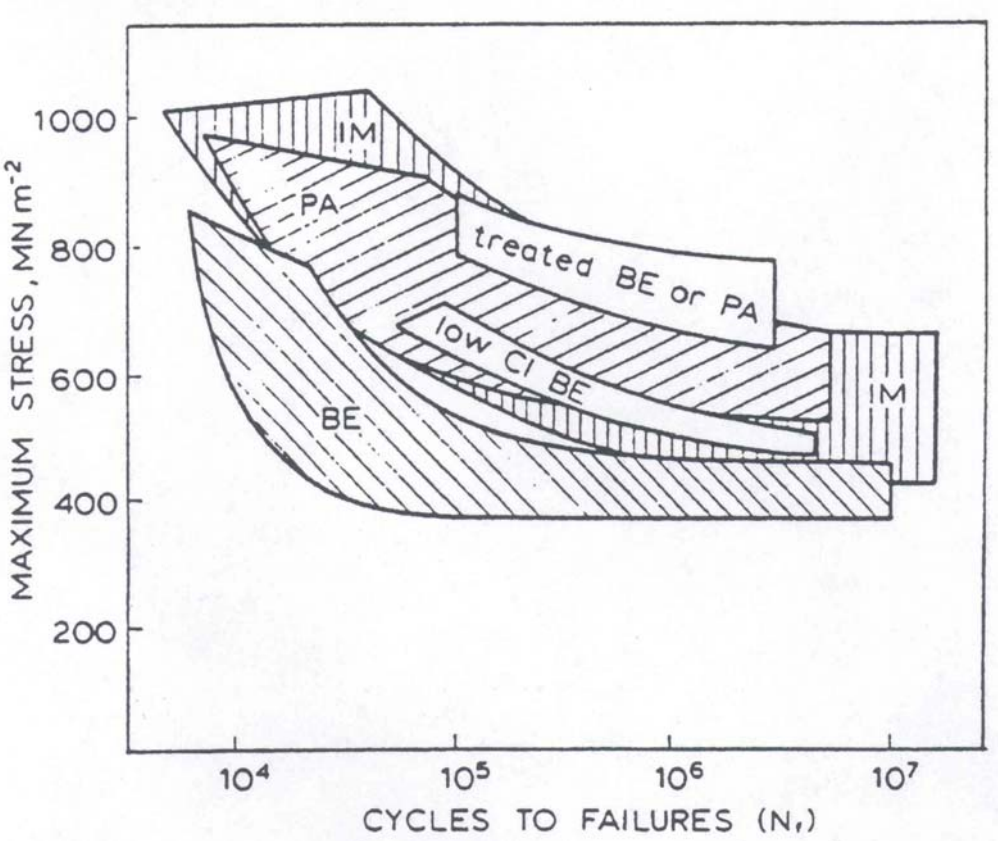

Figure 2.18: Comparison of room temperature fatigue life scatter bands of blended elemental (BE) and prealloyed (PA) Ti-6Al-4V compacts to that of mill annealed ingot metallurgy alloy. Ref: Froes and Eylon.

The next set of fatigue data (Figure 2.19) comes from a large data base on Ti64 owned by the US Air Force (USAF) that was delivered in 2004 by the prime contractor, the University of Dayton Research Institute (UDRI), to the USAF as the result of a major high-cycle fatigue (HCF) program.

In the mid-1990s, several HCF related incidents occurred within the USAF fighter fleet resulting in engine failures and, on occasion, grounding of the fleet. Operational readiness was severely affected at times by these events so a team was formed to uncover the root causes and suggest solutions. Hence, HCF became a major focus for USAF research. A portion of the program went to the Air Force Research Lab's (AFRL)

Materials and Manufacturing Directorate (ML) over a six year period and was designed to solve problems specifically related to material capability under HCF loading

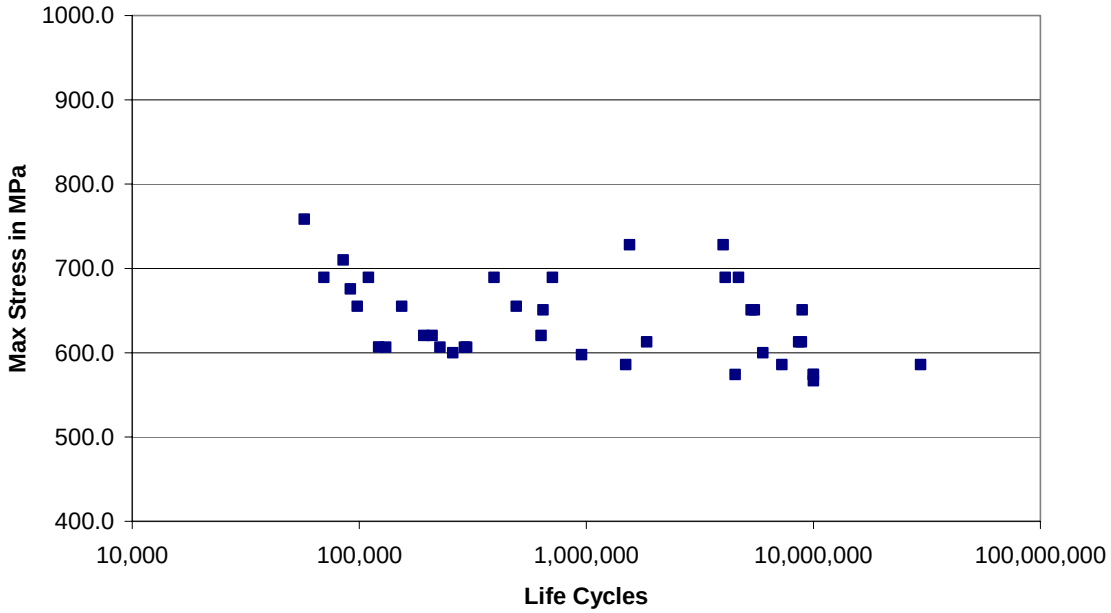

Figure 2.19: HCF program S-N Data with R=0.1and room temperature. Ref: Gallagher and Nicholas et al.

conditions. One of the earliest decisions in the program was the materials to evaluate. The engine industry was calling for a model material representative for a broad material class that had a large existing database. Ti64 was one of the primary alloy selected (Ti-17 was the other) because it was commonly used in engine fan and compressor components throughout the industry. The testing was conducted mostly at room temperature. All participants made use of a common material to minimize variation due to material. The approaches taken considered both total life and fracture mechanics methods (Gallagher and Nicholas, 2004:1-4). The data from the HCF, combined with the ASM handbook data, provide a reasonable foundation against which the Ti64+1B results from this research can be compared and evaluated for benefit to military and industrial applications.

Common Practice of Design for Worst Case Scenario

It has become common practice to manage the life of a military fleet on the basis of the statistically expected behavior (Figure 2.20) of the fleet's worst case vehicles:

> This is a well justified response to the fear of failure of the individual assets, but this approach has often imposed considerable conservatism in terms of initial design, deployment, and operation of systems. A typical asset management process… is rooted in a basic knowledge of initial design, prior use and maintenance, and relatively infrequent non-destructive inspections for damage to the material. To assure safety and reliability, an individual system is approved for continued service only if there is an extremely low (acceptable) probability of failure, wherein failure may be defined as the inability to perform anticipated future missions. Since the systems are managed largely on the worst-case scenario, the vast majority of the retiring assets may be expected to have a substantial amount of remaining (unused) lifetime or capability (Christodoulou and Larsen, 2005: 3).

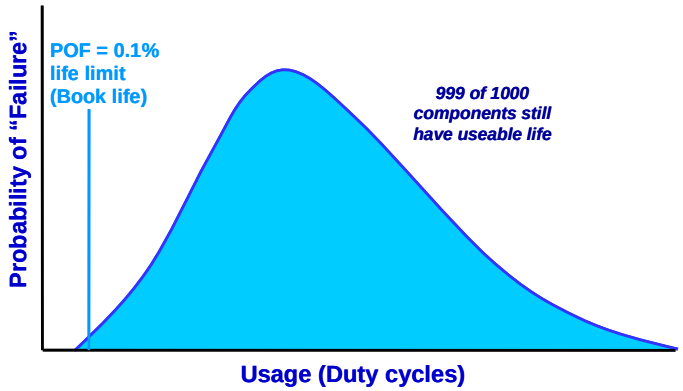

Figure 2.20: Current safe life approach used for management of fracture critical components in military turbine engines and aircraft—based upon worst case scenario. Ref: Christodoulou and Larsen.

Fatigue Variability Analysis

For a safe and efficient life prediction and life management of components, it is essential to understand the basis for variability in life from a physical standpoint. The traditional empirical approach for prediction of fatigue life does not explicitly treat variability. The variability of data for the HCF program shown in figure 2.29, for example, demonstrates at least two orders of magnitude between the best and worst test results at any given stress level. A more physically based life prediction methodology is

warranted (Jha and others (AIP), 2004:1955). As evidenced previously with the USAF's multiyear HCF program, the trend in the turbine engine and aircraft industries has been to improve the service lives of components.

Lognormal probability density functions (PDF) are commonly used to describe the fatigue variability of a material system. Attempts tracking the variability in life through the size distribution of a relevant feature in the microstructure were believed to be governed by crack growth life. These life calculations were based on an estimated crack size equivalent to that of a relevant microstructural feature and growth of that crack, until fracture. Variability in life was shown to only be controlled by a single mechanism. Therefore, the probability-of-failure (POF) plot was represented by only one cumulative probability distribution function (CPDF). It has been demonstrated that, when there are multiple mechanisms of failure, the CPDF result can be shown as the superposition of two or more mechanisms (Jha and others, 2003:1637-1638). This approach has considerable potential for life extension. Examples would be separating out the two mechanisms of surface and subsurface failures or in the case of this thesis, inclusion-initiated failure and non-inclusion-initiated failure, either of which could occur at the surface or in the subsurface. An inclusion-based failure at the surface would be extremely detrimental.

In Figure 2.21, the mean fatigue life behavior and life variability are depicted for the Ti-6Al-2Sn-4Zr-6Mo (Ti6246) alloy (Jha and others, 2003: 1638). The mean life and variability increased as much as two orders of magnitude with decreasing stress level. Upon arbitrary extrapolation of the fatigue data to a probability of 0.1 %, it was found that the predicted lives were much lower with decreasing stress than expected. This

underscored the importance of adopting a more physically based approach to fatigue life prediction (Jha and others (AIP), 2004: 1956). The probability of failure with respect to the selected stress levels for the Ti6246 alloy is shown in Figure 2.22.

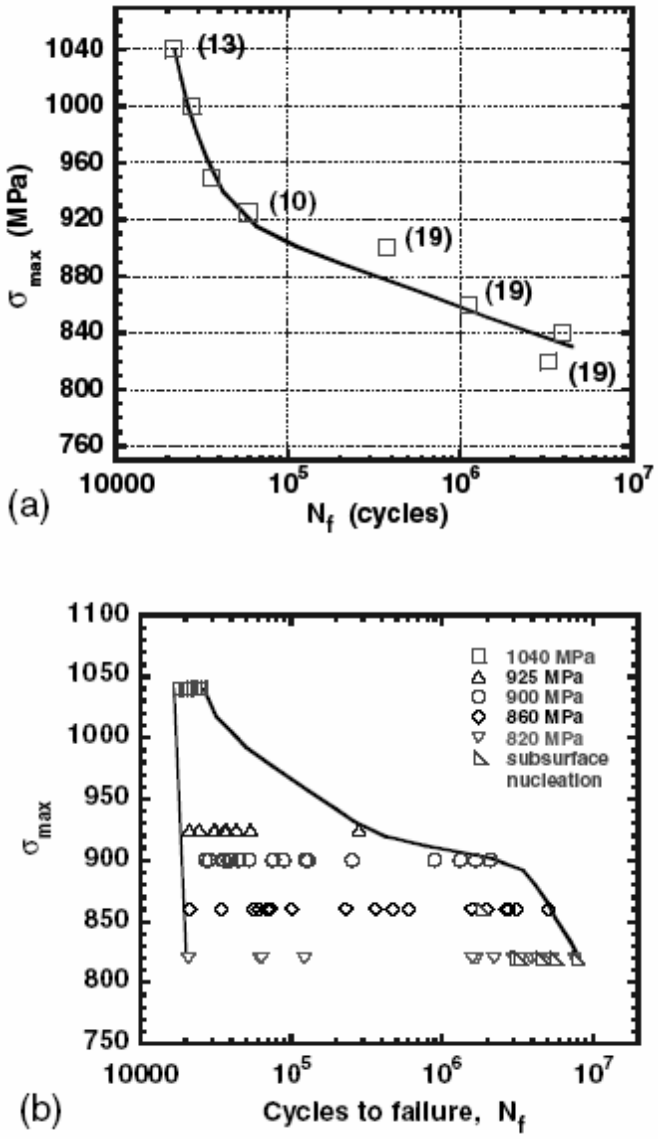

Figure 2.21: Fatigue life behavior of Ti-6-2-4-6: (a) mean lives, and (b) life variability. Ref: Jha and others, 2003.

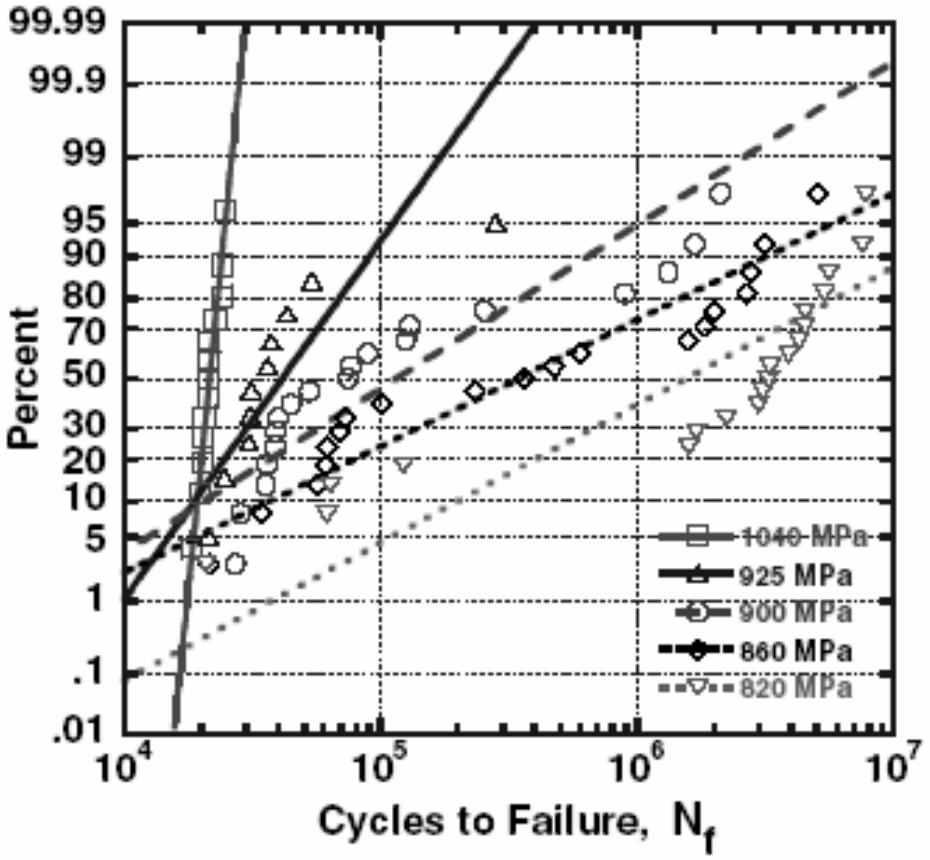

Figure 2.22: Ti6246 probability of failure plots at selected stresses. Ref: Jha and others, 2003.

In order to validate the existence of multiple damage mechanisms, Jha et al. separated the combined probability of failure plots (Figure 2.22) into separate plots for the three lowest stress levels and observed a step like behavior (Figure 2.23). A straight line for the highest stress level, 1040 MPa, was not plotted because it indicated only single mode of failure.

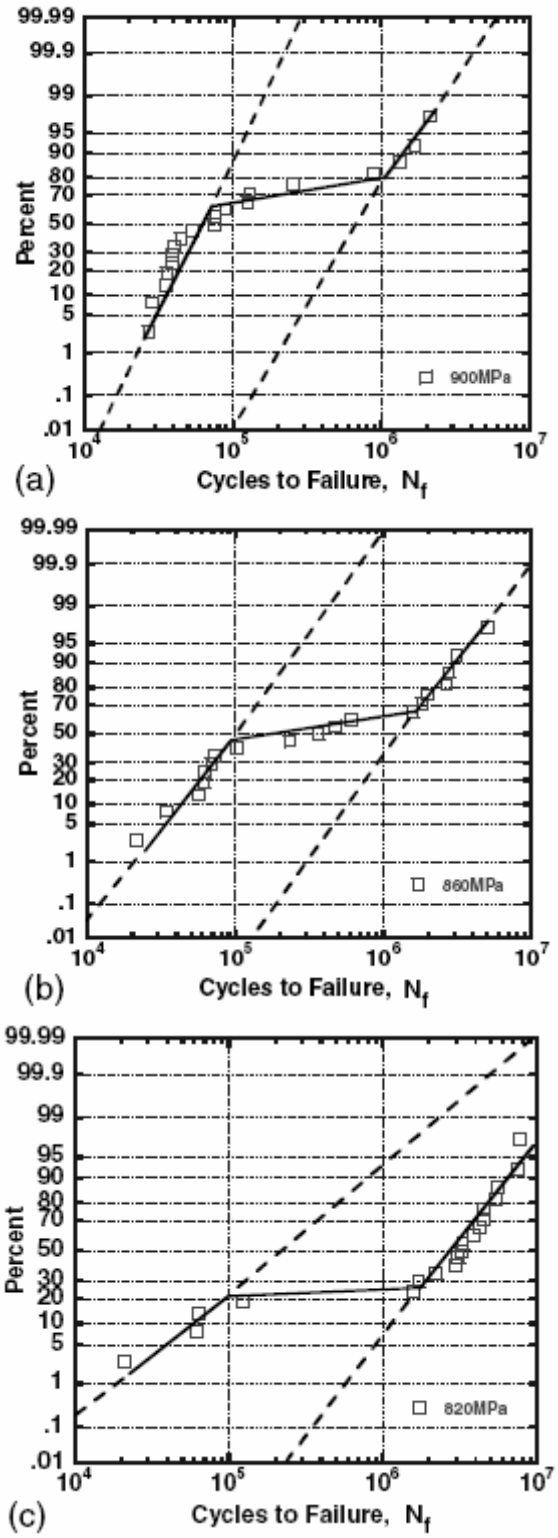

Figure 2.23: The step-like nature of the CDFs at (a) σ_{max} = 900 MPa, (b) σ_{max} = 860 MPa and (c) σ_{max} = 820 MPa indicating dual failure mechanisms. Ref: Jha and others, 2003.

The probability of failure plots were subsequently segregated into “Type I” and “Type II” failure modes and the data from each failure mode was extrapolated to the 0.1 % probability of failure design mark used for aircraft and turbine engine components. A plot is provided for the stress of 900 MPa (Figure 2.24) to illustrate the point of adjusted life extension using this more physically based approach to fatigue life prediction. The estimated life extension is approximately five times, or half an order of magnitude. The mean lives of the two failure types in Ti6246 differed by two orders of magnitude. In addition, the likelihood of one type of failure versus the other type changed noticeably with the different stress levels (Jha and others, 2003: 1642). This work on fatigue variability of the Ti6246 alloy was published in various journals and presented to several audiences (i.e., at TMS and AIP annual conferences).

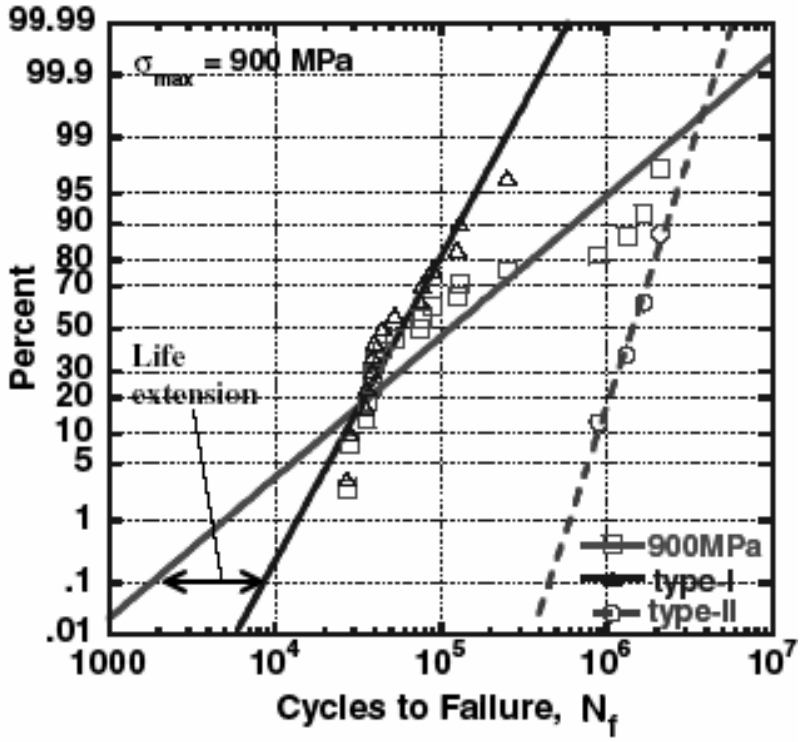

Figure 2.24: Illustration of life extension based on the worst case mechanism, i.e., Type I. Ref: Jha and others, 2003.

Whatever the type I failure might be, it is designated as the worst-case mechanism. The methodology based upon the worst case mechanism has the potential for many materials to greatly reduce the uncertainty in life and facilitate greater utilization of the useful life (Jha and others (TMS), 2005: 150).

Following the success with Ti6246, γ-TiAl (Jha and others, 2005:1293-1304) and nickel-based superalloys (Jha and others (TMS), 2005: 343-350) using the multiple-failure mechanism methodology, researchers at the Ohio State University and AFRL/ML duplicated the same test conditions with β-processed Ti64 alloy, with the exception of using a stress ratio of R = 0.1. Fatigue tests were repeated at the stress levels of 550, 600, and 675 MPa. Unlike Ti6246, a bimodal distribution (two separate failure mechanisms distinguishable in a variability plot) was not apparent. Crack growth analyses concluded that most of the lifetime was spent in crack propagation. Other methods, such as fuzzy logic models, were attempted to determine the microstructural characteristics with greatest impact on lifetime. The minimum lifetime for β-processed Ti64 alloy corresponded best to the cyclic life spent propagation a penny-shaped crack of area 100 μm^2, closest in area size to the evident critical crack initiation site (Polasik and others, 2005: 121-128).

Crack Initiation and Damage Mechanisms

Work done in the mid-1970's on load controlled tests of wrought Ti64 with stress ratio of R = 0.1 suggested that as much as 85 % of the low cycle fatigue (LCF) life and 98 % of the HCF life are spent initiating a crack of 0.5mm (0.02 in). Further studies on other alloys demonstrated a correlation between the premature initiation and loss of total fatigue life. The observation of crack initiation sites indicate that one of the keys to

understanding fatigue behavior of a material system is a basic study of the most frequently occurring damage mechanisms. Even with the best equipment and analytical tools, it is a daunting task to derive the information from broken specimens for an in-depth study (Eylon and others: 1980:95). The damage mechanisms considered here are surface flaws, inclusions, and porosity.

Surface Flaws

Machining marks, scratches and pits on a material's surface add stress concentrations to the concentrations already present because of specimen geometry. Fine grained materials are more adversely affected by rough surface finishes than coarse grained materials. Fatigue cracks almost always initiate at a free surface so any type of surface treatment is expected to noticeably affect the fatigue life (Bannantine and others, 1990:13-14). Fatigue crack initiations, then, for fine-grained Ti-B without significant defects alloys are expected to mostly occur at the surface.

Inclusions

The most frequent type of initiation found in fully dense prealloyed powder metallurgy material is inclusion-based initiation, which can result in severe fatigue life debit. Inclusions can often be chemically identified and analyzed from the fracture surface. On the other hand, the crack origin may be very difficult to identify (Eylon and others: 1980:96-97). Peebes and Kelto investigated five different types of prealloyed powders, of which none were free of contaminants. The major contaminants or inclusions in the powders were of a ceramic nature: aluminum, silicon, calcium, and magnesium, or of an organic nature, or introduced through equipment: iron and stainless steel (1980:57). A variety of microstructure related initiation mechanisms could also be

identified but will be included with inclusions since they are interrelated. Some reasons for inclusions are as follows:

> Most of the nonmetallic inclusions are found in a discrete form since they are picked up in the production equipment or during the subsequent handling of the powder. However, some metallic inclusions may be added to the powder in the powder making process and embedded in the powder particles. Discrete contamination particles can often be detected in the powder…and can be cleaned to certain extent by several methods although cleaning must always be considered as a poor substitute for producing clean powder initially. However, it is almost impossible to eliminate the embedded particles (Eylon and others, 1980: 78-79).

Porosity

Pore initiation typically occurs in elemental powder compacts, which are not fully dense unlike prealloyed, compacted powder material. Partially due to the difference in density, the pore initiations result in lower fatigue strength. Failures involving porosity are most likely to occur at the surface because of increased slip activity on specimen surfaces (Eylon and others, 1980:99). The role of porosity was not expected to be significant in the causes of premature failure for the material for this thesis because the specimens came from dense, prealloyed material.

Fatigue Crack Growth Behavior

Life prediction research at AFRL/ML has made progress towards validating the probabilistic fatigue variability approach by analyzing the fatigue crack growth behavior of the same materials. Fatigue variability and estimated crack growth life for a nickel-based superalloy are presented in Figure 2.25. Failures in the alloy were characterized using surface versus subsurface crack initiation. Zero initiation life was assumed at 940 MPa for starting crack sizes between 50 and 100 microns. The Paris regime was linearly extrapolated to approximate small crack growth behavior. Figure 2.26 is provided as a

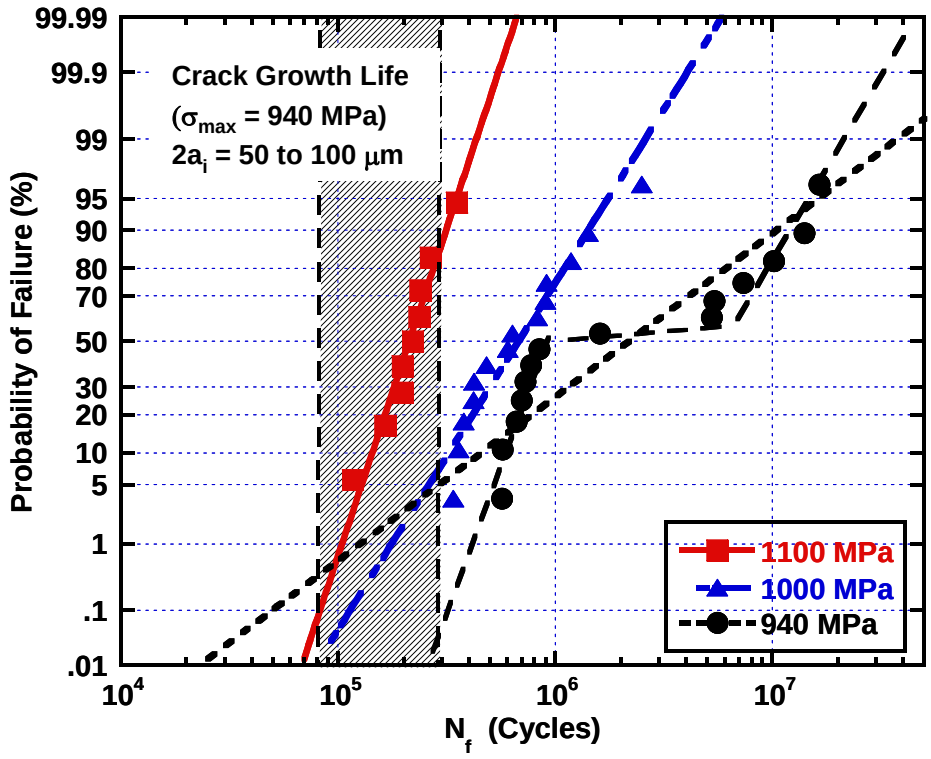

Figure 2.25: Cumulative probability distribution functions representing fatigue variability at different stress levels plotted in lognormal probability space for a nickel based superalloy. Ref (Jha and others, 2005).

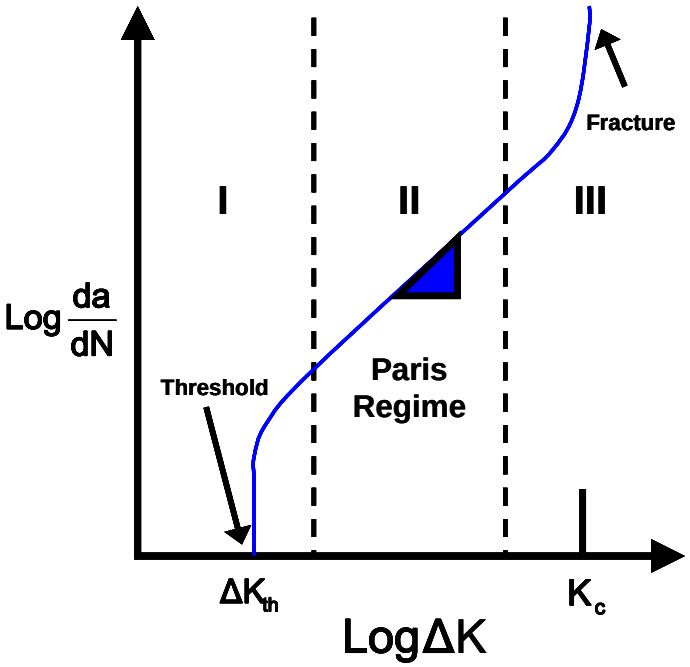

Figure 2.26: Typical fatigue crack growth behavior in metals. Ref: Anderson.

reference for typical fatigue crack growth behavior in materials. Even this conservative estimate of crack growth behavior clearly predicts a higher lifetime than the 1 in 1000 failure criterion used for engine components, which indicates that the fatigue variability extrapolation is still too conservative. Another apparent trend is that the cumulative distribution function used in making the extrapolation became less effective with decreasing stress level. At 940 MPa, for example, a step like shape of the experimental points is apparent that indicates the presence of two separate mechanisms. A further point is that the predicted crack growth life at the maximum stress of 940 MPa for flaw sizes from 50 to 100 μm, shown in the shaded part of Figure 2.25, also indicated that the 0.1 % probability of failure extrapolation was too conservative. Combining the knowledge of both fatigue variability and fatigue crack growth behavior on the basis of the lowest-life or worse-case damage mechanism was shown to substantially increase utilization of the alloy's useful life as well reducing uncertainty and increasing the minimum life (Jha and others (TMS), 2005: 343-345, 349).

Crack Growth Behavior of Ti64 Alloys and Composites with Boron

Some crack growth behavior of boron modified Ti64 composites and alloys was reported at TMS in 1995, where Soboyejo and others showed their mechanical property results of six boron-modified titanium alloys compared to baseline Ti64. Preliminary results obtained at that point indicated that as-extruded Ti-6Al-4V-0.5B, Ti-6Al-0.5B, and Ti-7.5Al-4V-0.5 each had better fatigue crack growth resistance than mill annealed Ti64. The crack growth rates for the best case, in Ti-6Al-0.5B, were about half an order of magnitude lower than that of mill annealed Ti64. The progress suggested that further improvements in fatigue resistance could be engineered by optimization of processing

parameters to minimize damage mechanisms attributed to things such as porosity. The same three alloys produced in-situ via blended elemental powder metallurgy also exhibited relatively slow fatigue crack growth rates and compared favorably with those of the mill-annealed Ti64. They postulated that the TiB whisker structure, composition, and microstructure significantly contributed to increasing fatigue crack growth resistance (1995: 178-195).

The next effort to examine fatigue crack growth in a boron modified titanium matrix composite was a collaboration of the Department of Materials Science and Engineering at Ohio State University and the Boeing Company. They studied an ingot metallurgy alloy composite version of Ti-6Al-4V-0.5B produced via induction skull melting and conventional casting. Boron was added in elemental form during casting. Single edge notched (SEN) specimens of size 50 x 13 x 6.35 mm were fabricated using electro-discharge machining, annealed at 704^0C for one hour, and air cooled afterwards. The microstructure was a typical Widmanstaetten $\alpha+\beta$ structure. The SEN specimens were tested in room temperature lab conditions using three-point bend loading. Observations in a scanning electron microscope (SEM) showed a ductile transgranular fracture mode in the fatigue region and ductile dimpled mode in the overload region. The boron-modified titanium composite was different from fracture surfaces of conventional Ti64 because fatigue striations were not as visible. Neither the elastic bridging nor the toughening from the crack bridging of the TiB whiskers appeared to have a noticeable effect upon Ti-6Al-4V-0.5B's fatigue crack growth resistance (Dubey, 1999: 303-304, 308).

Shademan's paper gives some insight into the micromechanisms of fatigue crack growth in mill annealed Ti64. He and his colleagues presented a physically based model that assumes crack extension per cycle has a direct proportionality relationship to the change in crack-tip opening displacement during the cyclic loading between the maximum and minimum stress intensity factors. Experiments were carried out using compact tension (CT) and SEN specimens at a variety of stress ratios. It was concluded that the micromechanisms of fatigue crack growth in Ti64 were strongly dependent upon the stress ratio and upon ΔK, the difference between maximum and minimum stress intensity factors (K_{max} and K_{min}). For the near threshold regime, fatigue crack growth occurred by a cleavage-like fracture mode. In the Paris regime, fatigue fracture occurred by a classical crack tip blunting mechanism that caused the formation of striations. Crack growth in the high regime, or overload region, occurred by a combination of ductile dimpled fracture and fatigue striations (Shademan and others, 2001: 1-2, 6, 9).

The final crack growth work considered in this literature review comes from Soboyejo, Shen, and Srivatsan investigating the fatigue crack nucleation and growth in Ti-6Al-4V-0.5B, which was published in 2004. The manufacturing of this material included similar ingot metallurgy, extrusion, and heat treatments steps from Soboyejo's previous work and hence can not be directly compared to the prealloyed powder metallurgy Ti64+1B material investigated in this thesis. They concluded that small amounts of TiB whiskers (~2.5 vol. %) could degrade the overall fatigue life of Ti64 because of premature nucleation of fatigue cracking of the TiB whiskers within the first 20% of life. The near-threshhold crack growth rates were faster than those in the Ti64 matrix material with the same nominal processing conditions. Although they point out

that there didn't appear to be a motivation for use of in-situ TiB whisker reinforced TMCs from a fatigue and fracture toughness standpoint, they noted the mechanical property advantages (i.e. modulus, tensile strength, and yield strength) of the material over what can be achieved with other titanium alloys (Soboyejo, 2004: 157-158).

AFGROW

The Air Force Growth (AFGROW) software provides a tool for analyzing crack growth lifetimes of metallic structures. It is one of the most efficient, user-friendly, and available crack growth life prediction tools. AFGROW is chiefly used for aerospace applications but can be applied to many metallic structure types that experience fatigue cracking. The stress intensity factor library currently provides models for over 30 different crack geometries (Harter, 2006). In this study, the data obtained from performing a fatigue crack growth test for Ti64+1B was entered into the tabular lookup menu of AFGROW so that the fatigue stress-life behavior could be predicted from it for a number of different maximum stresses and varying initial flaw sizes. The tabular lookup capability of AFGROW is extremely useful in analyzing fatigue and crack growth behavior of materials for which a database doesn't exist. AFGROW has the capability of calculating fatigue and crack growth rate properties for a variety of stress ratios and specimen geometries for common structural materials such as Ti64. The procedure for how AFGROW was used and its contribution to understanding and predicting fatigue and crack growth properties for Ti64+1B have been included in Chapters 3 and 4.

III. Procedures

This chapter describes the experimental and analytical methods employed while carrying out this research. Descriptions are given for the material that was evaluated, the mechanical test and data reduction procedures, and the fatigue variability and crack growth analysis approaches. The crack growth test data are depicted in several forms: raw, optical, corrected, and reduced data and plots of crack length (a) versus cycle count (N) curves as well as stress ratio (R) and maximum load (P_{max}) versus N are provided to facilitate describing the data reduction procedures. The fatigue variability, the crack growth rates, and the comparisons between the experimental data and outputs from credible models are reserved for Chapter 4.

Ti64+1B Material

The Ti-6Al-4V-1B-0.05C-0.11O (Ti64+1B) rolled plate used for this study was supplied by FMW Composites, Inc in Bridgeport, WV. The starting powder used in production of the plate was provided to FMW by Crucible Research Corporation in Pittsburgh, PA. The pre-alloyed Ti64+B powder was made by induction skull melting (ISM) followed by inert gas atomization. A schematic of the atomizer was shown in Figure 2.13 in Chapter 2. The actual atomization unit and cyclone used by Crucible are shown in Figure 3.1 and is described by Dr. Yolton (57):

> The titanium gas-atomization unit consists of a melting chamber, an atomization tower, and a cyclone collector… The boron is typically added as titanium diboride powder, and carbon is added as graphite powder. As the charge is melted, a skull forms at the crucible bottom and wall so the molten alloy is always contained in a solid skull of roughly the same composition. After the charge is fully melted and homogenized, it is bottom poured and atomized with high-pressure argon gas. The atomization gas carries the powder to the cyclone where

the powder is collected in a removable canister. After cooling under an argon atmosphere to room temperature, the powder is removed for further processing.

Figure 3.1: Picture of titanium atomization tower and cyclone at Crucible Research Corporation used to make Ti64+1B powder via pre-alloyed approach. Ref: Yolton, 2007 TMS presentation.

The thermomechanical processing steps used to prepare the Ti64+1B material are outlined in Figure 3.2. For this material the powder was classified as -35 mesh, which corresponds to powder not larger than 500 μm in diameter (Yolton, 2007 TMS presentation). Two compacts, with approximately 979 N (220 lbs) of Ti64+1B powder each, were made. The steps, described in Figure 3.2, of degassing, sealing, hot isostatic pressing (HIP), and heat treatment were used. The two compacts, weighing 1.6 kN (360 lbs) each, underwent hot isostatic pressing (HIP) at Bodycote in London, OH. The HIP was conducted at 1018°C and 103 MPa for three hours followed by heat treatment at 1300°C for six hours.

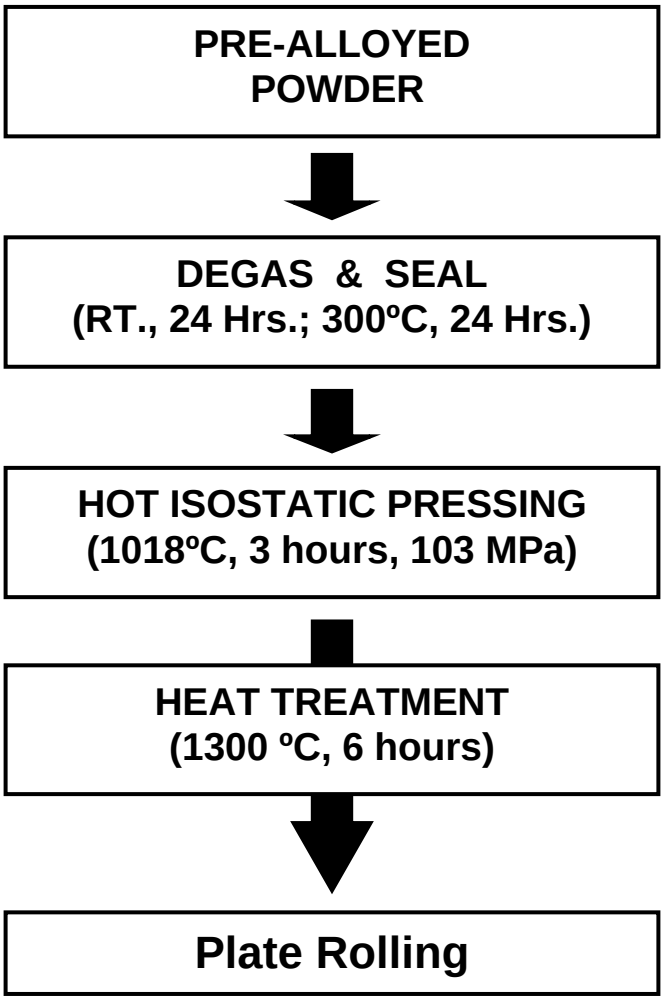

Figure 3.2: Thermomechanical processing steps for prealloyed Ti64-xB alloy.

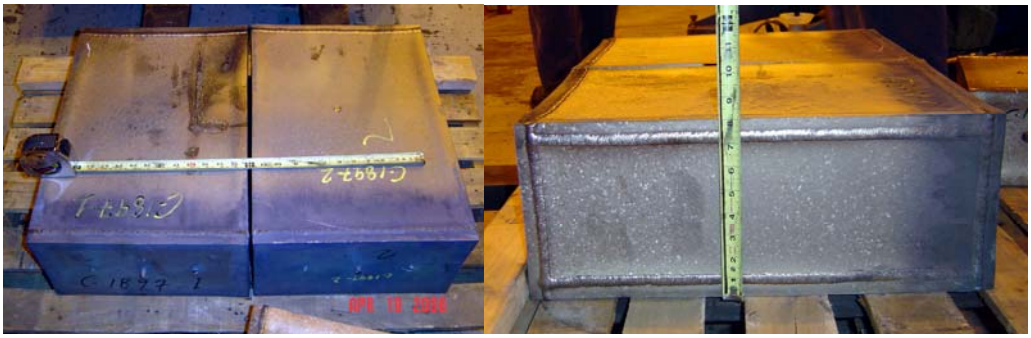

Figure 3.3: Ti-6Al-4V-1B-0.05C-0.11O compacts as they were received at Bodycote. Ref: Tamirisakandala.

After HIP, the material was delivered to the Manufacturing Sciences Corporation (MSC) in Oakridge, TN and the Ti64 can was removed from the as-HIPed Ti64+1B material before rolling commenced. The MSC Oakridge facility used a 4-high reversing

mill with 47 cm (18.5 in) diameter rolls and 22.2 x 10^3 kN (2500 tons) of separating force (Figure 3.4). The billet was loaded into a furnace (Figure 3.5) and heated to 1100^0C (2000^0F). Each billet was held for several hours in the furnace to ensure thermal soak and was then transferred to the rolling mill with a total transfer time of about 30 seconds (Figure 3.6). A first round of eight passes (Figure 3.7) was conducted on the bill reducing the dimensions to 71.1 x 52 x 10.1 cm (28 x 20.5 x 4 in) and the surface temperature had dropped to 950°C (1750°F). The plate was reheated to 1100^0C (2000^0F) and a second round of rolling passes was performed. The billet was reduced to a plate of 96.5 x 100.3 x 3.8 cm (38 x 39.5 x 1½ in) dimensions (Figure 3.8). After a third round of eight passes, the plate had a giant potato chip shape with 96.5 x 156 x 2.5 cm (38 x 61.5 x 1 inches) dimensions (Figure 3.9) and had become too big for the rolling mill. It was cut into two pieces (Figure 3.10) while at a temperature of 1040°C (1900°F). The two half plates (Figure 3.11) were flattened and stress relief annealed at 760°C (1400°F) for 1 hour and air cooled.

Figure 3.4: Rolling mill at Oakridge, TN facility. Ref: Tamirisakandala.

Figure 3.5: Ti64+1B billet being loaded into furnace. Ref: Tamirisakandala.

Figure 3.6: Ti64+1B billet just transferred from furnace to rolling mill. Ref: Tamirisakandala.

Figure 3.7: Ti64+1B billet after first round of 8 rolling passes. Ref: Tamirisakandala.

Figure 3.8: Ti64+1B, now a plate after second round of 8 rolling passes. Ref: Tamirisakandala.

Figure 3.9: Ti64+1B plate after third round of 8 rolling passes. Ref: Tamirisakandala.

Figure 3.10: Cutting Ti64+1B rolled plate into two plates. Ref: Tamirisakandala.

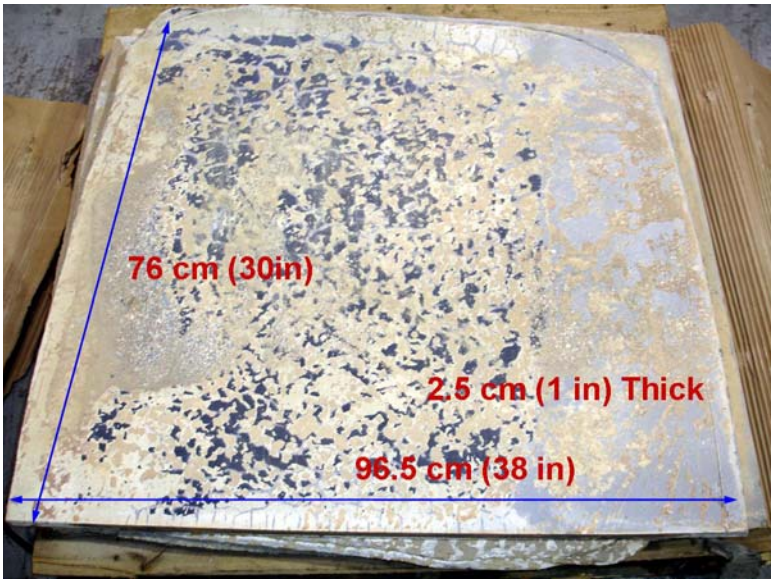

Figure 3.11: Two plates after cutting for tensile and fatigue testing. Ref: Tamirisakandala.

Specimens for tensile and fatigue testing of the Ti64+1B rolled plate material were machined from the plates shown in Figure 3.11 at BITEC in Dayton, OH. The

order included 12 round tensile specimens, 100 cylindrical dogbone fatigue specimens, and four compact tension (C(T)) specimens for fatigue crack growth testing. For the tensile specimens, six were machined in the longitudinal direction and six in the transverse direction. All the cylindrical dogbone and C(T) crack growth specimens were machined in the longitudinal direction. In addition, the round tensile and cylindrical dogbone fatigue specimens were extracted from a variety of locations throughout the entire rolled plate and underwent low-stress grinding to achieve a desirable surface finish. All of the test specimens were prepared according to ASTM standards (E8—04, 2004: 1-24, E466-96, 2002: 541-545, and E 647—00, 2000: 615-627).

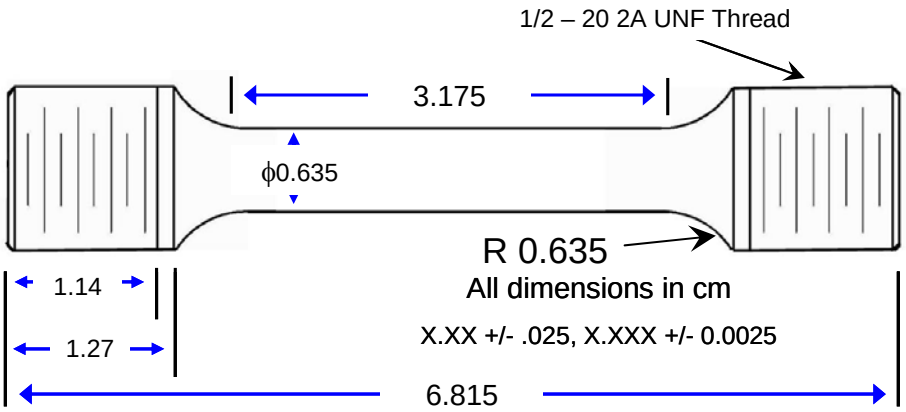

Figure 3.12: Geometry for 12 Ti64+1B round tensile specimens.

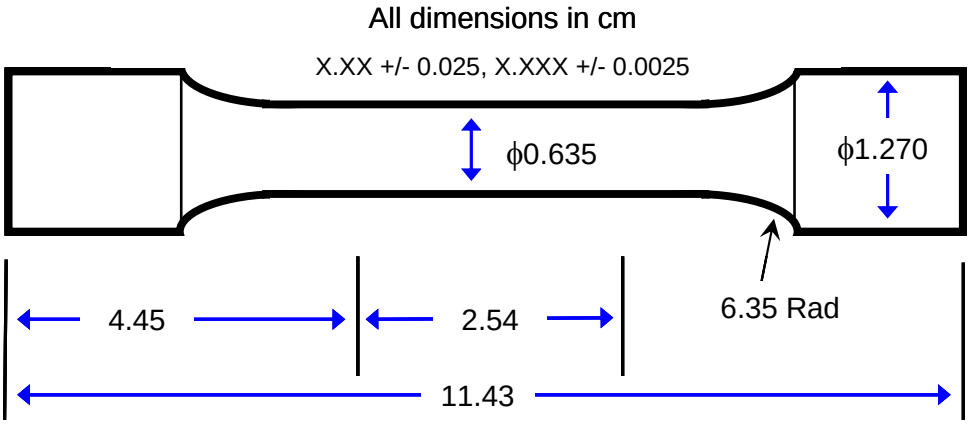

Figure 3.13: Geometry for 100 Ti64+1B cylindrical fatigue specimens.

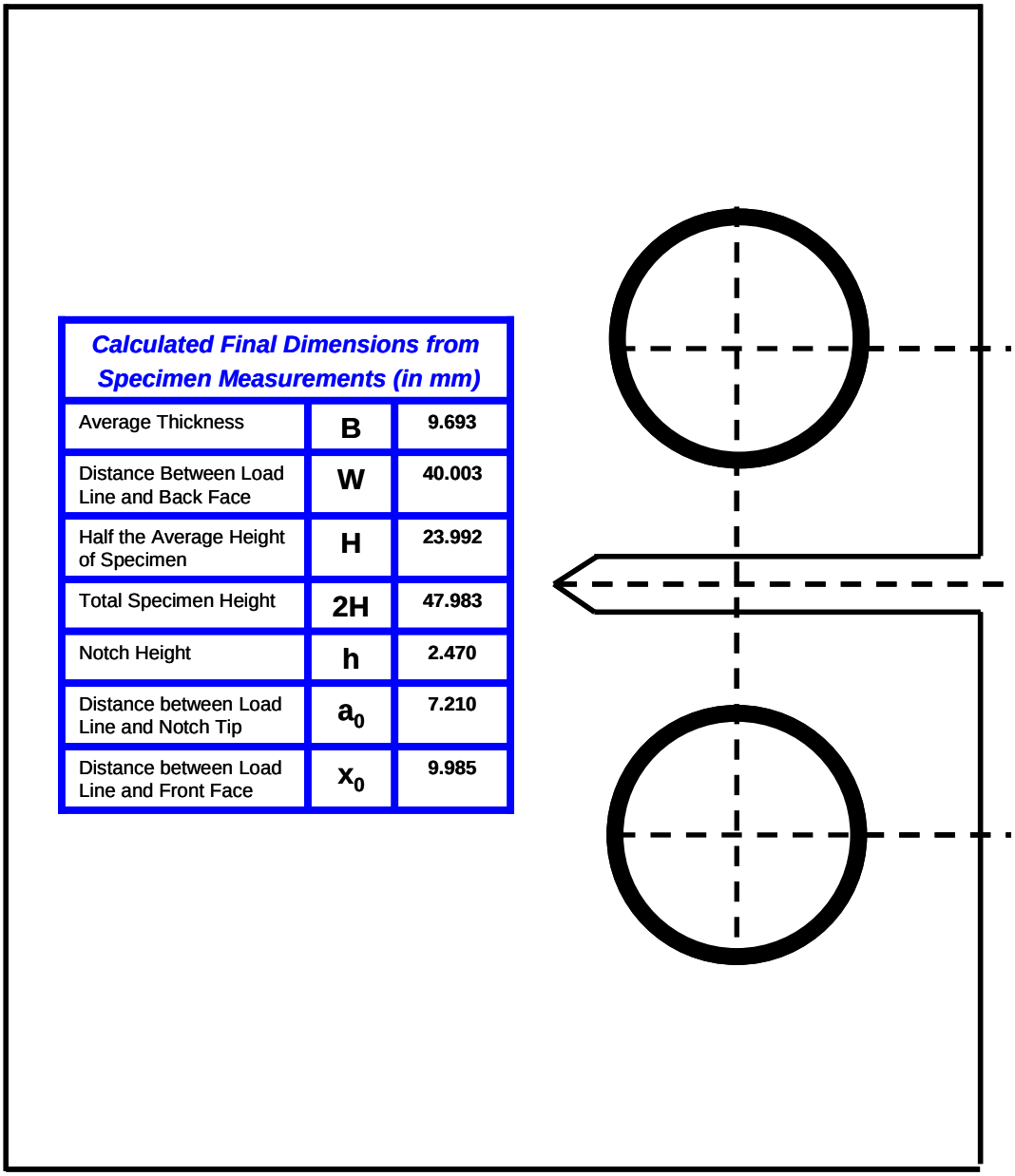

Figure 3.14: Geometry for 4 Compact Tension (CT) fatigue crack growth specimens with 48 mm total height, 10 mm thickness, and 40 mm load line to back face distance. Final dimensions for the last of the 4 specimens are shown as calculated from measurements performed with a Mitutoyo machinist microscope and then were used in fatigue crack growth analysis.

The specimen geometries for the tensile, fatigue, and crack growth C(T) specimens are shown in Figures 3.12, 3.13 and 3.14, respectively. Figure 3.15 is a picture of the Mitutoyo machinist microscope used in making specimen measurements.

Figure 3.15: Mitutoyo machinist microscope used to make fatigue and CT specimen measurements.

Tensile Testing Procedure

The tension tests were conducted in accordance with ASTM E8-04, which describes the standard methods of tension testing metallic materials (2004:1-24). The 12 tensile specimens were tested using an MTS 810 Material Test System (Figure 3.16).

Figure 3.16: MTS 810 Material Test System used to obtain tensile property data.

The tensile properties obtained are provided in Table 3.1 and Figure 3.17. The ultimate tensile and yield strengths compare well with similar Ti64-xB alloy data discussed in the literature review. The longitudinal and transverse directions have comparable properties and show a near 20% increase in strength and stiffness over ELI Ti64 material. No debit to ductility is apparent. The data, as demonstrated by the standard deviation in Table 3.1, had very little scatter.

Table 3.1: Tensile properties of prealloyed ELI Ti64+1B.

ID	***YS***	***UTS***	***e***	***E***
	ksi	ksi	%	Msi
Longitudinal				
1L1	141	155.9	11.6	20
1L2	140	155.7	11	20.1
1L3	139	154.6	10.5	20.1
1L4	140	154.7	11	19.9
1L5	140	154.6	10.2	19.5
1L6	141.8	156.3	8.5	19.9
Avg	**140**	**155**	**10**	**20**
SD	**0.97**	**0.76**	**1.08**	**0.22**
Transverse				
1T1	142.3	157.5	10.5	19.9
1T2	141.8	157.3	11.1	20.1
1T3	142.8	156.9	11.3	20
1T4	146.4	160.5	11.3	20.6
1T5	146.3	160.4	9	19.4
1T6	146.6	160	10.7	19.4
Avg	**144**	**159**	**11**	**19.9**
SD	**2.29**	**1.70**	**0.87**	**0.46**

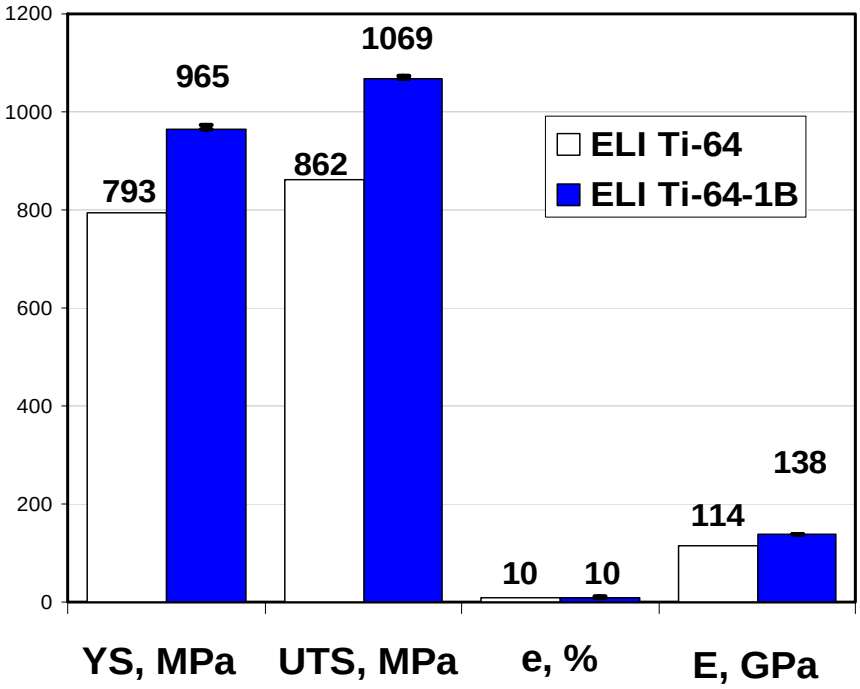

Figure 3.17: Comparison of tensile properties and ductility of prealloyed ELI Ti64 with ELI Ti64+1B.

Microstructure

Metallography was performed on material taken from the grip sections of two tensile specimens, one pulled in the final rolling (longitudinal) direction and the other in the transverse direction. These specimens were mounted in conductive material and polished to 1 micron mirror-like finish for scanning electron microscopy. The images in Figures 3.18 a through 3.18c depict the microstructures in the longitudinal, short transverse and transverse directions, respectively. The black whiskers and particles are the TiB phase. The gray and light gray are alpha and beta phases of titanium, respectively. The short transverse and transverse images confirm that the TiB whiskers were uniformly distributed and randomly oriented prior to rolling. The longitudinal view suggests that during rolling, the whiskers became aligned in the rolling direction. Whisker lengths ran up to 30 μm and diameters up to 3 μm. The average aspect ratio was

nominally 10. This compares well with the work of Tamirisakandala and others who found aspect ratios in other prealloyed Ti-B alloys to be in the range of 8 to 12 (2003: 62). The mean volume fraction of TiB was between five and seven %, which agrees with Lieberman et al's characterization of boron modified Ti64 (2007 TMS presentation).

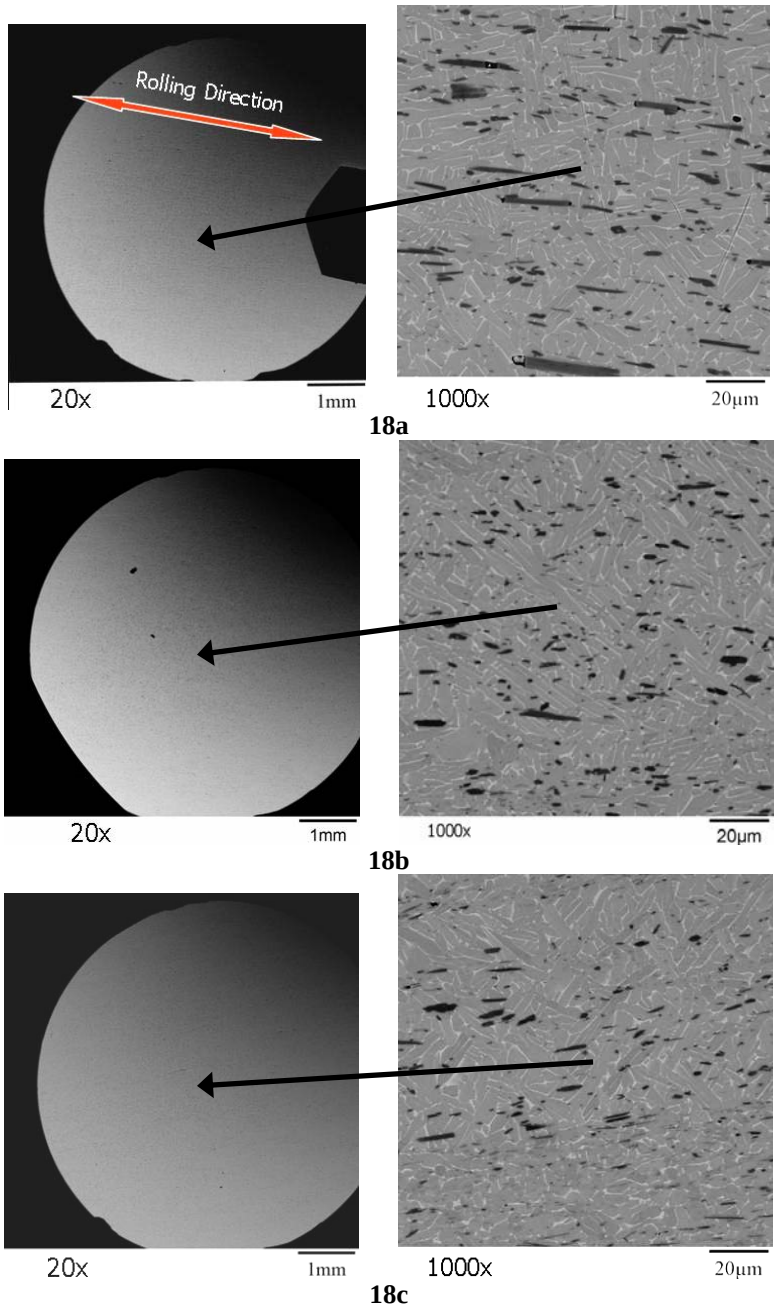

Figure 3.18: Back-scattered electron images of Ti64+1B alloy in a) the longitudinal direction, b) the cross-section from the longitudinal direction or short transverse and c) the transverse direction.

Fatigue Stress-Life Testing Procedure

Smooth bar fatigue testing was conducted on an MTS 810 servo hydraulic test system equipped with a 458 controller, Figure 3.19. A total of 67 constant amplitude load controlled tests were performed at room temperature in a laboratory air environment. All tests utilized a load ratio, R (= $\sigma_{min}/\sigma_{max}$), of 0.1 and a frequency of 20 Hz. The objective of the first ten tests was to develop an initial stress-life (S-N) curve for the Ti64+1B alloy. The stress levels ranged from 586 MPa to 896 MPa. The results from the initial tests are provided in Table 3.2 and Figure 3.20. The test at 896 MPa was repeated because of an unexpected poor result, which will be addressed in Chapter 4

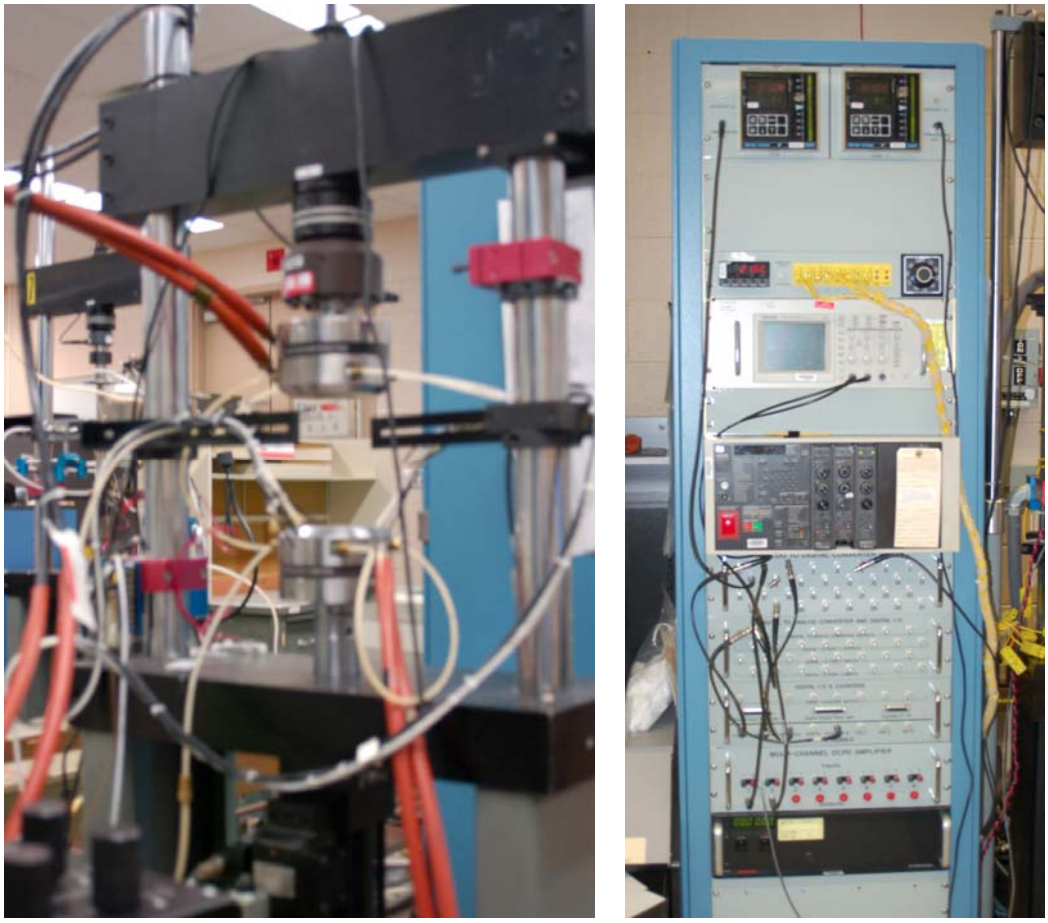

Figure 3.19: Fatigue testing equipment. Left-actual testing site shown with MTS 810 servo hydraulic test system, Right-MTS 458 controller.

Table 3.2: Initial fatigue data for Ti64+1B.

MPa	ksi	N
586	85	10,400,000
621	90	1,864,456
655	**95**	940,601
690	100	501,496
724	105	285,520
758	**110**	116,754
827	120	69,186
862	**125**	49,840
896	130	31,816
896	130	4,485

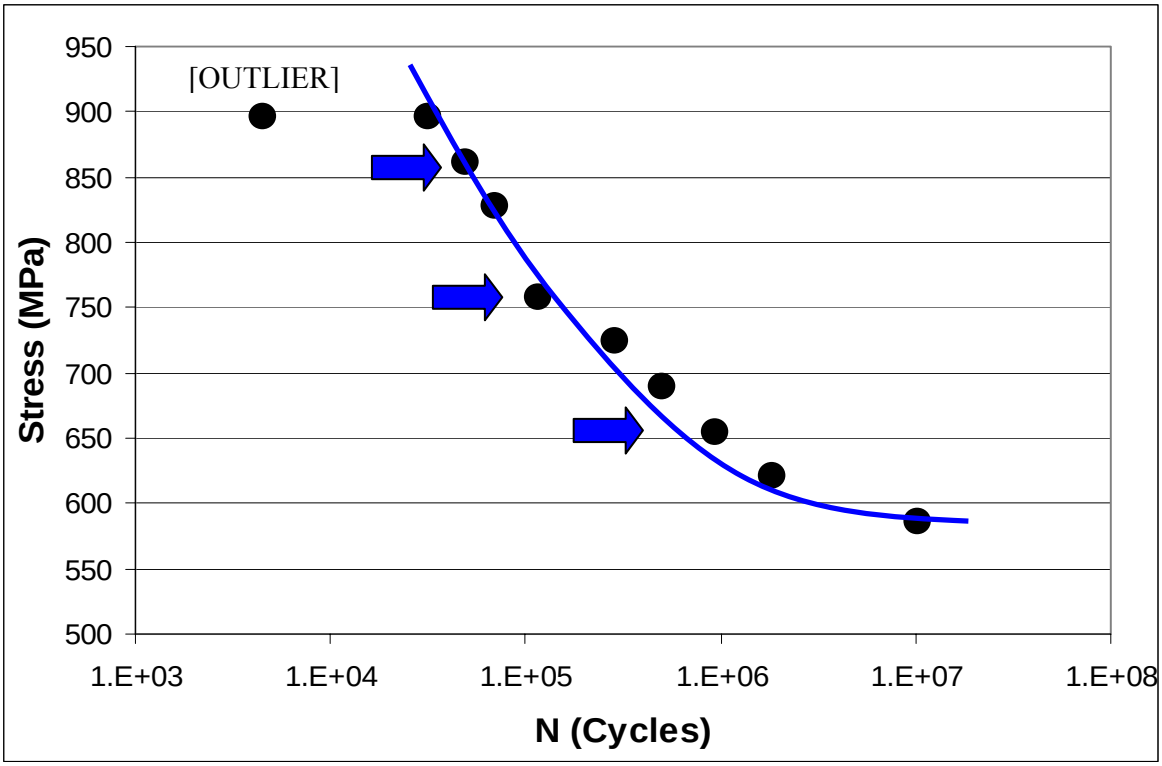

Figure 3.20: S-N Curve of initial fatigue data for Ti64+1B.

The initial S-N screening was essential to identify three levels for the fatigue variability study. As shown by the arrows in Figure 3.20, maximum stress levels of 655, 758, and 862 MPa were selected to achieve target targeted lives of $5x10^4$, 10^5, and 10^6 cycles. 19 additional tests, making a total of 20, were conducted at each selected stress level to

establish the degree of variability under fatigue loading conditions. The reason that 20 tests were performed per condition was to adequately capture the entire variability distribution and determine whether the distribution was bimodal or not as a result of potentially multiple mechanisms leading to fatigue damage. The data for the three stresses are in Tables 3.3, 3.4, and 3.5.

Table 3.3: Fatigue variability data for Ti64+1B at lowest stress level of 655 MPa.

Stress Level	9.41E+05
655 MPa / 95 ksi	6.99E+06
	2.12E+06
	1.65E+06
Statistics for N (Cycles)	4.74E+06
Median	2.66E+06
1.64E+06	7.93E+04
Minimum	8.37E+05
7.93E+04	8.38E+05
Maximum	1.63E+06
6.99E+06	3.71E+06
Standard Deviation	2.50E+06
1.77E+06	6.89E+05
Order of Magnitude Spread	9.43E+05
(= LOG(max divided by Min))	7.34E+05
1.9	2.31E+06
	2.88E+06
	6.40E+05
	4.76E+06
	9.29E+05

Table 3.4: Fatigue variability data for Ti64+1B at middle stress level of 758 MPa.

Stress Level	1.17E+05
758MPa / 110 ksi	5.55E+05
	1.34E+06
	9.63E+03
Statistics for N (Cycles)	1.95E+05
Median	1.57E+05
1.20E+05	1.03E+05
Minimum	9.09E+04
9.63E+03	1.38E+05
Maximum	8.46E+04
1.34E+06	8.30E+04
Standard Deviation	1.10E+05
2.90E+05	1.60E+05
Order of Magnitude Spread	8.03E+04
(= LOG(max divided by Min))	1.41E+05
2.1	1.22E+05
	2.07E+05
	1.23E+05
	7.12E+04
	1.08E+05

Table 3.5: Fatigue variability data for Ti64+1B at highest stress level of 862 MPa.

Stress Level	4.98E+04
862 MPa / 125 ksi	5.05E+04
	2.00E+04
	4.52E+04
Statistics for N (Cycles)	5.44E+04
Median	4.29E+04
4.72E+04	4.81E+04
Minimum	5.10E+04
2.00E+04	4.62E+04
Maximum	4.21E+04
5.44E+04	5.27E+04
Standard Deviation	4.53E+04
7.23E+03	4.18E+04
Order of Magnitude Spread	4.92E+04
(= LOG(max divided by Min))	5.04E+04
0.4	4.59E+04
	4.90E+04
	5.00E+04
	4.00E+04
	4.53E+04

Fatigue Life Variability Analysis Methodology

The variability analysis procedure used in this study was similar to the procedure described in chapter 2 from Jha and others (2003: 1637-1642). The fatigue variability data was analyzed using probability of failure (POF) or cumulative distribution function (CDF) plots. The program used to create these plots calculated the natural logarithms of all 20 fatigue variability points, ranked, and then normalized the logarithmic values. The vertical scale of the probability of failure plots shows the use of a normal probability scale. On a normalized probability plot, a mostly straight line is created. The intercepts plot according to Equation 3.1 where P_i represents the probability, i represents the i-th data point in rank order from smallest to largest cycles to failure, and m represents the maximum number of points in the distribution (Box, Hunter, and Hunter, 1978:329-330), which in this case is 20 for each stress level. Jha and others used Equations 2, 3, and 4 to represent the CDF and the CDF as a function of distinct damage mechanisms with the data separated into two distinct distributions. In these equations, erf is the error function, M is the mean of the natural logarithms of the cycles to failure, and S is the standard deviation of the natural logarithms of cycles to failure (2003: 1639-1640)

$$P_i = 100\frac{(i-0.5)}{m} \quad \text{for i = 1, 2, … m.} \tag{3.1}$$

$$CDF(x) = 0.5\left[1 + erf\left(\frac{\ln(x) - M}{S\sqrt{2}}\right)\right] \tag{3.2}$$

$$CDF(N_f) = p_{Type-I}CDF_{Type-I}(N_f) + p_{Type-II}CDF_{Type-II}(N_f) \tag{3.3}$$

$$p_{Type-I} + p_{Type-II} = 1 \tag{3.4}$$

The horizontal scale of the probability of failure plots representing the cycles-to-failure, N_f, was also logarithmic but not normalized.

The results from fractography, which was used to locate features and anomalies affecting crack initiation and growth, were used simultaneously to identify a dominant mechanism, if one existed, that was driving the lower tail of the lognormal distribution. The variability data from the specimens with failures caused by the life-limiting mechanism was segregated from the remainder of the data with the help of visual observation and fractography on the fracture surfaces of the 60 specimens. Two separated distributions for the data sets with and without the life-limiting flaws were plotted on the same POF charts per stress level. These plots provided insight into how severe an effect the life-limiting damage mechanism had on the lower bound of fatigue life and how the fatigue life would improve if the mechanism were removed. The fatigue variability results are discussed in Chapter 4 using lognormal probability density plots.

Given the flaw sizes along with their various locations on the fracture surfaces, it was of interest to predict the worst case scenario for these conditions. The Air Force's fatigue crack growth software, AFGROW, was used to make these predictions, but it required crack growth data for Ti64+1B since none was available in AFGROW's databases. The procedure for carrying out the fatigue crack growth test is provided in the next section. A more thorough discussion of the predictions using AFGROW for Ti64+1B follows the crack growth results in Chapter 4.

Fatigue Crack Growth Testing Procedure

The steady state fatigue crack growth (FCG) behavior of the Ti64+1B material was evaluated at a stress ratio of 0.1. The FCG test was performed in accordance with

ASTM test specification E 647-00 utilizing a compact tension, C(T) specimen, Figure 3.14 (2000: 615-627). The specimen was instrumented with a direct-current electric-potential (DCEP) system for continuous monitoring of crack length. A 458 controller, similar to that used in the fatigue S-N testing, was used. The MTS equipment used for the crack growth testing is shown in Figure 3.22. The furnace equipment shown in the picture was not used during the test, since the test was conducted at room temperature.

Figure 3.21: Equipment used for testing CT specimen. Optical microscope and extensometer equipment is included on apparatus for manually recording data while testing.

In order to monitor the electrical resistance of the specimen as an instantaneous measure of crack length, DCEP pick-up leads were tack welded to the front face of the C(T) specimen at mid-thickness above and below the crack plane. The DCEP system, thus, provided a measured of the voltage drop across the specimen and changes as a function of crack length.

Two traveling optical microscopes, one for the front face and one for the back face, were used to regularly make optical, surface, crack-length measurements for comparison with, and post correction of, the DCEP crack length measurements. The CT

specimen was polished to a one-micron, mirror-like finish to facilitate optical crack-length measurements.

Before FCG testing, the C(T) specimen was precracked at frequencies incrementing up from 10 to 20 and finally to 40 Hz at a stress ratio of 0.1. The precracking process was interrupted often to monitor K_{max} and P_{max} conditions and make minor control adjustments. Although unusual, this was necessary because of equipment sensitivity and maximum load spiking issues that plagued previous trials with 3 other Ti64+1B C(T) specimens. Equations 3.5 and 3.6 (Anderson, 2005: 347) were used to calculate the stress intensity, K, for the C(T) specimen geometry where a was the crack length, B was the average specimen thickness , W was the distance between the load line and back face, and P was the load. The initial and final K_{max} during precracking were 12 MPa√m and 4.8 MPa√m respectively. For the initial and final crack lengths of 7.21mm and 8.71mm, this corresponded to P_{max} of 5.7511 kN and 2.0680 kN respectively.

$$f(a/W) = \frac{KB\sqrt{W}}{P} \tag{3.5}$$

$$f(a/W) = \frac{2+\frac{a}{W}}{\left(1-\frac{a}{W}\right)^{\frac{3}{2}}}\left[0.886+4.64\left(\frac{a}{W}\right)-13.32\left(\frac{a}{W}\right)^{2}+14.72\left(\frac{a}{W}\right)^{3}-5.6\left(\frac{a}{W}\right)^{4}\right] \tag{3.6}$$

The fatigue crack growth (FCG) response was determined from two separate test-control procedures: decreasing ΔK (to threshold) and constant P_{max} (to fracture). Both fatigue crack growth procedures were performed at a frequency of 40 Hz, which was sufficiently slow to maintain load-control within ASTM standards but fast enough to complete threshold testing in a practical time. A sinusoidal cyclic waveform was used.

The ΔK-decreasing, also called threshold, test immediately followed pre-cracking and was started at a K_{max} of 5.5 MPa√m which was slightly higher than the K_{max} at the end of precracking (5.45 MPa√m). The load, P_{max} as shown in Figure 3.23, shed continuously from 2.35 to 1.74 kN over the first 10^7 cycles and held for another 1.5 x 10^7 cycles during which negligible crack extension occurred. The stress ratio, shown in Figure 3.24, was maintained at 0.1 ± 0.01. Threshold testing ended when crack growth arrest occurred. Crack growth arrest was defined as less than 0.1 mm crack growth in a period of 5 x 10^6 cycles (growth rate of 2 x 10^{-11} m/cycle).

Constant maximum load testing followed with a P_{max} of 1.85 kN, which was about 5% above the ending P_{max} condition from the threshold testing. The crack was intended to grow out to 32 mm, or 80 percent of the specimen's width, or until fracture. Figures 3.25 and 3.26 show P_{max} and R versus cycle count for the constant P_{max} test condition. P_{max} was maintained at 1.85 ± 0.03 kN and R was again maintained at 0.1 ± 0.01.

After completing the test, a machinist microscope was used to assess the crack for any crack tunneling that would impact the accuracy of the effective crack length. A tunneling correction was added to the optical surface measurements to provide a best estimate of the actual crack length at several points throughout the FCG test. The crack length measurements from the DCPD system were adjusted post test to the best estimate of the actual crack length, surface measurements plus the tunneling adjustment. To determine the degree of tunneling, measurements were made at the free surfaces, the mid-line, and quarter points of the C(T) specimen. Figure 3.22 is an image of the CT specimen's fracture surface and illustrates the degree of tunneling or crack curvature.

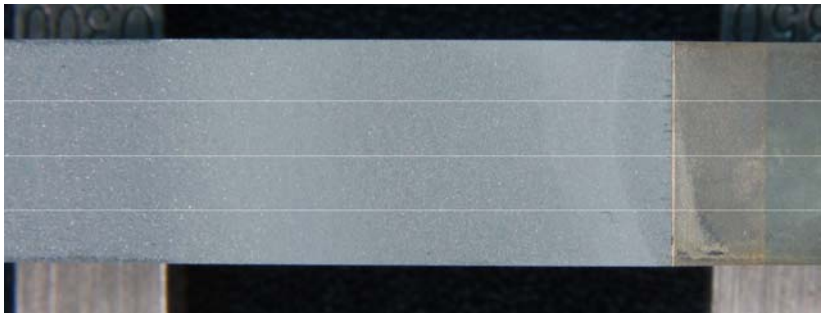

Figure 3.22: Fracture surface of Ti64+1B CT specimen demonstrating significant degree of tunneling.

Several steps were necessary to take the large quantity of crack growth test data, nearly 50,000 data points down to a da/dN curve representing both test portions. First, the optical crack length measurements had to be corrected to take into account the tunneling, which was assumed to represent the true crack length. Second, the DCEP data was adjusted to match the corrected optical data. Finally, the growth rate, da/dN, was calculated from the slope of the a versus N curve. This was accomplished using a program that utilized a least squares fit of 15 points at a time and Δa (crack length increment) of 0.05 mm. The term da/dN means the crack growth per cycle and ΔK is the difference between the maximum stress intensity factor, K_{max}, and minimum stress intensity factor, K_{min}. The FCG results, the da/dN versus ΔK curve for Ti64+1B, is included and discussed in detail in Chapter 4.

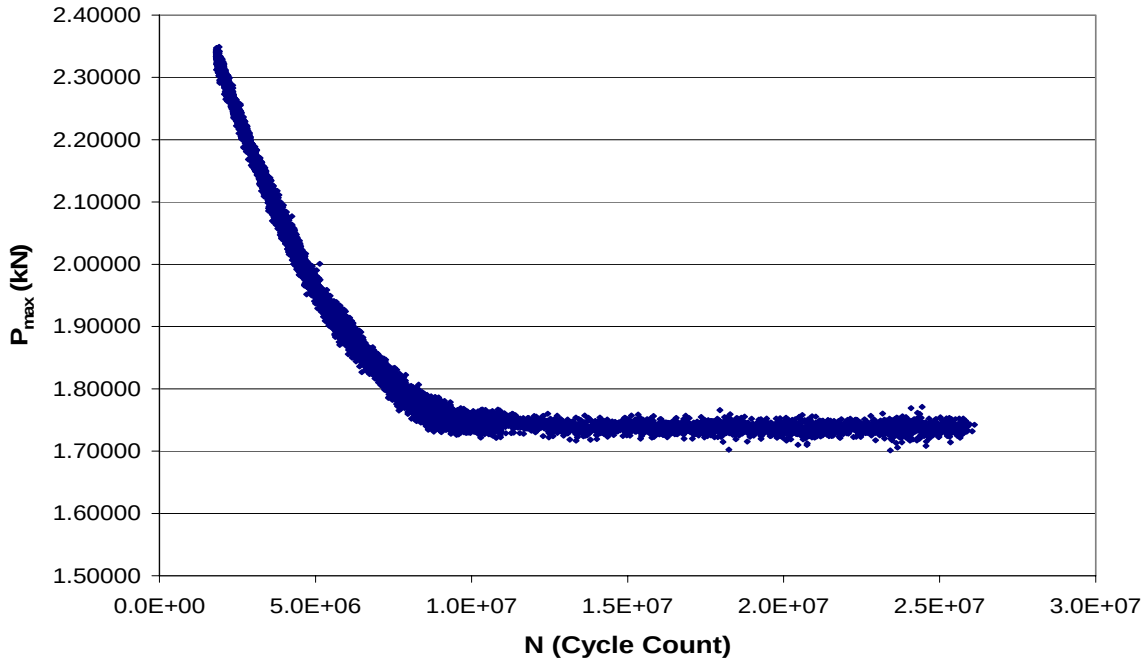

Figure 3.23: P_{max} versus cycle count for K-decreasing threshold testing.

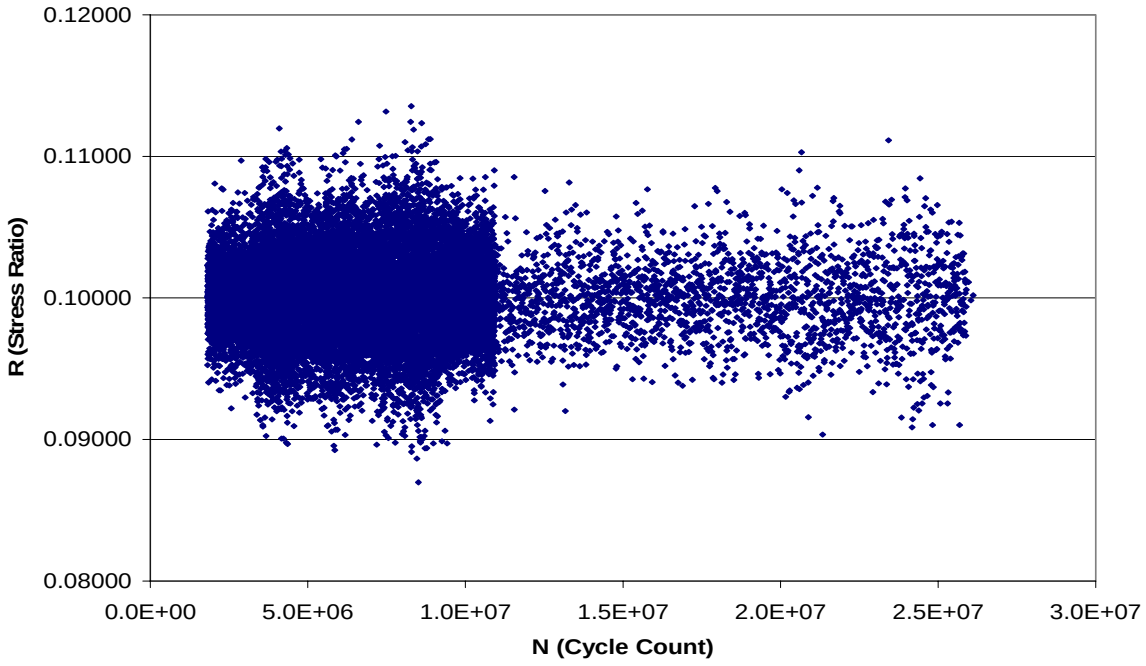

Figure 3.24: R versus cycle count for K-decreasing threshold testing.

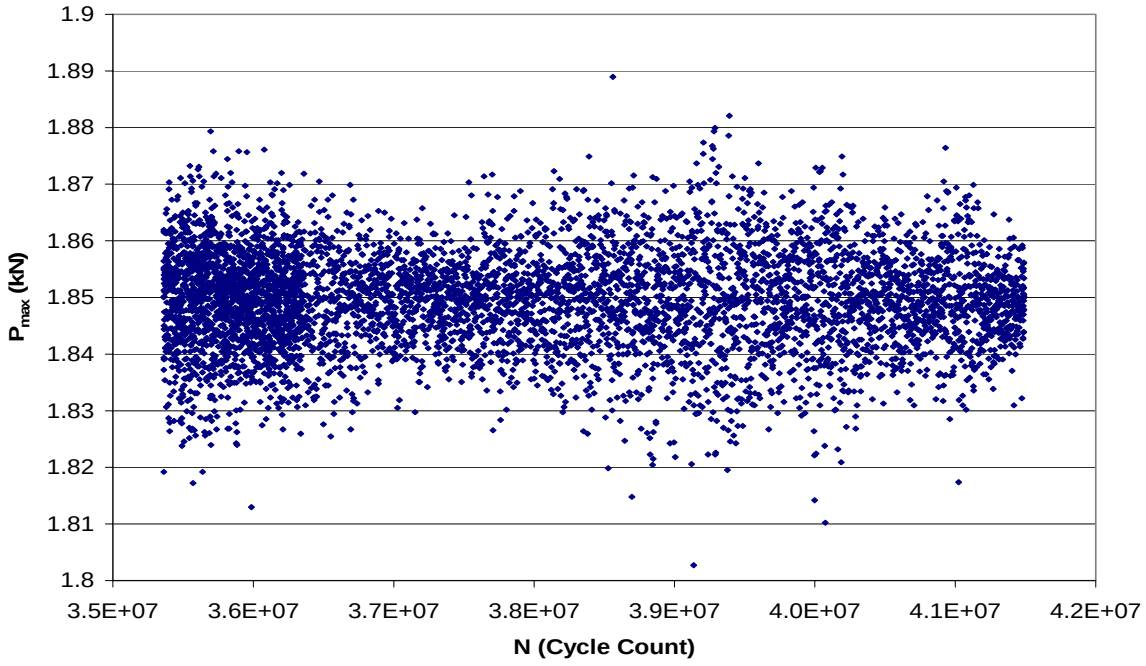

Figure 3.25: P_{max} versus cycle count for constant P_{max} post-threshold testing.

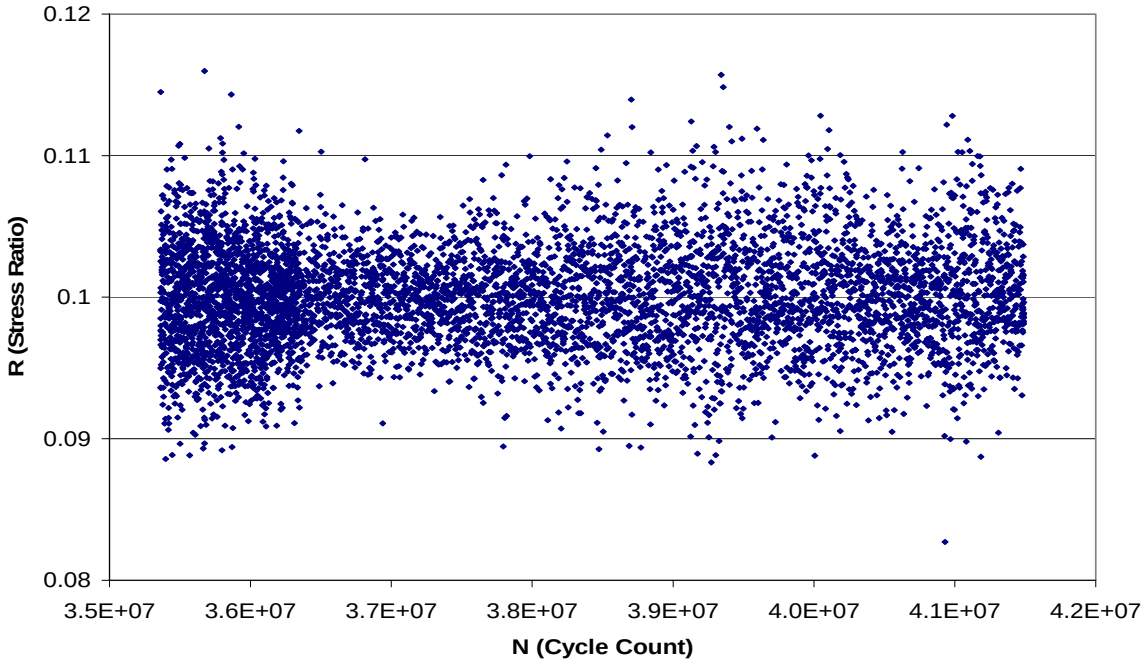

Figure 3.26: R versus cycle count for constant P_{max} post-threshold testing.

Fracture Mechanics and AFGROW

The purpose of this section and the next section is to document the fracture mechanics theory and procedure used to make a prediction of the fatigue life based solely on the fatigue crack growth behavior and initial flaw size of the Ti64+1B material. The results of this analysis are included in Chapter 4.

Inclusions within the rolled plate material were modeled as elliptical embedded or semielliptical surface cracks. Figure 3.27 captures the configuration used to simulate an embedded crack in the smooth bar fatigue tests. This type of solution is only valid as long as the crack is small compared to the specimen dimensions (2c<<specimen dimensions). The dimensions of an elliptical flaw are 2c by 2a, where c is always greater than or equal to a. For a semielliptical flaw, the dimensions would be 2c by a, where 2c is the surface length and a is the crack depth. Figure 3.27 and subsequent equations for calculating the stress intensity factor for an embedded elliptical flaw, 3.7 through 3.9, are from included from Anderson (2005: 48-49).

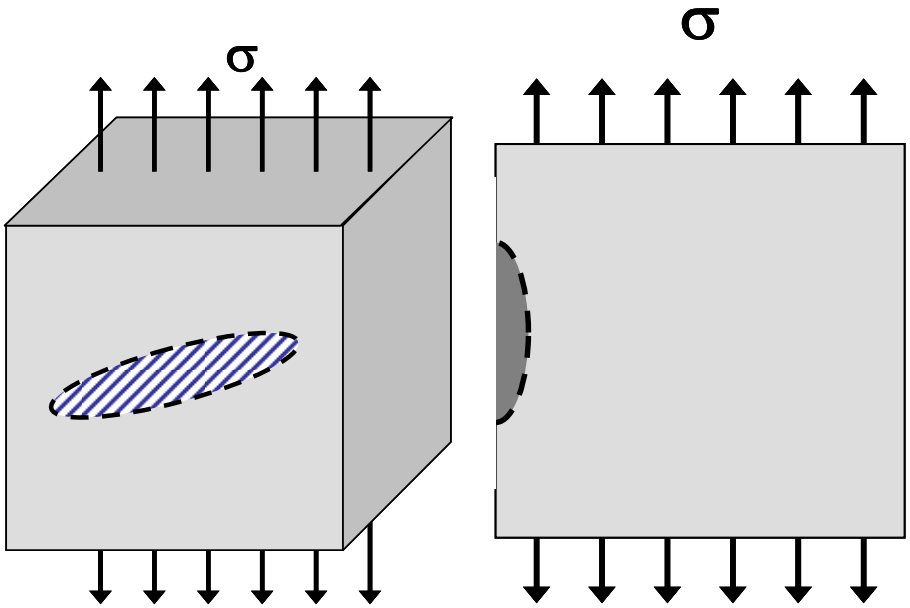

Figure 3.27: Left - embedded elliptical flaw and right – semielliptical surface flaw.

$$K_I = \sigma\sqrt{\frac{\pi a}{Q}} f(\phi) \quad (3.7)$$

$$Q = 1 + 1.464\left(\frac{a}{c}\right)^{1.65} \quad (3.8)$$

$$f(\phi) = \left[\sin^2(\phi) + \left(\frac{a}{c}\right)^2 \cos^2(\phi)\right]^{\frac{1}{4}} \quad (3.9)$$

The FCG rate information in the da/dN versus ΔK curve and initial flaw sizes from fractography (posted with the results in Chapter 4) were combined with these calculations from these equations using the AFGROW software to predict the cycles to failure as a function of initial flaw size, which provided a key comparison to the fatigue life variability assessment.

The embedded elliptical and semielliptical surface flaws were the two geometries studied. AFGROW didn't have the capability to simulate these flaws for a specimen of circular cross-section so the dimensions of the cylindrical dogbone specimens used in fatigue testing were converted to dimensions assuming a square cross section of equivalent area, the same as seen in Figure 3.27. The 6.35 mm diameter converted to a square with a side of 5.63 mm. The 5.63 mm was more than ten times greater than the maximum powder dimension size of 500 μm in the Ti64+1B material.

The tensile properties and fatigue crack growth test conditions were necessarily programmed into AFGROW to make the worst case fatigue life predictions for each stress level. The tabular data capability of AFGROW utilizes the Walker equation on a point-by-point basis (Harter T-Method) to extrapolate or interpolate fatigue S-N and crack growth data for any R value as long as a crack growth curve (da/dN vs. ΔK) is

either provided from a FCG test conducted by the user or found for the same or similar material within AFGROW's material databases (Harter, 2006: 34-38). The Harter T-Method and NASGRO databases were also compared with this study's fatigue crack growth results, which are presented in Chapter 4. These databases contain crack growth information for a wide range of standardized processes used in producing Ti64 material.

IV. Results and Discussion

Fatigue Life Results

The fatigue life of Ti64-1B was evaluated at a stress ratio of 0.1 for three stresses: 655 MPa, 758 MPa, and 862 MPa. The choice of these stress levels was based upon targeted lifetime ranges of interest to the titanium design community. 20 tests were conducted for each stress, all performed at room temperature in laboratory air conditions. The results from these tests are shown for each of the three stresses in Tables 4.1, 4.2, and 4.3 respectively and in Figure 4.1. The average life and standard deviation in life, a measure of variability or scatter, increased with decreasing stress level. At the two lower stress levels, approximately two orders of magnitude of variability were observed. These results were consistent with the research of Jha et al (2003:1638, 2004:1956, 2005:144, 2005:344, and 2005:1297).

Table 4.1: Fatigue variability data for Ti64+1B at lowest stress level of 655 MPa.

Stress Level	9.41E+05
655 MPa / 95 ksi	6.99E+06
	2.12E+06
	1.65E+06
Statistics for N (Cycles)	4.74E+06
Average (Logarithmic)	2.66E+06
1.47E+06	7.93E+04
Minimum	8.37E+05
7.93E+04	8.38E+05
Maximum	1.63E+06
6.99E+06	3.71E+06
Standard Deviation	2.50E+06
1.77E+06	6.89E+05
Order of Magnitude	9.43E+05
(= LOG(Max divided by Min))	7.34E+05
1.9	2.31E+06
	2.88E+06
	6.40E+05
	4.76E+06
	9.29E+05

Table 4.2: Fatigue variability data for Ti64+1B at middle stress level of 758 MPa.

Stress Level	1.17E+05
758MPa / 110 ksi	5.55E+05
	1.34E+06
	9.63E+03
Statistics for N (Cycles)	1.95E+05
Average (Logarithmic)	1.57E+05
1.27E+05	1.03E+05
Minimum	9.09E+04
9.63E+03	1.38E+05
Maximum	8.46E+04
1.34E+06	8.30E+04
Standard Deviation	1.10E+05
2.90E+05	1.60E+05
Order of Magnitude	8.03E+04
(= LOG(Max divided by Min))	1.41E+05
2.1	1.22E+05
	2.07E+05
	1.23E+05
	7.12E+04
	1.08E+05

Table 4.3: Fatigue variability data for Ti64+1B at highest stress level of 862 MPa.

Stress Level	4.98E+04
862 MPa / 125 ksi	5.05E+04
	2.00E+04
	4.52E+04
Statistics for N (Cycles)	5.44E+04
Average (Logarithmic)	4.29E+04
4.52E+04	4.81E+04
Minimum	5.10E+04
2.00E+04	4.62E+04
Maximum	4.21E+04
5.44E+04	5.27E+04
Standard Deviation	4.53E+04
7.23E+03	4.18E+04
Order of Magnitude	4.92E+04
(= LOG(Max divided by Min))	5.04E+04
0.4	4.59E+04
	4.90E+04
	5.00E+04
	4.00E+04
	4.53E+04

The complete fatigue results for the Ti64+1B material compared well, with the exception of two low outliers, with the prealloyed Ti64 powder metallurgy parts data from Froes and Eylon (1990) as well as results from the Ti64 high cycle fatigue program (Gallagher and Nichols, 2004). Figure 4.1 provides a plot of the data from this research

project along with a envelope of prealloyed powder metallurgy Ti64 from Froes and Eylon and the data from the HCF program.

The increased variability was found to be the combination of multiple failure types: failure initiating at the surface generally corresponding to longer fatigue lives and failures initiating at inclusions, mostly but not exclusively in the subsurface, generally corresponded to shorter fatigue lives. With decreasing stress level, these two failure types diverged increasingly from each other as shown in Figure 4.2. As a third and more rare type, a few fatigue specimens showed inclusions at or very near the surface and exhibited the lowest life results. The next step was to investigate the cause of the worst case mechanism, inclusion failure by performing fractography on a sampling of the broken fatigue specimens.

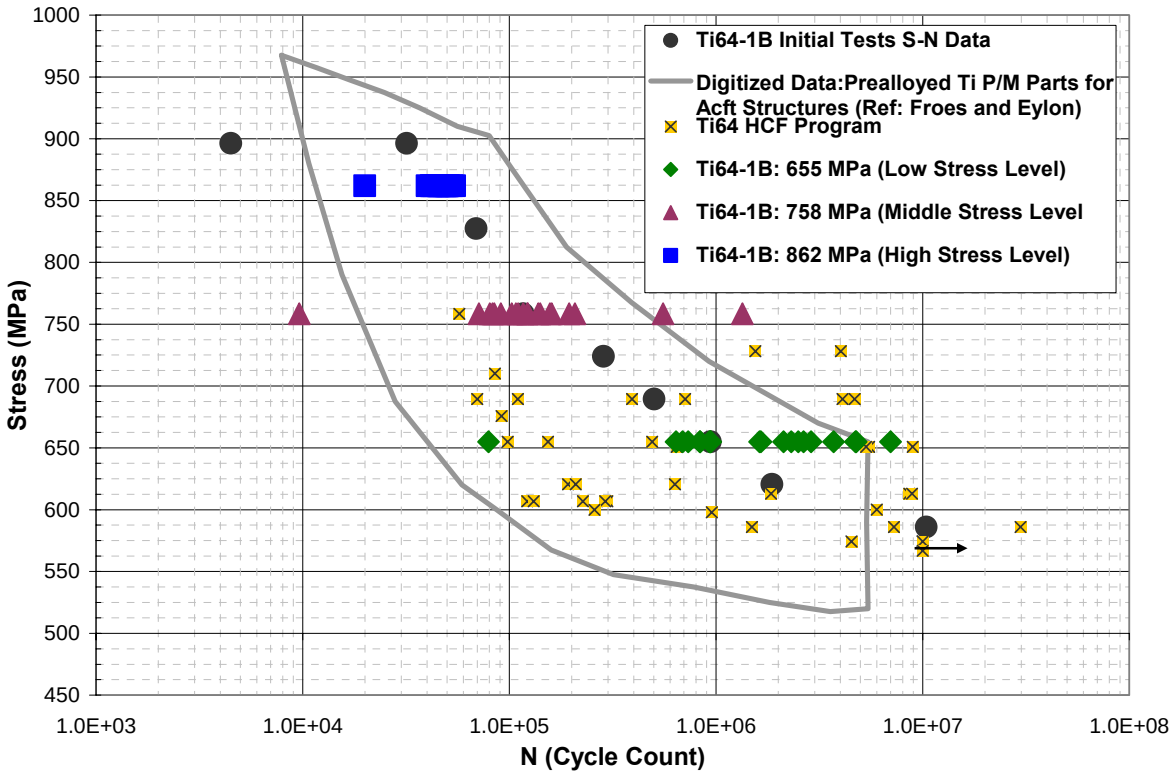

Figure 4.1: Complete fatigue variability data for Ti64+1B.

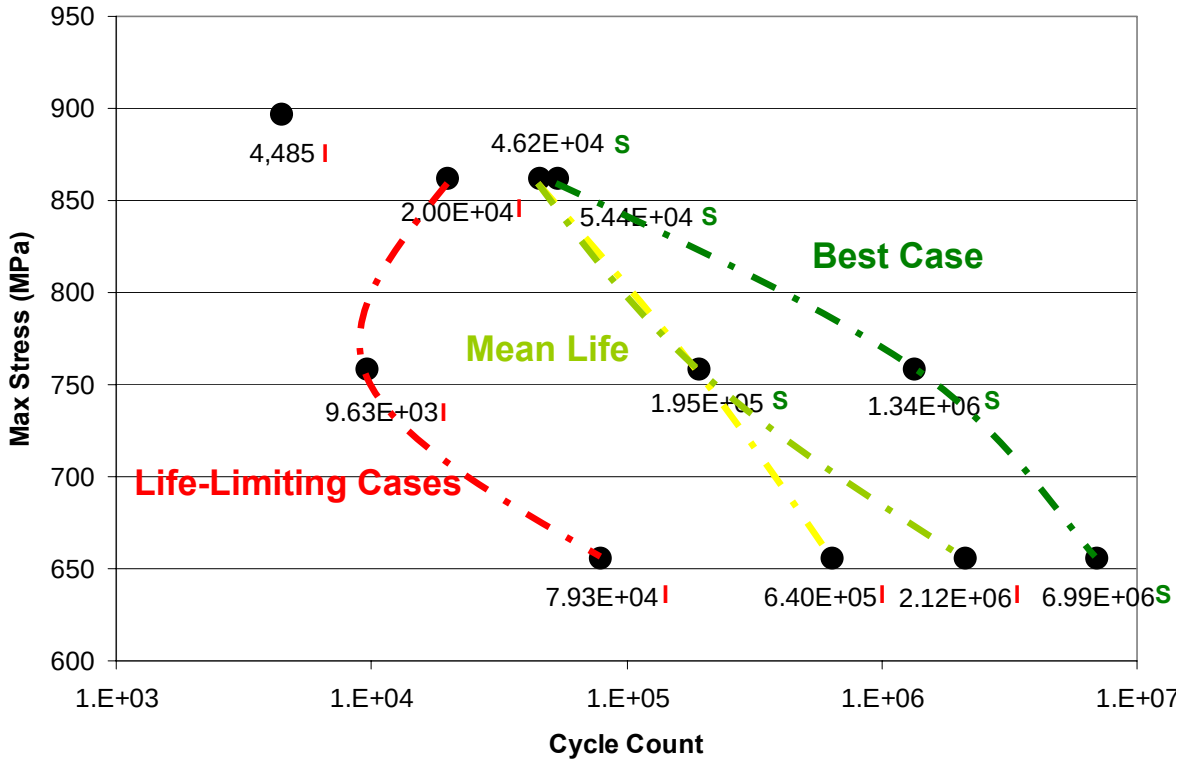

Figure 4.2: Observation of Failure types diverging as a function of σ_{max}-level. Inclusions are represented with an "I" and surface initiated failures with an "S".

Fractography

Fractography was done on the fatigue samples using Leica 360 FE and FEI Quanta scanning electron microscopes (SEM) using mostly secondary electron mode but also back-scattered electron mode. These analyses, performed on a sampling of 11 of the 67 fatigue specimens, exhibited a variety of failure types. The cycle counts and failure types for the 11 specimens singled out for fractography are all included in Figure 4.2. Before delving into the fracture surfaces as imaged in the SEMs, the observations depicted in Table 4.4 were made visually without the help of any microscope or other magnification.

Table 4.4: Fatigue variability data for prealloyed Ti64+1B material for three stress levels with a corresponding failure initiation description.

862 MPa		758 MPa		655 MPa	
4.98E+04	**S**	1.17E+05	**S**	9.41E+05	**I**
5.05E+04	**S**	5.55E+05	**I**	6.99E+06	**S**
2.00E+04	**I**	1.34E+06	**S**	2.12E+06	**I**
4.52E+04	**S**	9.63E+03	**I**	1.65E+06	**I**
5.44E+04	**S**	1.95E+05	**S**	4.74E+06	**S**
4.29E+04	**S**	1.57E+05	**I**	2.66E+06	**I**
4.81E+04	**S**	1.03E+05	**S**	7.93E+04	**I**
5.10E+04	**S**	9.09E+04	**S**	8.37E+05	**I**
4.62E+04	**S**	1.38E+05	**S**	8.38E+05	**I**
4.21E+04	**S**	8.46E+04	**S**	1.63E+06	**I**
5.27E+04	**S**	8.30E+04	**S**	3.71E+06	**I**
4.53E+04	**S**	1.10E+05	**S**	2.50E+06	**I**
4.18E+04	**S**	1.60E+05	**S**	6.89E+05	**I**
4.92E+04	**S**	8.03E+04	**S**	9.43E+05	**I**
5.04E+04	**S**	1.41E+05	**S**	7.34E+05	**S**
4.59E+04	**S**	1.22E+05	**S**	2.31E+06	**S**
4.90E+04	**S**	2.07E+05	**S**	2.88E+06	**I**
5.00E+04	**S**	1.23E+05	**S**	6.40E+05	**I**
4.00E+04	**S**	7.12E+04	**S**	4.76E+06	**I**
4.53E+04	**S**	1.08E+05	**S**	9.29E+05	**I**

Key:

S = Surface and subsurface non-inclusion initiated failure

I = Inclusion initiated failure; primarily subsurface*****

At the low-cycle, highest stress combinations at 862 MPa, surface initiated failures were dominant occurring in all but one of the specimens. At the middle stress of 758 MPa, surface initiated failures without inclusions still dominated but this time in only 17 out of 20 of the specimens. For the high-cycle, low stress of 655 MPa, 16 of the 20 specimens had failures originating from inclusion sites mostly in the subsurface. The sampling for microscopy (made bold in Table 4.4) included specimens corresponding to the worst case, average, and best case cyclic counts for the three stress levels. An extra average life specimen from the 655 MPa stress and a low outlier at a higher stress of 896 MPa from initial S-N fatigue testing were also examined.

The first specimen of concern is the additional outliers coming from the initial S-N testing at the stress of 896 MPa. When this test was performed early on, it failed much earlier than expected at 4,485 cycles. The test was repeated and a lifetime of 31,816 cycles was achieved. The result of 4,485 cycles was attributed to an early initiation at an inclusion.. Figure 4.3 shows the location of the flaw on the specimen's fracture surface. The secondary and backscatter images of the flaw are shown in Figure 4.4. The

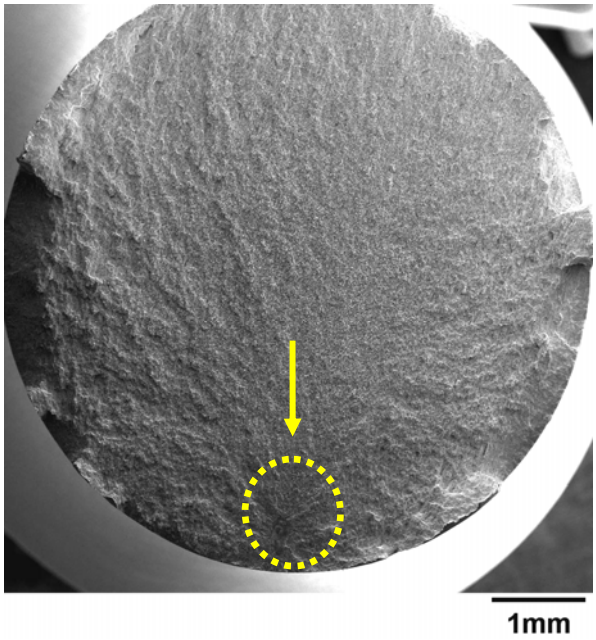

Figure 4.3: Fracture surface for fatigue specimen tested at 896 MPa failing at 4,485 cycles.

images indicate that the initial flaw size was approximately 400 by 200 microns, which is fairly large but within the allowable 500 micron size for -35 mesh size powder. Energy dispersive spectroscopy (EDS) analysis was performed on this fatigue specimen. The analysis resulted in the EDS spectra of Figures 4.5 and 4.6. Figure 4.5 shows the analysis of the material adjacent to the flaw and identified the presence of titanium, aluminum, and vanadium as expected. However, the analysis was performed close enough to the flaw and suggested small levels of iron, chromium, manganese, silicon on the fracture

surface. Figure 4.6 shows the EDS analysis for the inclusion defect. At the heart of the flaw, the highest peaks are of iron, manganese, chromium, vanadium and nickel. This suggests that the prealloyed Ti64+1B powder was contaminated by particles of steel-like composition during processing. A silicon peak was also detectd and the matrix elements had small peaks relative to the above mentioned contaminants.

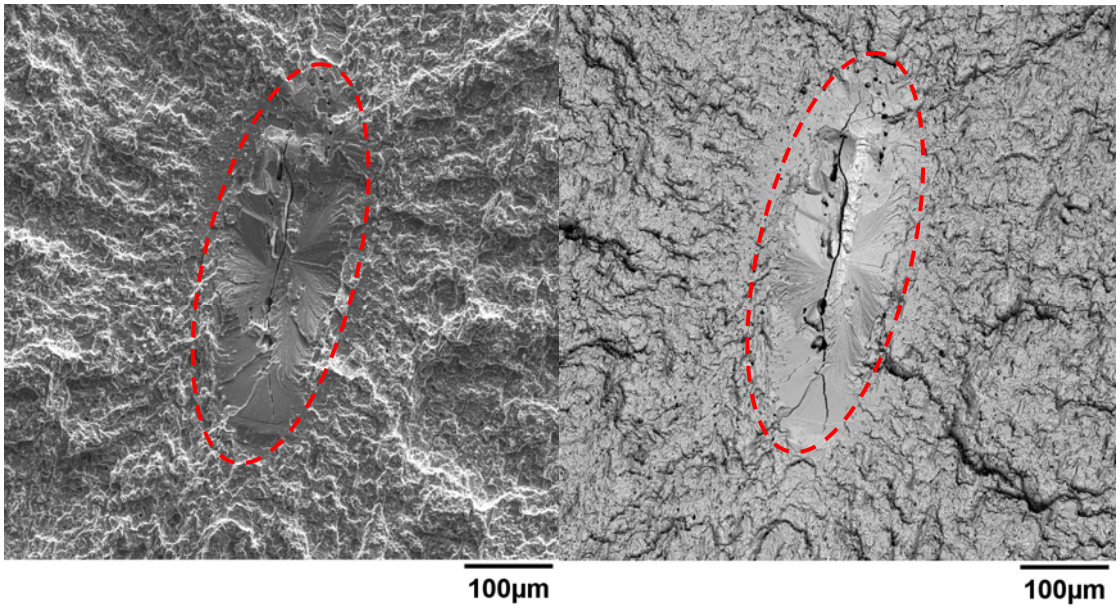

Figure 4.4: Inclusions shown in secondary imaging on left and backscatter imaging on right for fatigue specimen tested at 896 MPa failing at 4,485 cycles.

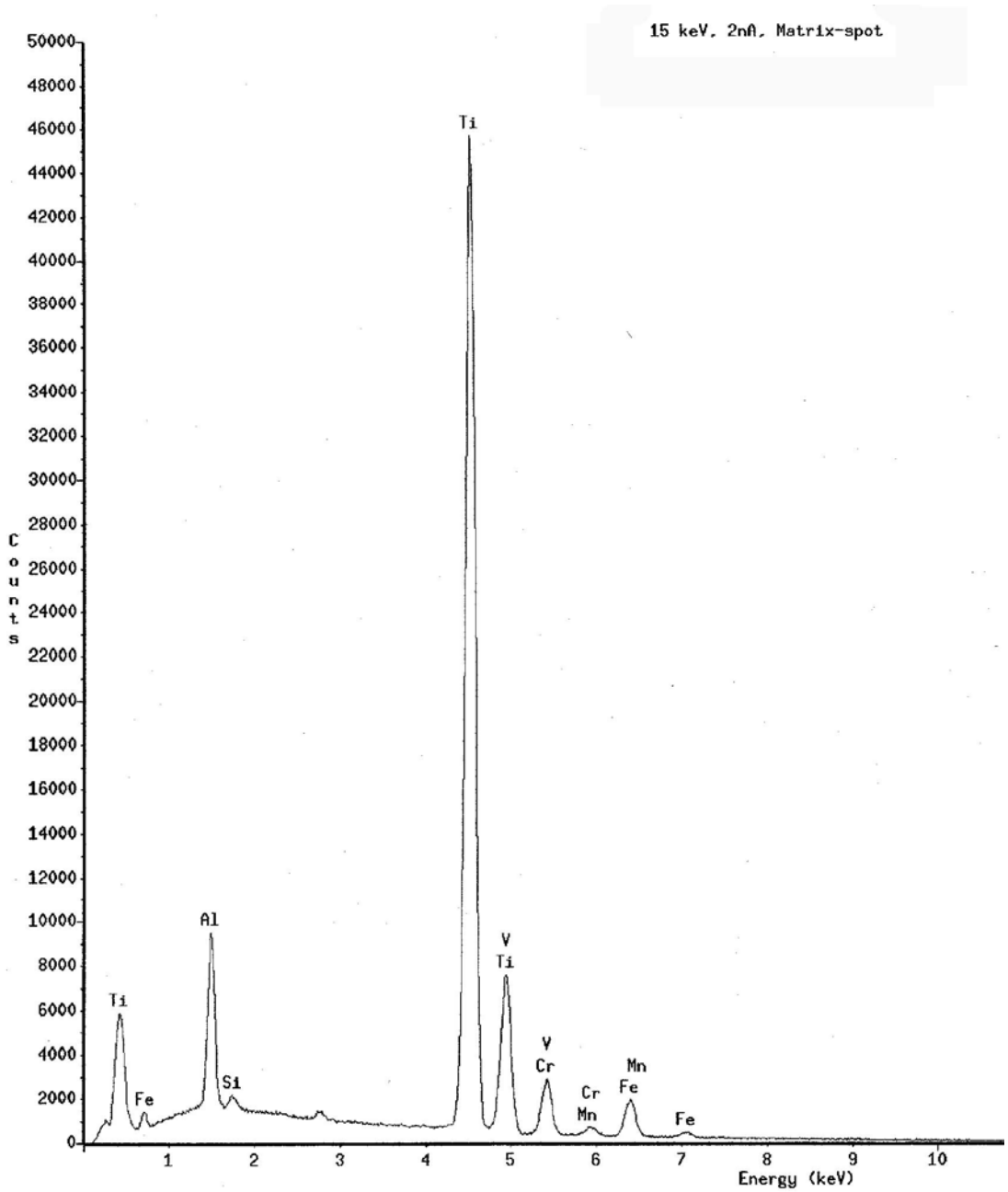

Figure 4.5: EDS x-ray analysis of Ti64 matrix for fracture surface of Ti64+1B specimen tested at a stress of 896 MPa failing at 4,485 cycles.

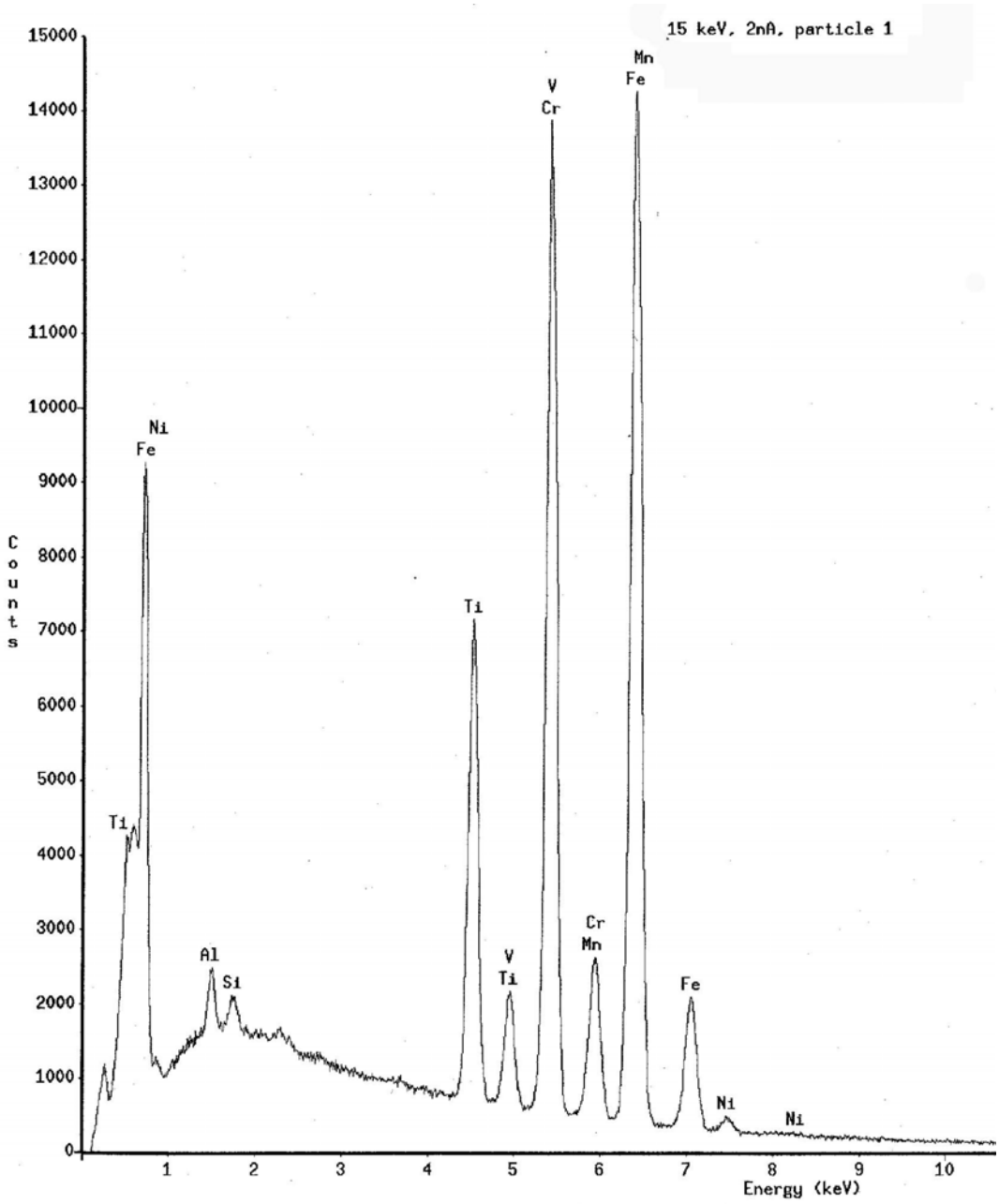

Figure 4.6: EDS x-ray analysis of inclusion flaw on fracture surface of Ti64+1B specimen tested at a stress of 896 MPa failing at 4,485 cycles.

The lowest fatigue life for the 60 tests run for studying variability, which drew immediate attention, actually occurred at the middle stress of 758 MPa and failed at 9,629 cycles. The inclusion observed visually on the fracture surface was one of the largest from all of the specimens. The fractographs taken of the inclusion, shown in Figure 4.7,

confirmed that extrinsic matter contaminated the material. The secondary image on the left shows a substantial amount of charging making it difficult to ascertain the size of the flaw. The backscattered electron image on the right shows that the inclusion was large and if modeled as an ellipse was approximately 375 by 225 μm in size. These estimated dimensions of the effected area may be a bit large since the images show that many pieces of the inclusion broke off and surrounded the major piece of the inclusion. However, the worst case must be assumed and the size is still below the largest possible powder size for this material.

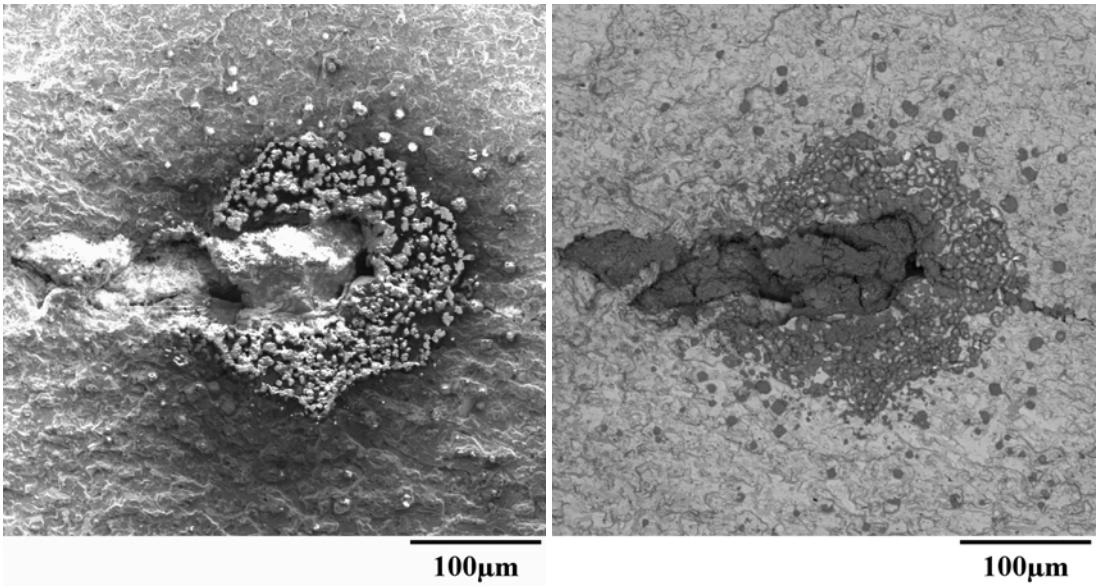

Figure 4.7: Secondary (left) and backscatter images of fracture surface for Ti64+1B specimen tested at 758 MPa and failing at 9,629 cycles.

The EDS spectrographs of both the inclusion and base material are provided in Figures 4.8 and 4.9. Figure 4.8 shows the analysis in the center of the inclusion. The largest peak indicated the presence of calcium. Magnesium, silicon, oxygen, carbon, and iron are also present, several of which are typical contaminants in materials produced via powder metallurgy (Peebes and Kelto, 1980:57). The EDS spectrograph of Figure 4.8

was observed in the matrix material sufficiently far away from the inclusion and shows the expected titanium, aluminum, and vanadium peaks.

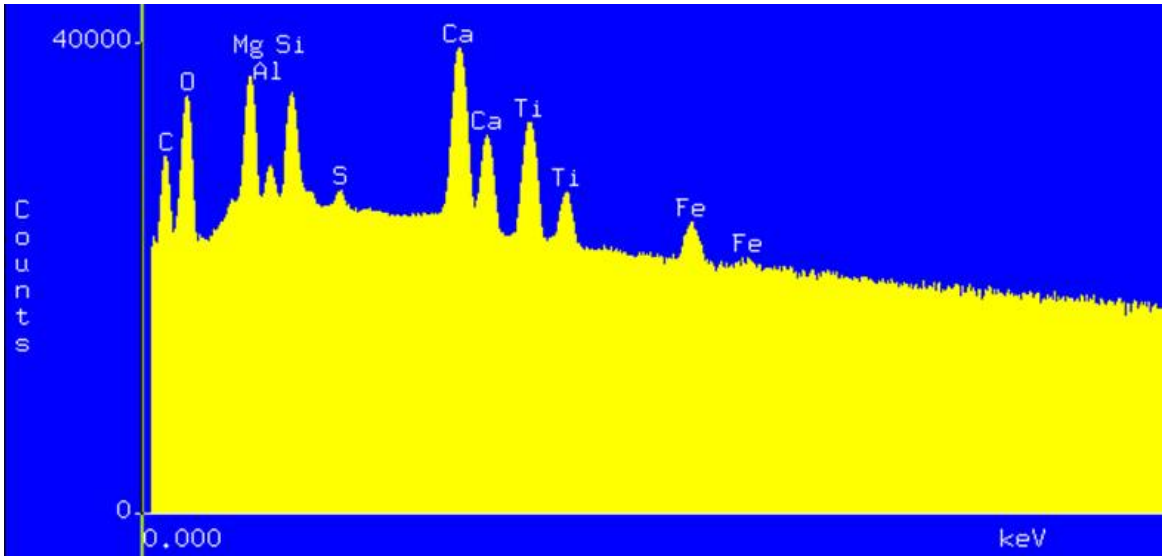

Figure 4.8: EDS spectrograph of center of inclusion in Ti64+1B specimen tested at 758 MPa and failing at 9,629 cycles.

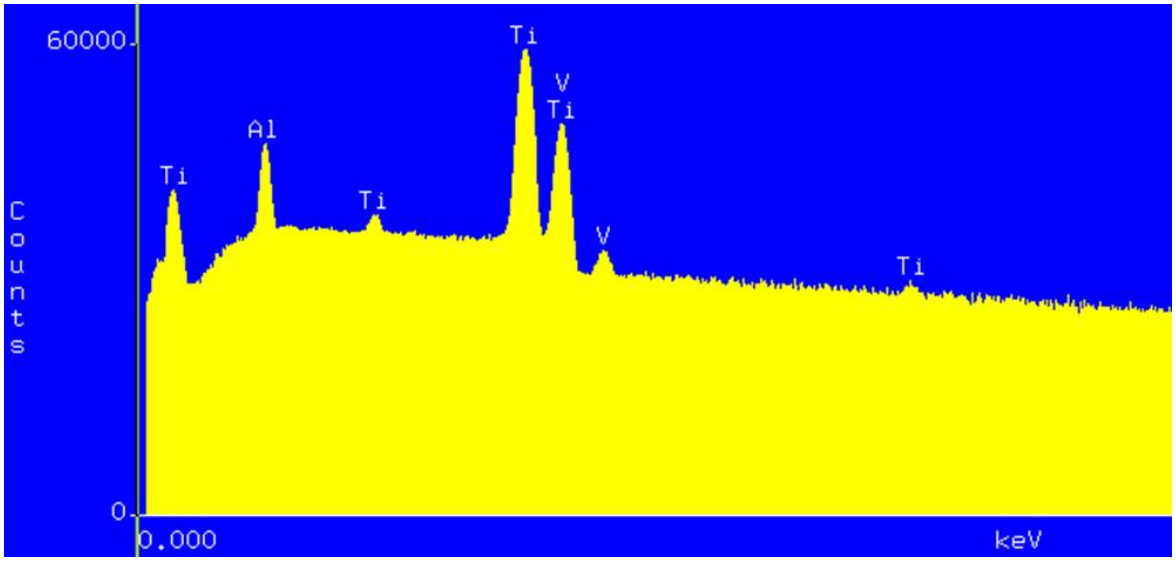

Figure 4.9: EDS spectrograph of matrix material away from inclusion for a Ti64+1B specimen tested at 758 MPa and failing at 9,629 cycles.

Only the two lowest life outliers have been examined in the main body of this study. Additional fractography work for this study is included in Appendix A. From all 11 specimens examined in the SEMs, the subsurface crack initiation sites eminating from

inclusions were easy to locate. Most of the fractography was performed in secondary electron mode. Therefore, the inclusions were not as distinguishable as they would be had a backscatter electron detector beam been employed, but the inclusion sites were obvious on the fracture surface to the naked eye. Noteable was that large TiB particles were not observed at any of the initiation sites examined. For the specimens with non-inclusion dominated crack initiation sites, failing primarily at the surface, it was much more difficult to determine the source of crack nucleation. It can be that for specimens that failed at sites not involving inclusions, the majority of the life was spent initiating a crack. This will be supported with crack growth analyses later in this chapter. However, it was unnecessary to search for further damage mechanisms at this point because the fatigue life results for the surface initiated cracks of the Ti64+1B specimens agreed well enough with sources of fatigue data for Ti64. Most important was that inclusions were determined to be life limiting for the Ti64+1B material studied in this thesis. The lower limit was clearly not driven by the presence of TiB whiskers or particles.

Analysis of Fatigue Life Variability

The probability of failure (POF), also referred to as a cumulative distribution function (CDF) or lognormal probability function, is shown in Figure 4.9 for all three stress levels. The fatigue data has been plotted in lognormal probability space. At the two lower stress levels, 655 MPa and 758 MPa, there was poor concurrence between the experimental results and the related CDFs depicted with straight lines. Similar to the statistics and graphics from Tables 4.1, 4.2, and 4.3 and Figure 4.1, Figure 4.10 demonstrates two orders of magnitude of variability for the two lower stress levels. By extrapolating the CDFs out to the POF of 0.1% (the 1 in 1000 failure criteria commonly

used for fracture critical turbine engine components), it was evident that much lower worst case lives were predicted for the lower stress levels that what was obtained through fatigue variability testing. This suggested that a different mechanism of crack initiation played a significant role in the fatigue life of the lowest life specimens. From fractography, it has already been suggested that for non-inclusion dominated failures, the majority of the specimen life was spent initiating a crack.

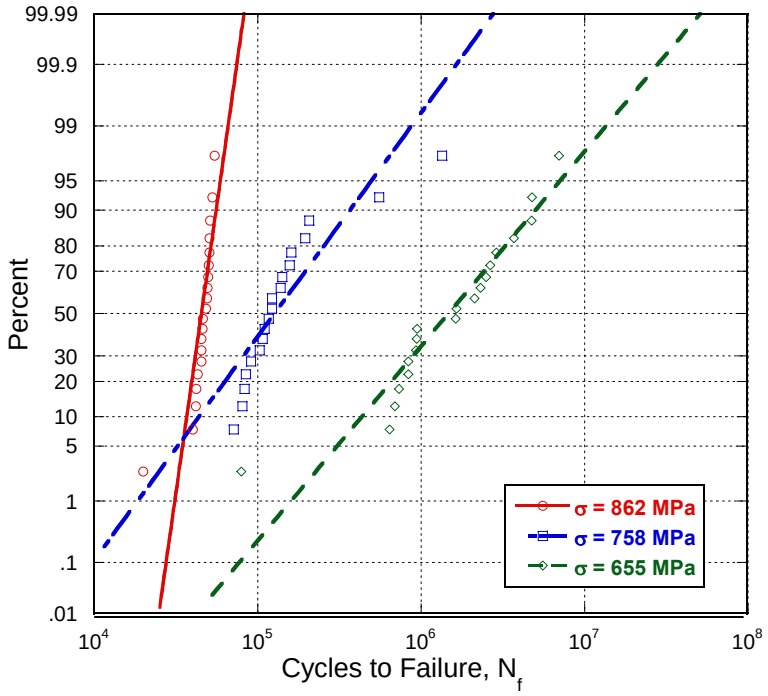

Figure 4.10: Representation of fatigue variability results for rolled Ti64+1B plate in terms of probability of failure for all three stress levels.

The extent to which inclusions in the Ti64+1B rolled plate material affected the variability in fatigue life is demonstrated in POF plots for the two lower variability stresses in Figures 4.11 and 4.12. Here, each data set is broken into two populations. One data set represents the specimens that didn't fail at inclusions and the other set represents the specimens that did fail at inclusions. For the lower stress in Figure 4.11, the combined data had a 0.1% POF at about 60,000 cycles. Most of the failure initiation

sites at the lower stress were from inclusions but without the inclusions the cycle count at the 0.1% POF doubled to about 120,000. At the middle stress in Figure 4.12, filtering out the inclusions also resulted in doubled the 0.1% POF prediction from around 9,000 to 20,000 cycles. Furthermore, a 0.1% POF for the inclusion data only of both lower stresses was carried out. In the lowest stress case, the effect was negligible. However, at the middle stress of 758 MPa in Figure 4.12, a disastrous near zero cycle count was predicted. The POF inclusion extrapolation at the middle stress is based only upon three data points so this prediction carried little impact but could be interpreted as a major warning concerning the threat that inclusions pose on the lower limit to fatigue variability.

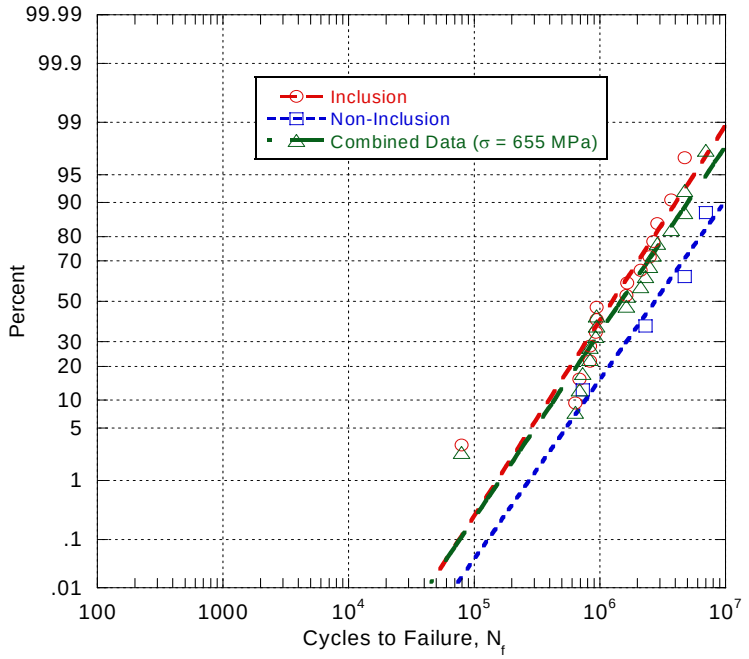

Figure 4.11: Fatigue variability results of rolled Ti64+1B plate at stress of 655 MPa in terms of probability of failure. The mechanism of inclusion is separated from the other data to demonstrate its affect upon the fatigue life.

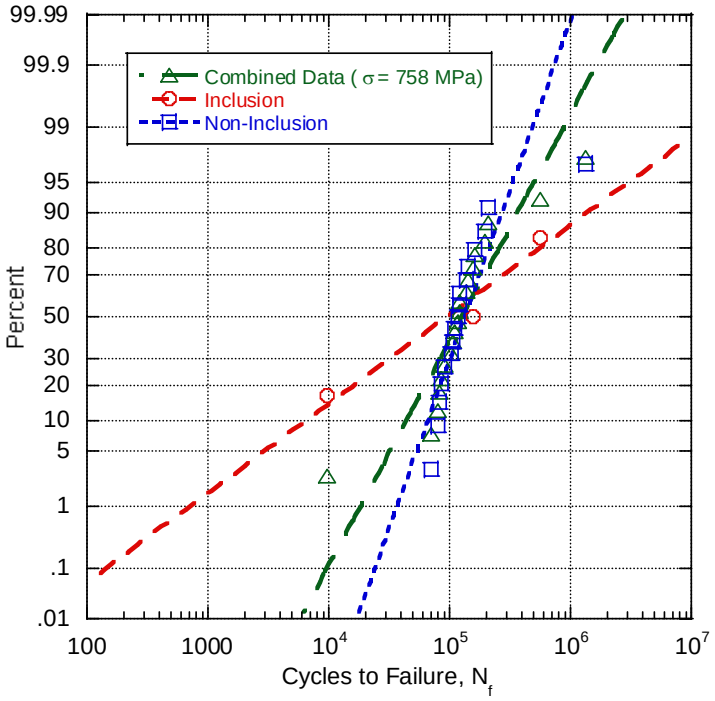

Figure 4.12: Fatigue variability results of rolled Ti64+1B plate at stress of 758 MPa in terms of probability of failure. The mechanism of inclusion is separated from the other data to demonstrate its affect upon the fatigue life.

Fatigue Crack Growth Results

The fatigue crack growth (FCG) behavior of Ti64+1B was evaluated from only one compact tension C(T) specimen. There were plans to run a repeat test, however, equipment control difficulties resulted in overloads that fractured the other three specimens just after precracking. A large quantity of direct-current electric-potential (DCEP) FCG data was collected during all portions of the testing consisting of: pre-cracking, ΔK-decreasing threshold testing, and constant P_{max}-constant testing. In order to obtain a da/dN versus ΔK curve for the material, several data manipulation steps were necessary on the DCEP data. These steps have been plotted in Figures 4.13 and 4.14 for the K-decreasing and P_{max}-constant testing, respectively. The K-decreasing and P_{max} test portions were analyzed separately. Optical crack length data from the front and back of

the C(T) specimen was periodically recorded during the testing and was corrected afterwards to include tunneling observed on the surfaces. The tunneling accounted for most of the difference between the initial DCEP data. At the end of precracking, the difference between the DCEP data and fracture surface (taking into account tunneling) was approximately 1 mm. This number increased to 1.7 mm at the end of the ΔK decreasing test and then back down to about 1 mm again by the end of P_{max}-constant testing. This is demonstrated in Figures 4.13 and 4.14 as the difference between the dark blue squares and the large ___ circles. The raw DCEP data was ultimately corrected to match the "optical and tunneling adjustment" points, which were considered the best measure of optical crack length.

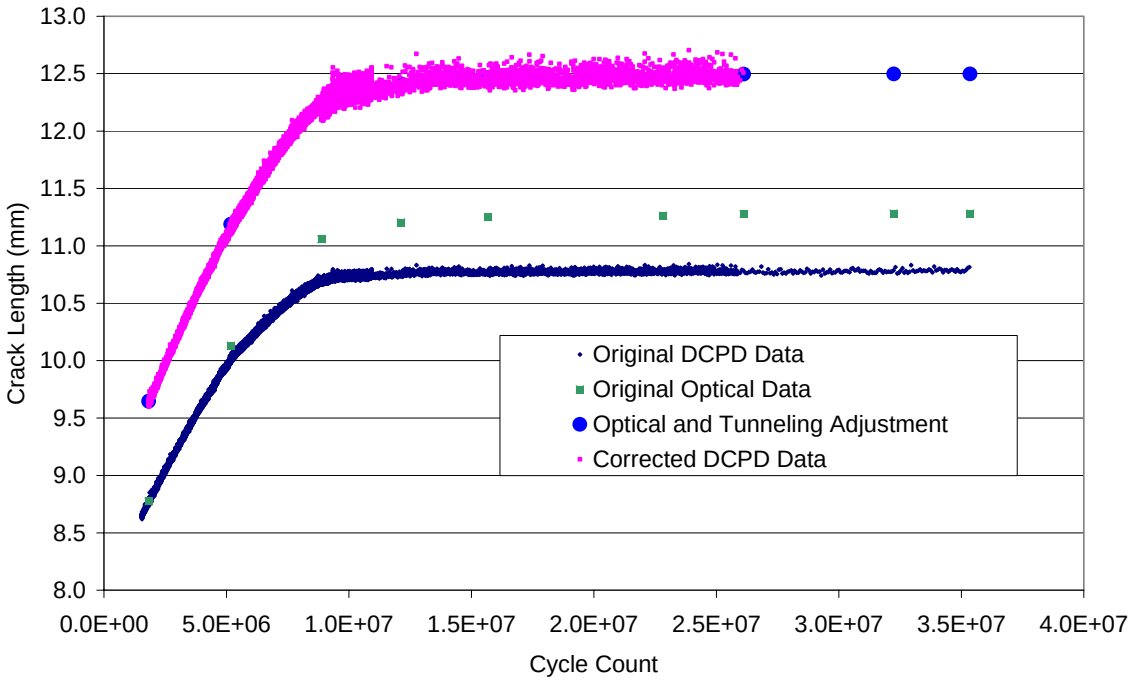

Figure 4.13: Correction steps of fatigue crack growth results for threshold or ΔK-decreasing testing for Ti64+1B C(T) specimen.

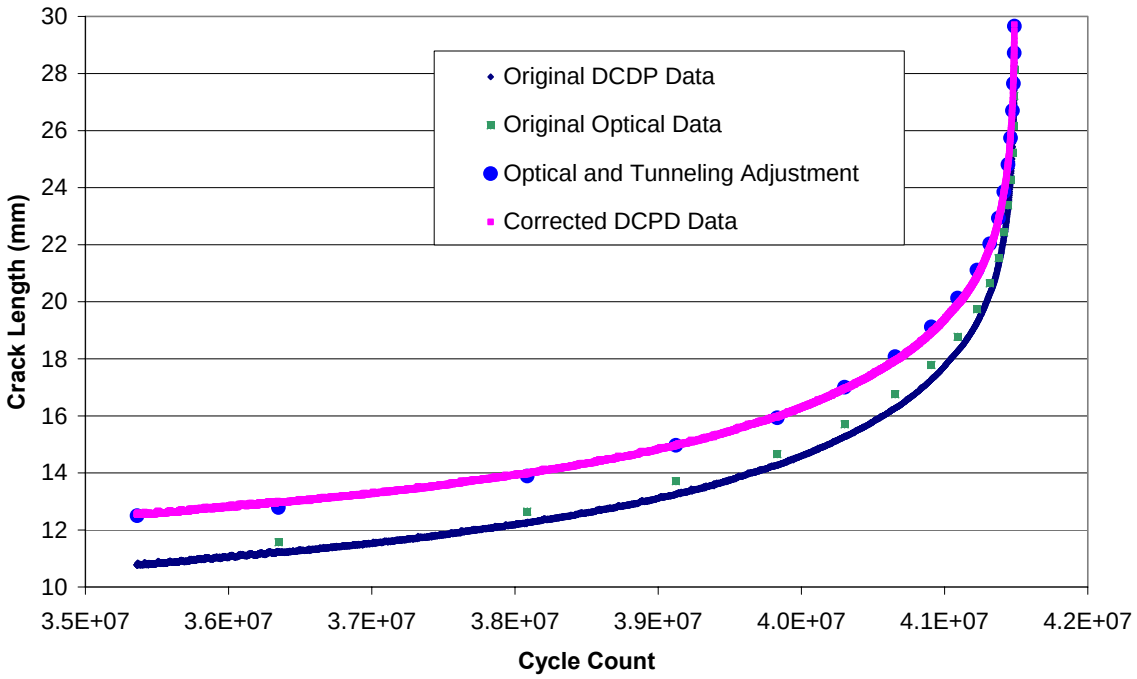

Figure 4.14: Correction steps of fatigue crack growth results for constant P_{max} testing for Ti64+1B C(T) specimen.

The fatigue crack growth data for theTi64+1B rolled plate material, da/dN versus ΔK, was subsequently determined after the data was further reduced and smoothed using a program that utilized a least squares fit containing 15 points at a time and a Δa (crack length increment) of 0.05 mm. The method employed by this program has been explained thoroughly in ASTM E 647-00 Appendix X1.2. The reduced, smoothed DCEP results were compared against the corrected DCEP results in Figures 4.15 and 4.16 for the K-decreasing and P_{max} test portions. The reduced, smoothed DCEP results correlate well with the previous DCEP results. The code used to smooth the corrected DCEP results also converted the crack length vs. cycle count data to a change in crack length per cycle versus the change in stress intensity factor. This important da/dN versus ΔK result is shown in Figure 4.17 merging both test portions.

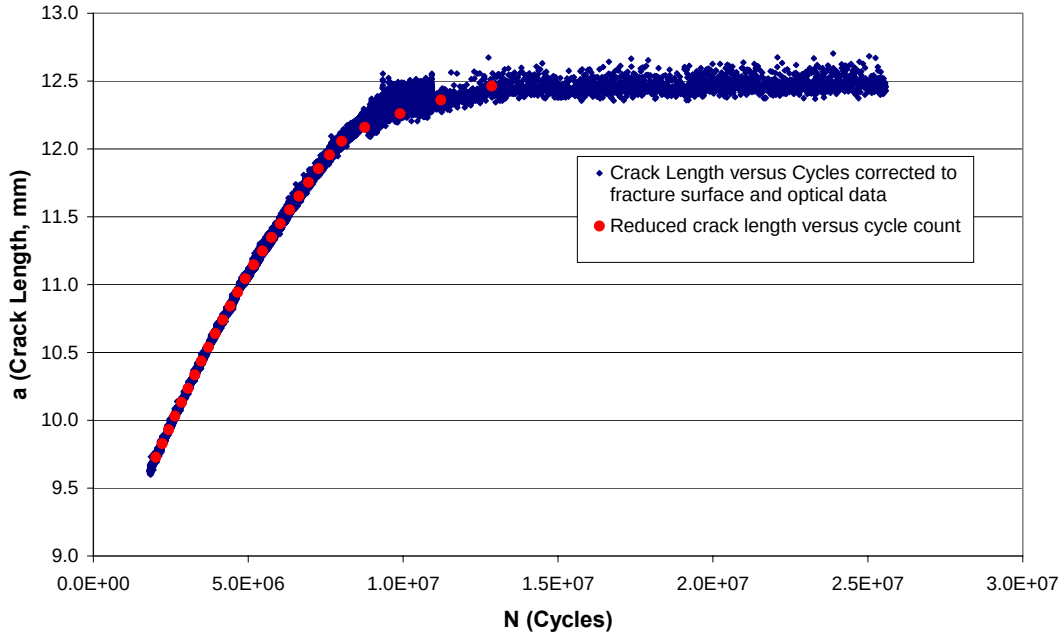

Figure 4.15: Reduction of fatigue crack growth results for threshold or K-decreasing testing for Ti64+1B C(T) specimen.

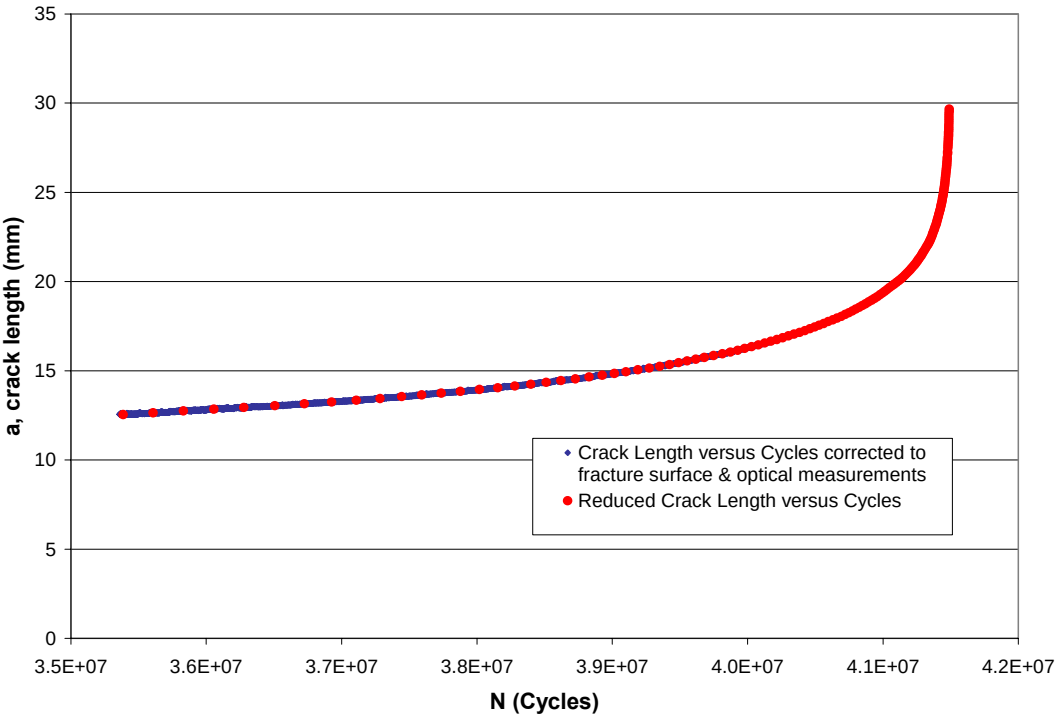

Figure 4.16: Reduction of fatigue crack growth results for constant P_{max} testing for Ti64+1B C(T) specimen.

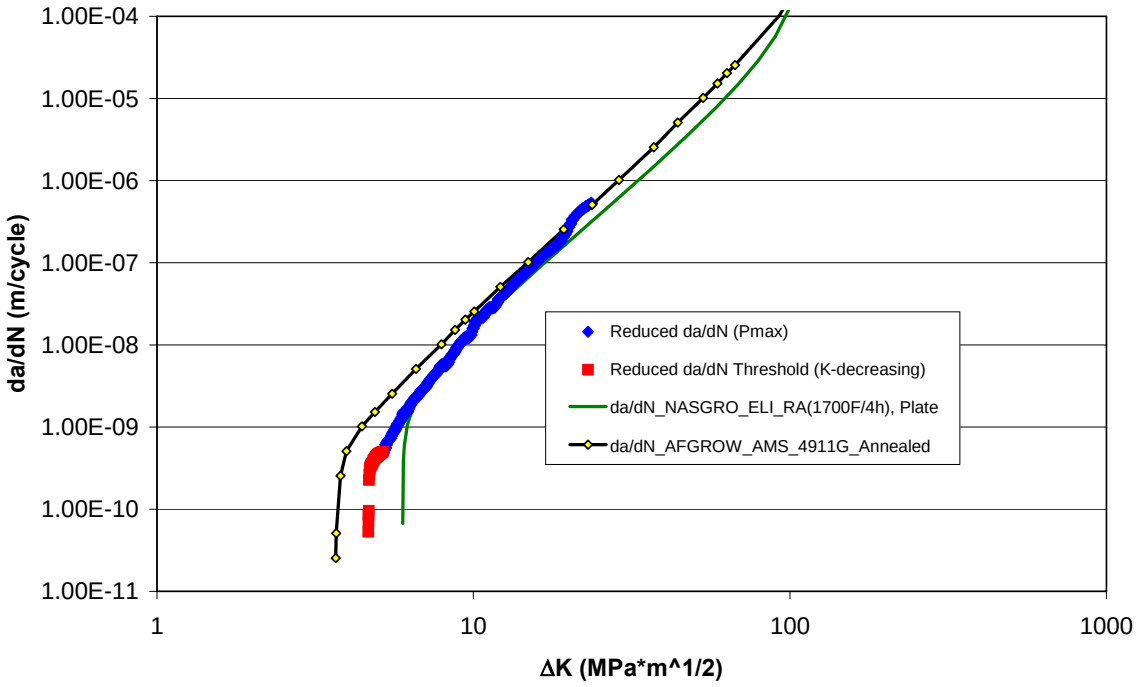

Figure 4.17: Complete Ti64-1B crack growth compared with NASGO and AFGROW databases for Ti64.

Crack growth information from two credible databases found in AFGROW (Harter, 2006: 48-59) was included in Figure 4.17. The first set was for extra low interstitial (ELI) Ti64 plate from the NASGRO database. The NASGRO equation was the equation used in NASA's crack growth life prediction program (Forman and Mettu, 1992). The second data set was AFGROW's Ti64 AMS 4911G Annealed (Harter, 1994). The results of the comparison were positive—the fatigue crack growth behavior of Ti64+1B closely resembled the behavior of Ti64 from the two databases.

In order to relate the crack growth rate behavior of the Ti64+1B compact tension specimen with the fatigue variability analysis, a hyperbolic arctangent model was fit to the crack growth rate data seen in Figure 4.17 so that the resulting crack growth curve could be easily fed into AFGROW. The hyperbolic arctangent model is shown in

Equation 4.1 where C_1, C_2, C_3, and C_4 are regression coefficients:

$$\log\left(\frac{da}{dN}\right) = C_1 \arctan h\{C_2\left[\log(\Delta K) + C_3\right]\} + C_4 \qquad (4.1)$$

Larsen and others used the hyperbolic arctangent equation because of the equation's ability to bend more abruptly than other models and therefore provide a better representation of near threshold data (Larsen and others, 1996: 237-255). The combined over 200 points from the reduced crack growth data, with the threshold portion of the crack growth data being more heavily weighted, were used to determine and fit the 4 constants of Equation 4.1 . The constants were determined to be: $C_1 = 1.55$, $C_2 = 2.37$, $C_3 = -1.04$, and $C_4 = -7.67$. Thirty points along the hyperbolic arctangent fit were then imported into AFGROW to allow FCG lifetime calculations for predicting the fatigue lower limit at each of the stresses of 655 MPa, 758 MPa, and 862 MPa. The calculations, assuming a range of initial flaw size, are useful for demonstrating the effect of initial flaw size on FCG lifetimes. Assuming a negligible crack initiation life, the FCG lifetimes can be used as a lower limit of the overall fatigue life.

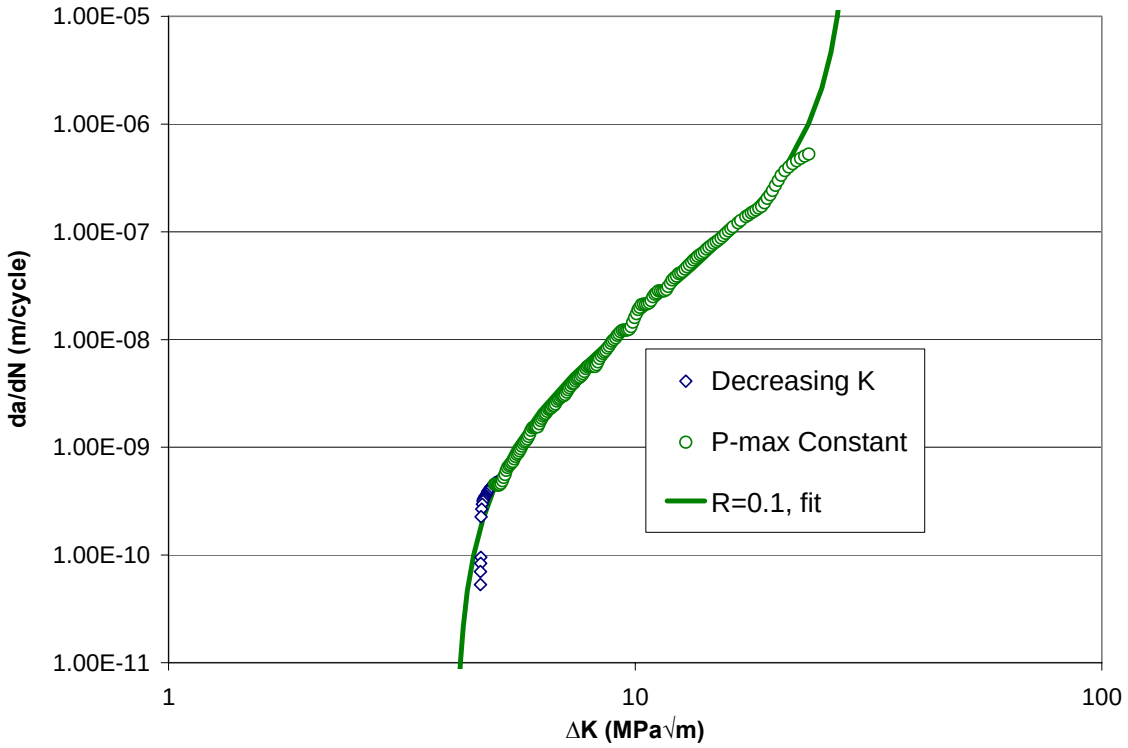

Figure 4.18: Complete Ti64-1B crack growth compared hyperbolic arctangent fit.

The tabular look-up crack growth rate capability within AFGROW was utilized because it allows users to input their own crack growth rate curves. Data at the stress ratio of interest was put into AFGROW so that no interpolating was required. AFGROW's ability to perform these calculations for worst case fatigue life at a given stress was particularly useful for Ti64+1B because crack growth rate data on this material was scarce. The necessary fracture mechanics equations for performing this analysis were already built into AFGROW (Harter, 2006: 60).

FCG Predictions

The fatigue lower limit predictions of this section were calculated using the AFGROW software after the mechanical property data of Ti64+1B, the crack growth rate data fit to a hyperbolic arctangent model, and the fatigue crack growth testing conditions were entered into the tabular lookup menu in AFGROW. Based upon the findings of the

fractographic analysis, embedded (subsurface) elliptical flaws at three a/c ratios and the semi-elliptical surface crack flaws at one a/c ratio were simulated to determine the life limiting cycles, N_f, for a variety of crack lengths, 2c, at all three stress levels. The geometry of the full ellipse was 2c for the longer dimension and 2a for the shorter dimension. For the semi-elliptical flaw geometry, the longer dimension was 2c and the shorter dimension was a. The results of this analysis for the stresses of 655 MPa, 758 MPa, and 862 MPa are depicted in Figures 4.19, 4.20, and 4.21 respectively. These plots demonstrate both the sensitivity to aspect ratio for a given crack size and for a given aspect ratio, the sensitivity to crack size.

The AFGROW analysis provided insight into many of the trends in fatigue life for varying flaw sizes and flaw geometry (a/c ratios). As the initial flaw size 2c decreased, fatigue life, N_f, became increasingly sensitive to the initial flaw size. The degree of sensitivity was higher as the a/c decreased or as the initial flaw geometry's became less and less circular. This is evidenced by the near infinite slope of the a/c = 0.33 curve at a stress of 655 MPa in Figure 4.19. In addition, the degree of sensitivity to initial flaw size was also much higher at the lowest stress as indicated by the steepening slopes per a/c ratio going from the highest to the lowest stress. With decreasing stress and decreasing initial flaw size, the ΔK value approaches $\Delta K_{threshold}$. The fatigue life would increase exponentially at this point with such a small da/dN value closer to $\Delta K_{threshold}$, where the fatigue life, N, is the denominator. The highest a/c ratio had the worst N_f results as expected because the crack area was larger. This analysis also included semi-elliptical surface flaws, which proved to be the worst case overall. Inclusions at the surface, even small ones, 2c = 100 μm, had relatively low lives as shown in Figure 4.22.

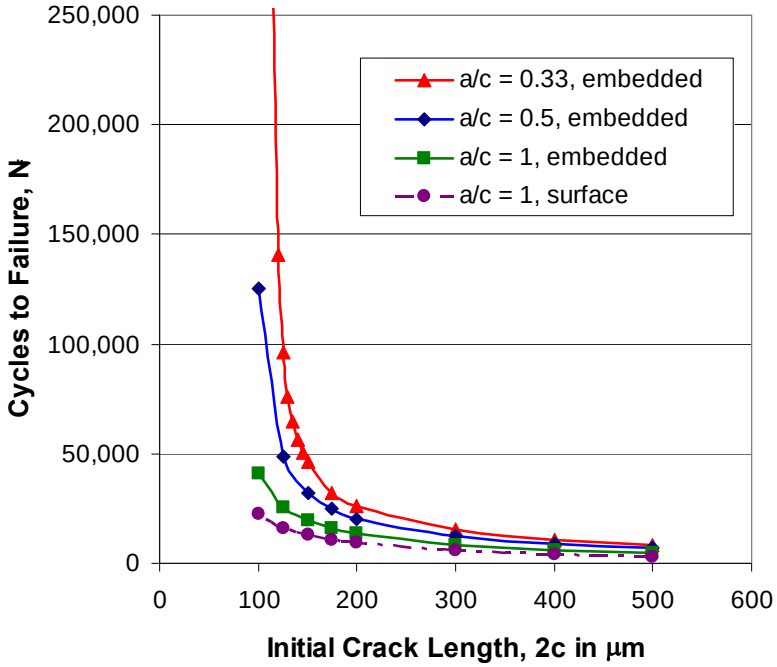

Figure 4.19: AFGROW prediction of worst case cycles to failure for an embedded elliptical flaw at three different a/c ratios and a semielliptical surface flaw at one a/c ratio for Ti64+1B at the stress of 655 MPa.

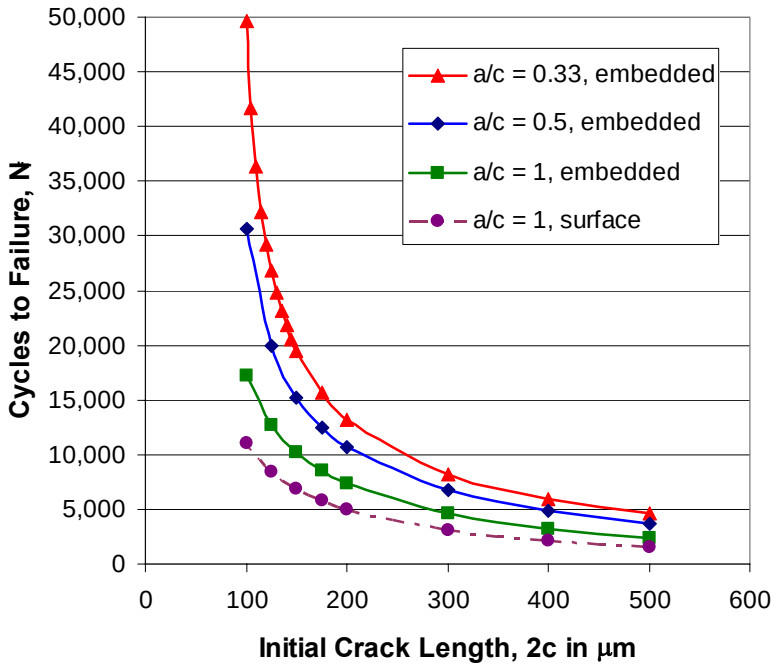

Figure 4.20: AFGROW prediction of worst case cycles to failure for an embedded elliptical flaw at three different a/c ratios and a semielliptical surface flaw at one a/c ratio for Ti64+1B at the stress of 758 MPa.

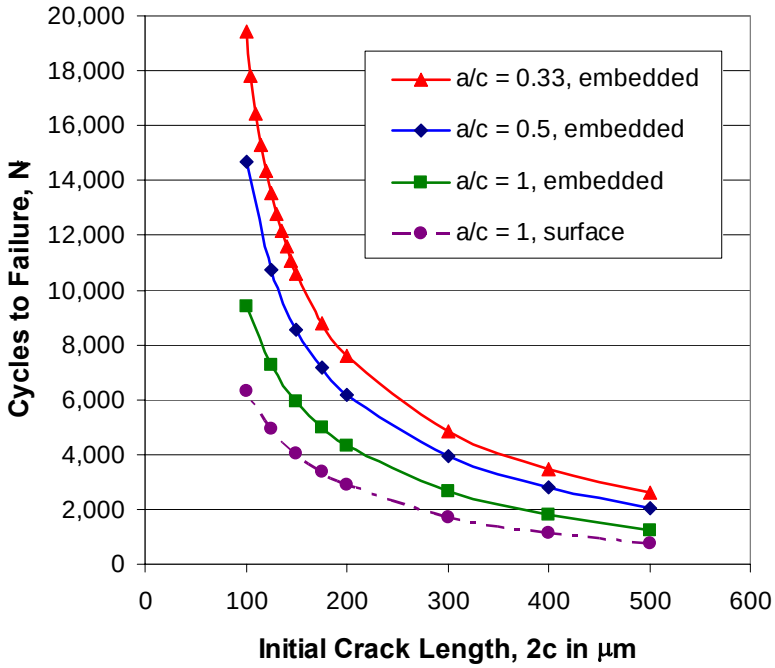

Figure 4.21: AFGROW prediction of worst case cycles to failure for an embedded elliptical flaw at three different a/c ratios and a semielliptical surface flaw at one a/c ratio for Ti64+1B at the stress of 862 MPa.

The S-N fatigue results were placed side by side with the results of the AFGROW analysis in Figures 4.22, 4.23, 4.24, and 4.25 for the three a/c embedded flaw cases and the surface flaw case. From fractography, the dimensions of the lowest life specimen at the middle stress of 758 MPa (labeled in all four figures) were approximately 375 by 225 μm. This equates to a/c = 0.6. This subsurface flaw had a fatigue life of 9,629 cycles. Using Figure 4.23 with a/c = 0.5, a 2c = 300 μm embedded flaw corresponds to an N_f of about 7,000 cycles and a 2c = 400 μm embedded flaw corresponds to an N_f of 5,000 cycles. The prediction using Figure 4.22 with a/c = 1 at the same flaw sizes yields a N_f range of 5,000 down to 3,000 cycles. A worst case result for this flaw at a/c = 0.6 could be interpolated between the a/c = 0.5 and a/c = 1 data. The close enough results of this are analysis show that the FCG analysis using AFGROW has accurately predicted and

captured both the worst case fatigue life and the detrimental effect of the life-limiting damage mechanism: inclusions.

The other data point circled in Figures 4.22, 4.23, 4.24, and 4.25 is for the specimen at the low stress of 655 MPa that failed at 79,720 cycles. Although the result for this specimen is still safely away from the left edge of the digitized envelope, fractography showed that an inclusion near the outside of the specimen caused this specimen to fail. In addition, nearly an order of magnitude separates this data point from the next point at this stress level. The flaw and resulting initiation site had dimensions of approximately 150 μm by 75 μm. Assuming the worst case, an inclusion at the surface, and estimating between the 2c = 200 μm and the 2c = 100 μm curves, the N_f would have been between 10,000 and 20,000 cycles. This is five times less than the actual fatigue life but Figure 4.25 still demonstrates that inclusions allowed by a -35 mesh sieve (up to 500μm) could result in poor life fatigue lives below 10,000 cycles for the Ti64+1B material system.

Clearly, a cleaner Ti64+1B material produced via powder metallurgy using a smaller mesh size would be more competitive for aerospace applications. The current life limiting mechanism's influence on the fatigue lower limit and crack initiation character as well as the risk of premature failure can be substantially reduced. These improvements could be realized by repeating the analysis of this thesis for the next generation Ti64+1B material.

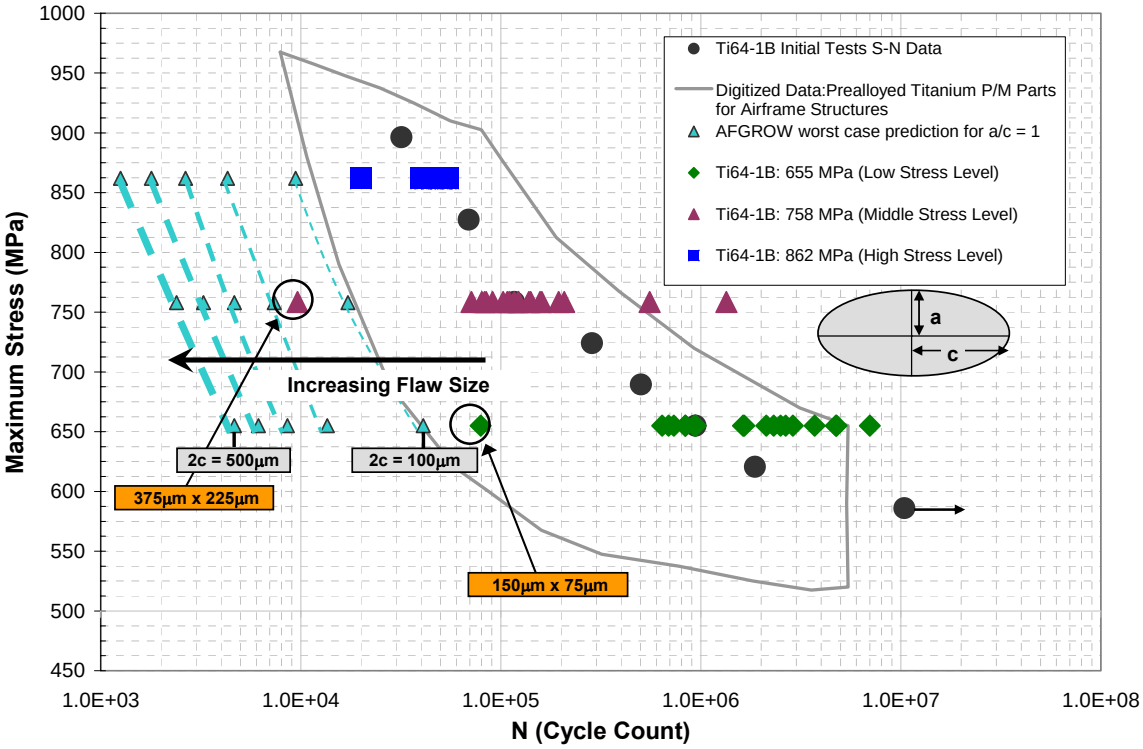

Figure 4.22: Comparison of fatigue variability results with AFGROW's elliptical embedded flaw prediction at a/c = 1.

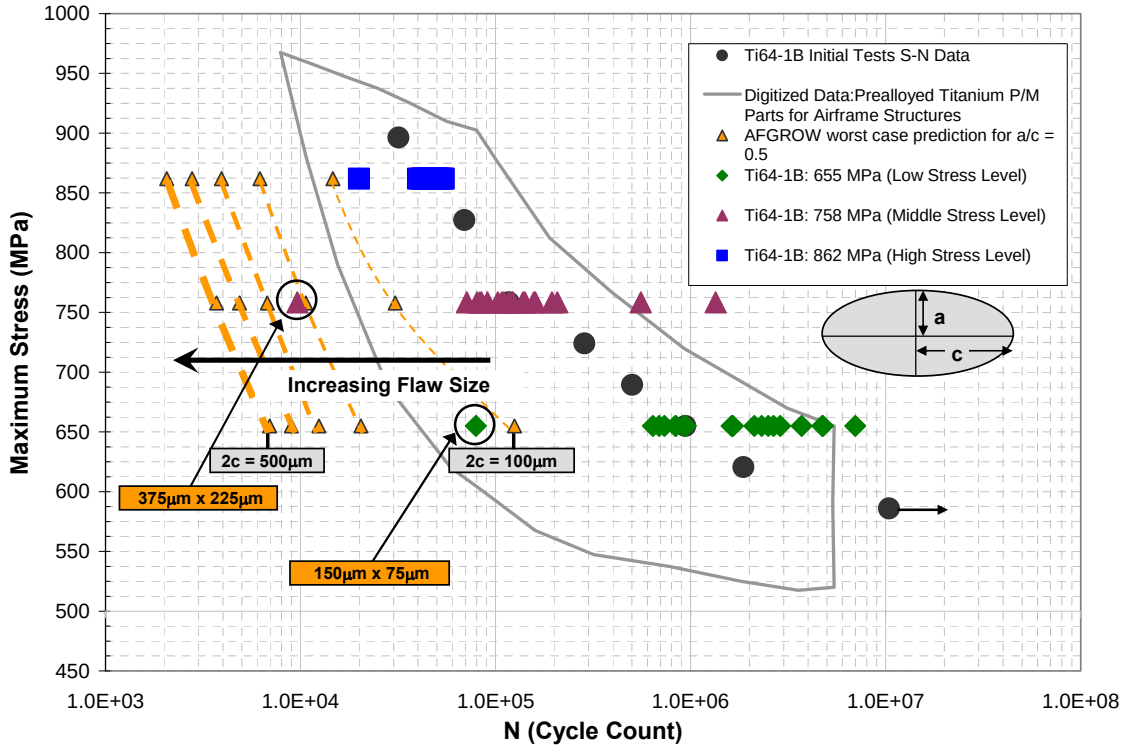

Figure 4.23: Comparison of fatigue variability results with AFGROW's elliptical embedded flaw prediction at a/c = 0.5.

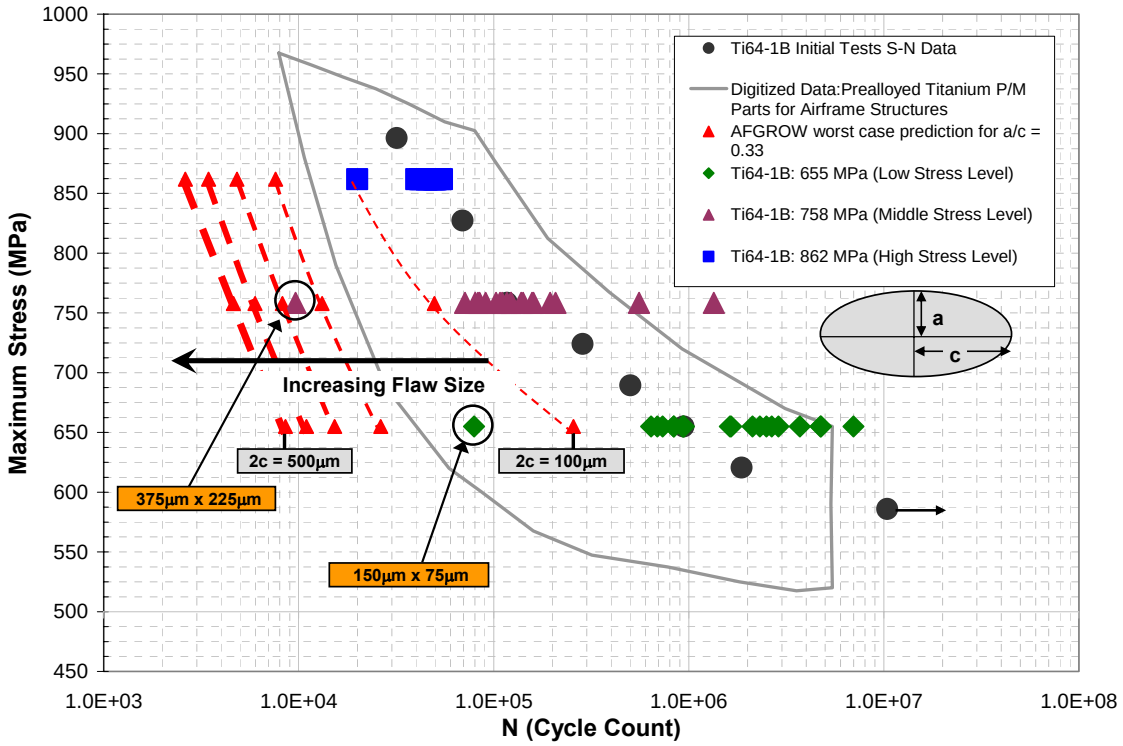

Figure 4.24: Comparison of fatigue variability results with AFGROW's elliptical embedded flaw prediction at a/c = 0.33.

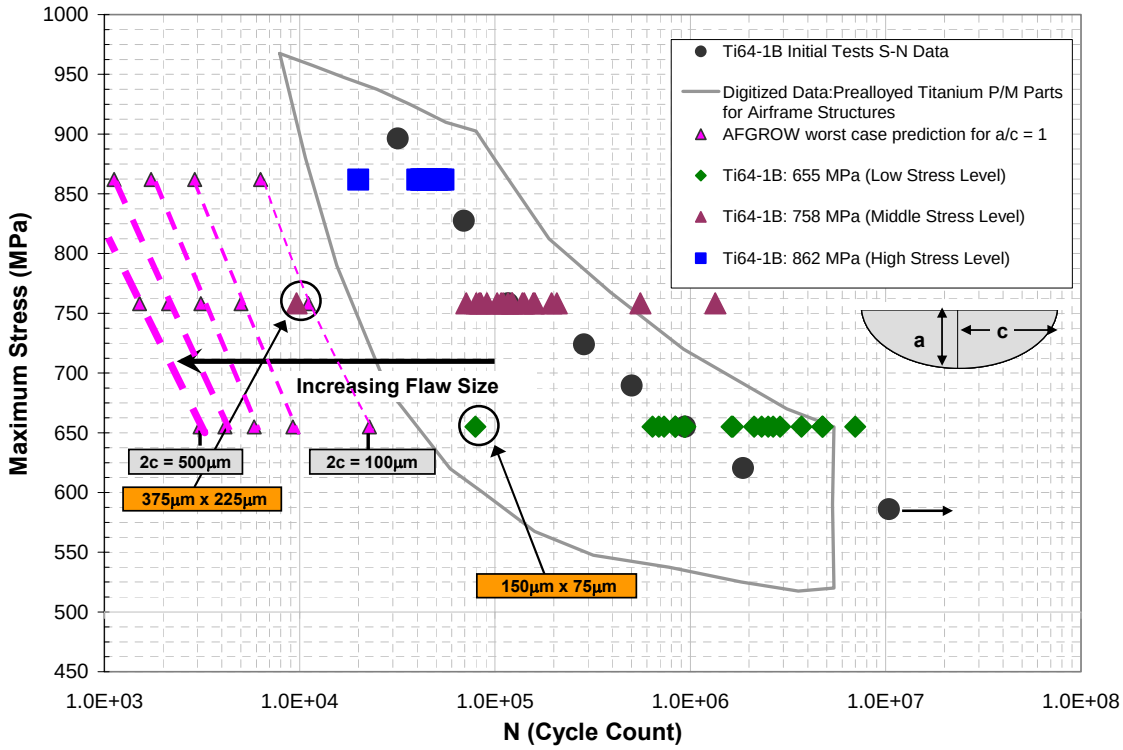

Figure 4.25: Comparison of fatigue variability results with AFGROW's semi-elliptical surface flaw prediction at a/c = 1.

V. Conclusions

The purpose of this research study was to assess the fatigue behavior of novel boron-enhanced Ti-6Al-4V-1B. Emphasis was placed on evaluating the fatigue variability and understanding the mechanisms responsible for the life limiting failures. A stress-cyclic life curve was developed from which three stresses targeting specific life-cycle ranges were chosen. For each maximum stress, 655, 758, and 862 MPa, 20 fatigue tests were performed at a stress ratio of R = 0.1, which established the variability in fatigue life of the Ti64+1B rolled plate material. The overall fatigue life behavior was compared against two credible sources of Ti64 fatigue data. The fracture surfaces of the fatigue specimens were visually inspected to make an initial determination of the mechanisms leading to crack initiation. Fractography and energy dispersive spectroscopy (EDS) analysis were employed on a subset of the fatigue specimens that more thoroughly identified the life limiting mechanism. A compact tension specimen was tested to establish the fatigue crack growth behavior of Ti64+1B. The test was carried out in separate steps: precracking, K-decreasing threshold testing, and constant P_{max} testing. The large quantity of fatigue crack growth data was carefully reduced in several steps and converted to a da/dN versus ΔK crack growth rate curve. The crack growth rate curve was also compared with two credible fatigue crack growth databases. Finally, this entire study was brought full-circle by calculating the worst case cycles to failure at each stress level based solely on fatigue crack growth for varying initial flaw sizes including both elliptical embedded and surface flaw geometries. The calculated fatigue crack growth lifetimes were matched up against the worst case cyclic life results from the fatigue

variability testing. The following conclusions and recommendations resulted from this experimental and analytical study:

- The mean fatigue life and standard deviation in life increased with decreasing stress level. The variability in fatigue life increased with decreasing stress level. Two orders of magnitude of variability were observed at the two lower stresses.
- The overall fatigue life results for the prealloyed powder metallurgy Ti64+1B rolled plate material compared favorably with existing data sets on P/M Ti64 ELI and Ti64 forged plates tested in the USAF HCF program.
- In assessing the overall fatigue performance of Ti64+1B, the worst case scenario was not driven by TiB particles. In the majority of stress-life fatigue tests, including the specimens with subsurface inclusions, most of the life in the test was assumed to have been spent initiating and growing a small crack with little influence of the TiB particles.
- Inclusions were the life limiting mechanisms. Calcium, iron, silicon, and magnesium rich inclusions/foreign matter were the dominant failure initiation mechanisms discovered via fractography and energy dispersive spectroscopy (EDS) analysis of the specimens exhibiting the lowest life fatigue results. These mechanisms culminated in an adjusted lower limit prediction, which was confirmed by using the AFGROW software to predict the crack growth at each of the stress levels from a variety of flaw sizes. The initial flaw sizes were chosen based upon the fractography performed on a subset of all 67 fatigue specimens.
- The outliers will drive the design life of fatigue critical components made with Ti64+1B. Removal of the low outliers, in fact the removal of the life limiting

mechanism of inclusions, should have a significant impact on 0.1% probability of failure. Probability of failure plots created from fatigue variability at the 655 MPa and 758 MPa indicated that filtering out the largest inclusions would potentially double the fatigue life, which in some cases amounts to half an order of magnitude improvement for the worst case fatigue life.

- The fatigue crack growth curve of Ti64+1B, da/dN versus ΔK, compared favorably with the Ti64 databases found in the AFGROW program. The curve for Ti64+1B fell between the curves for the two material databases: AFGROW's Ti64 AMS 4911G Annealed and NASA's Ti64 ELI Forged Plate.
- The crack growth predictions were similar to the lowest life results found in fatigue variability testing. This demonstrated that inclusions allowed by a -35 mesh sieve (500μm) could result in premature fatigue failures for the Ti64+1B material system that would.
- It is recommended that the Ti64+1B be reevaluated using finer starting powder (i.e. sifted using a smaller mesh sieve). The -100 mesh size, for example, would limit powder and maximum flaw size to 150 μm, which is 70% smaller than the size used in this study. A cleaner Ti64+1B alloy would have an improved fatigue lower limit and the variability between the diverging mechanisms of inclusion and non-inclusion flaws would be controlled and probably substantially reduced. It remains to be seen how much the fatigue crack growth behavior would improve.
- This study represents positive results and great potential for many boron modified titanium alloys. It indicates that the time dependent properties of fatigue and

crack growth for Ti64+1B can be at least as good as and probably a little better than baseline Ti64.

Appendix: Fractography

σ = 655 MPa, N_{Low} = 79,270 (Near surface inclusion)

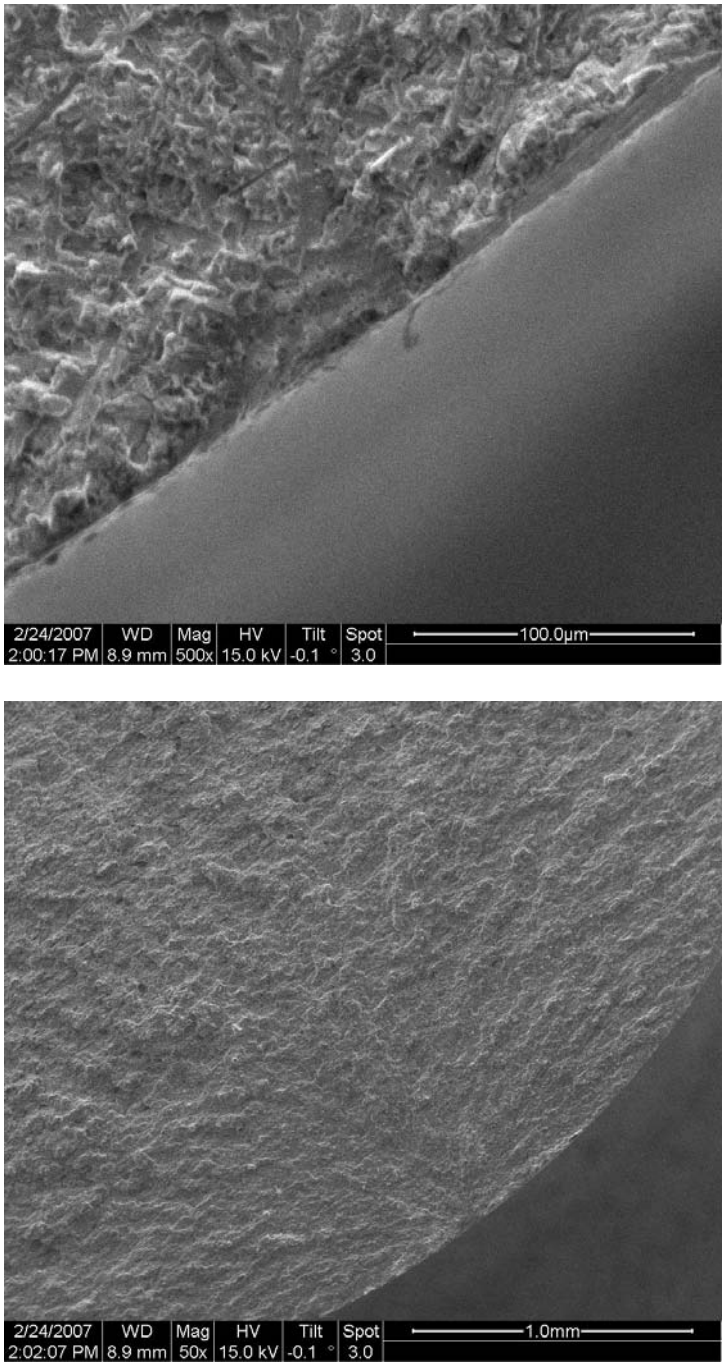

Top - 50x secondary image of specimen fracture surface with inclusion at initiation site near the surface, and bottom-500x close up of surface inclusion. The size of the semielliptical flaw has dimensions of 100 microns by 50 microns.

σ = 655 MPa, N_{Mid} = 640,185 (Inclusion)

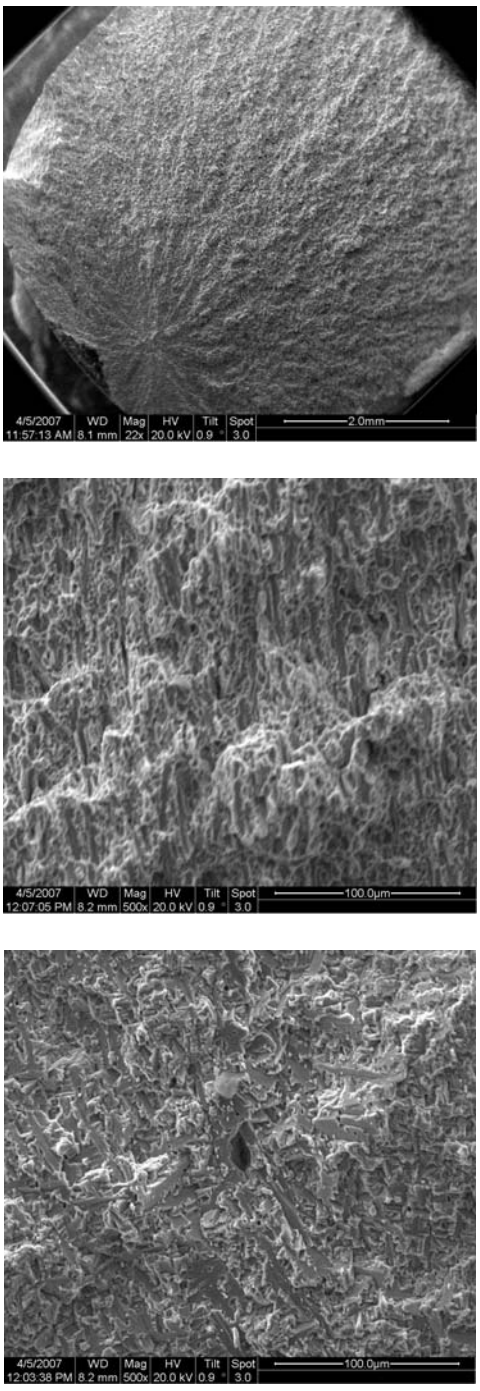

Top – 20x secondary image of specimen fracture surface with inclusion initiation site in lower left corner, middle – secondary image of the flaw at 500x, and bottom – secondary image of the matrix material in the middle of the specimen far away from the initiation site.

σ = 655 MPa, N_{Mid} = 2,122,964 (Inclusion)

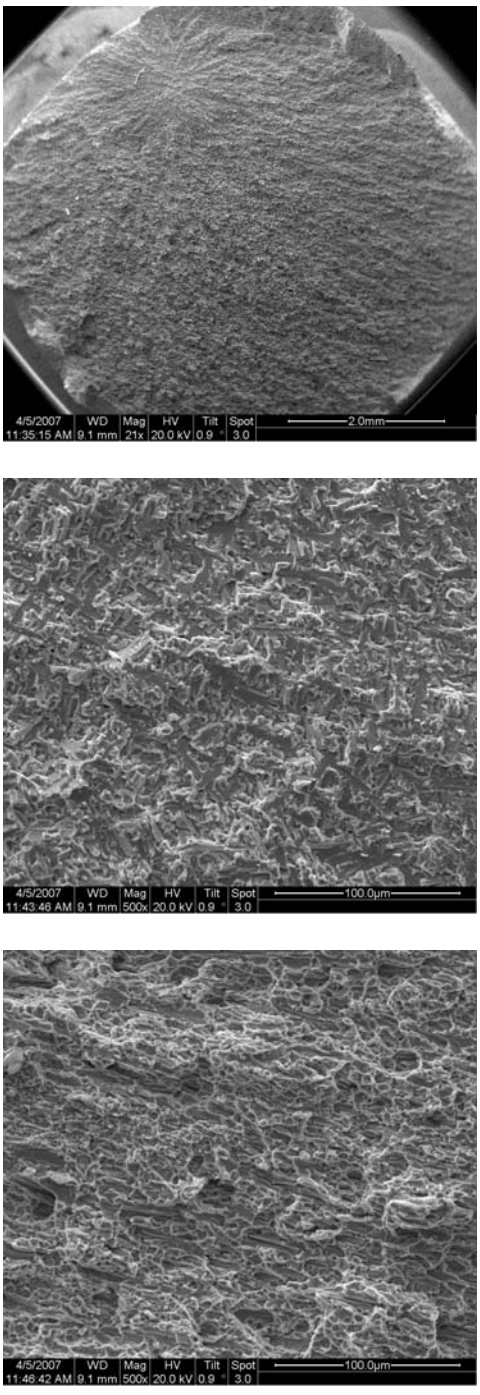

Top - 20x secondary image of specimen fracture surface with inclusion initiation site at the top of the image, middle – secondary image of the flaw at 500x, and bottom – secondary image of the matrix material in the middle of the specimen far away from the initiation site.

σ = 655 MPa, N_{High} = 6,985,294 (Not an inclusion)

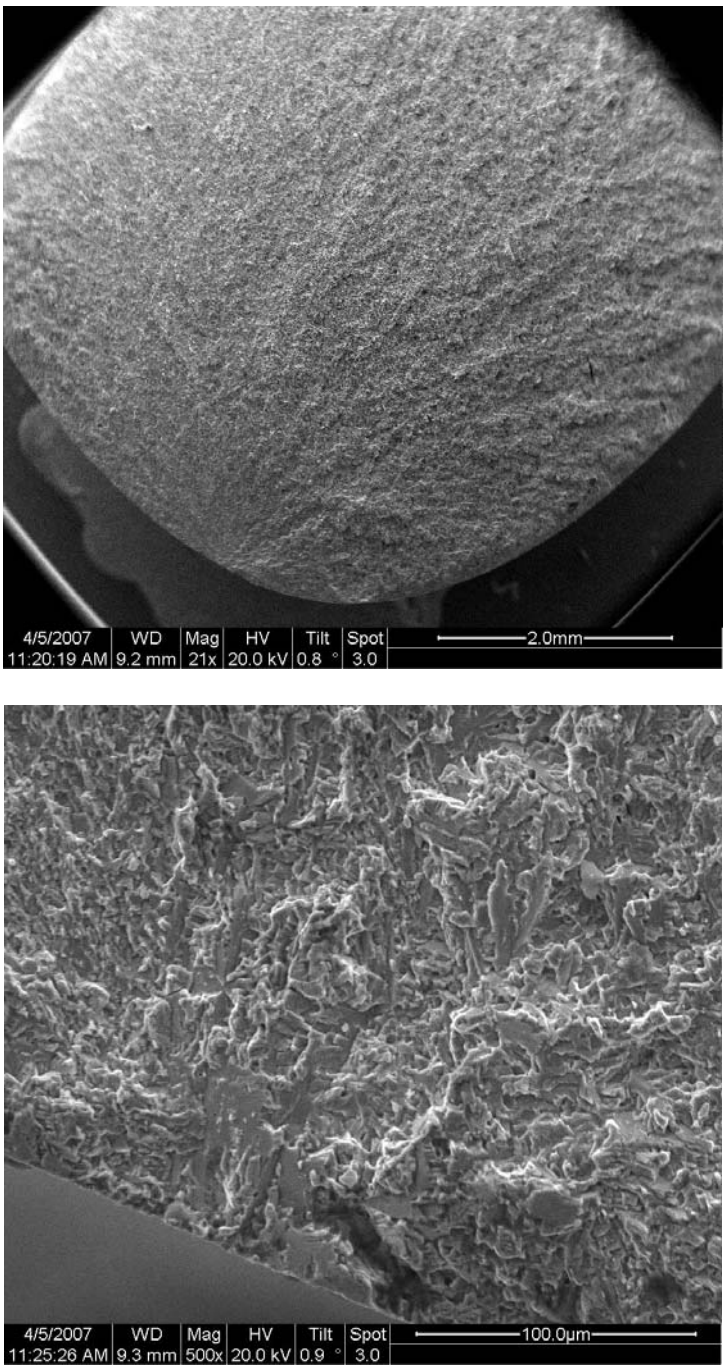

Top - 20x secondary image of specimen fracture surface with non-inclusion failure site at the bottom of the picture, and bottom – secondary image of initiation site near the machined surface of the specimen; for the specimens with non-inclusion crack initiation sites, it was more difficult to find the initiation site and to discover what caused the crack initiation.

σ = 758 MPa, N_{Low} = 9,629 (Inclusion)

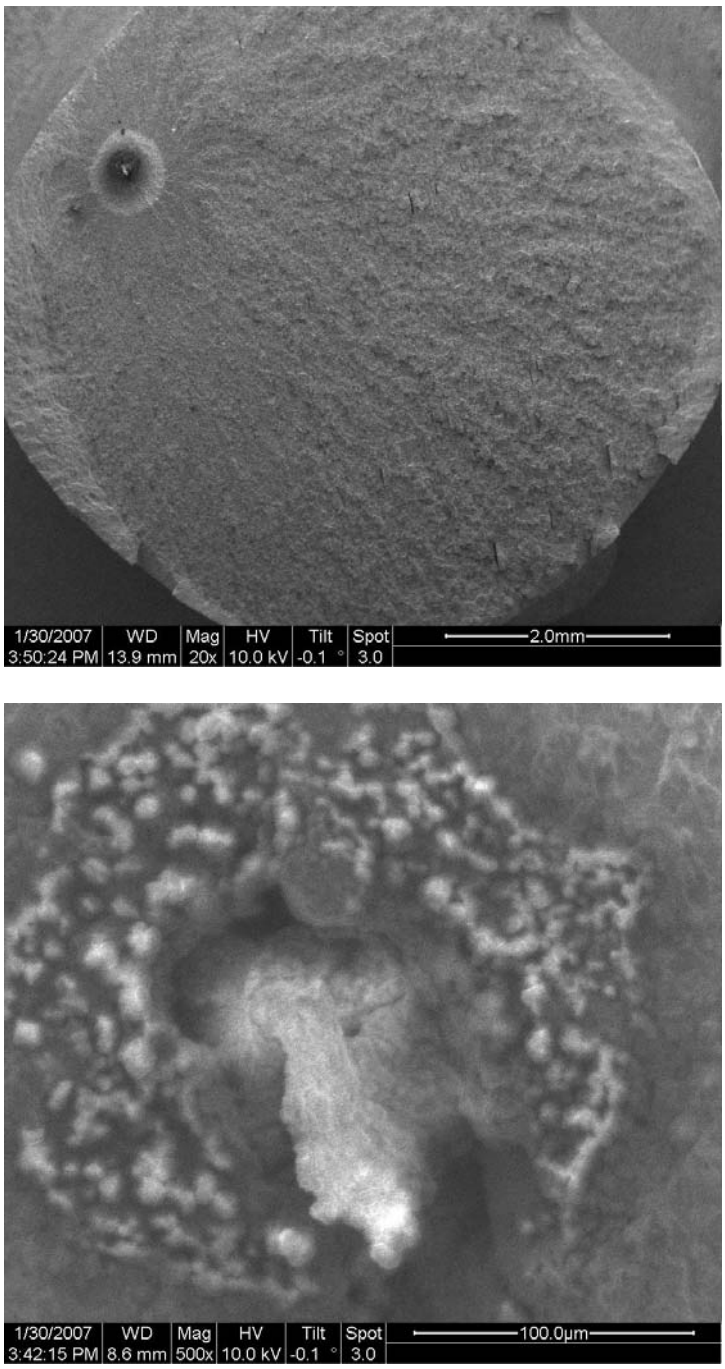

Top – secondary image of the fracture surface with an inclusion in the upper left of the image, and bottom– close up of initiation site at 500x. The energy dispersive spectroscopy (EDS) analysis of this particular inclusion is covered thoroughly in the main body of the thesis.

σ = 758 MPa, N_{Mid} = 194,626 (Not an Inclusion)

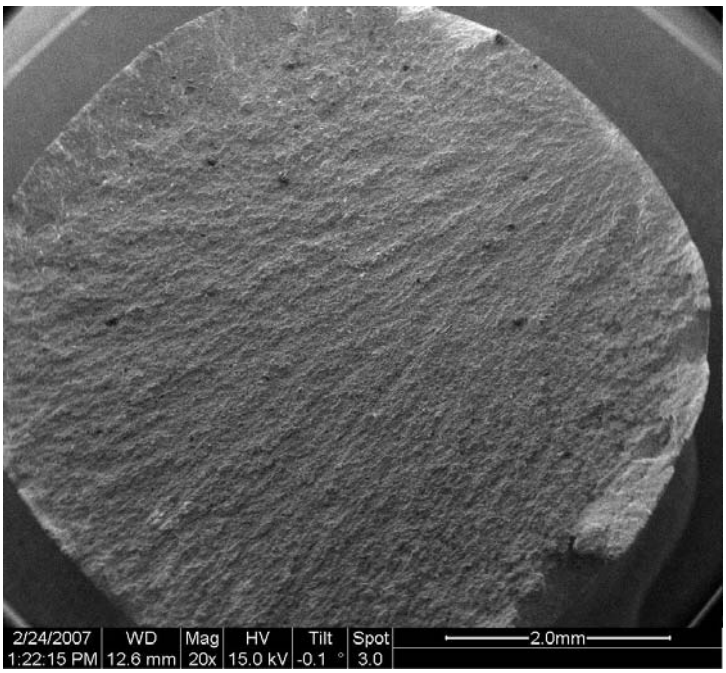

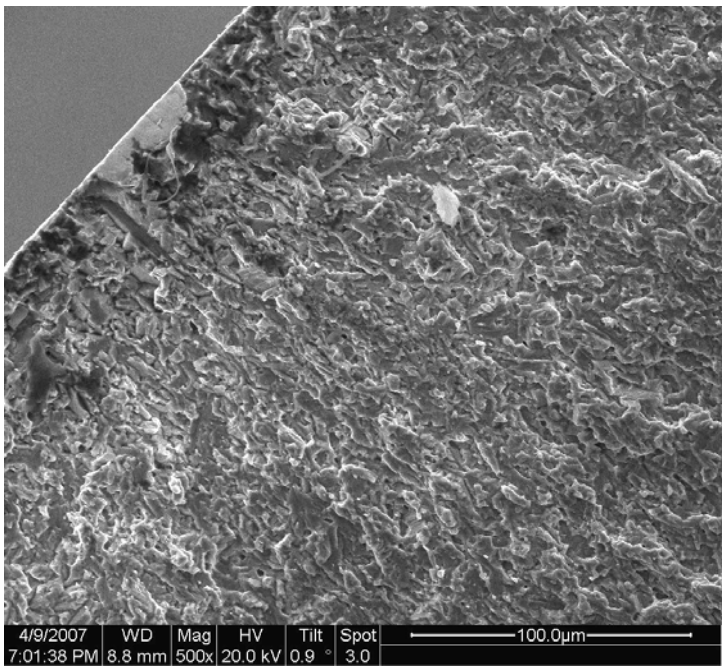

Top - 20x secondary image of specimen fracture surface with non-inclusion failure site at the bottom of the picture, and bottom – secondary image of initiation site near the machined surface of the specimen; for the specimens with non-inclusion crack initiation sites, it was more difficult to find the initiation site and to discover what caused the crack initiation.

σ = 758 MPa, N_{High} = 1,342,920 (Not an Inclusion)

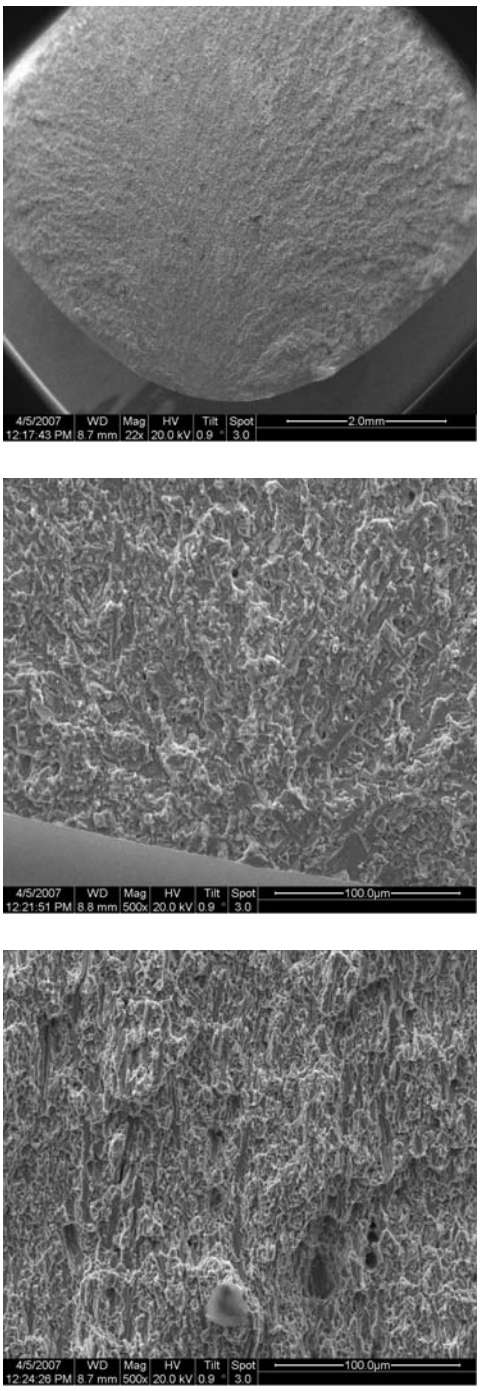

Top - 20x secondary image of specimen fracture surface with non-inclusion failure site at the bottom of the picture, middle – secondary image of initiation site near the machined surface of the specimen, and bottom – view of matrix material specimen away from the crack initiation region; for the specimens with non-inclusion crack initiation sites, it was more difficult to find the site of crack initiation.

σ = 862 MPa, N_{Low} = 19,959 (Inclusion)

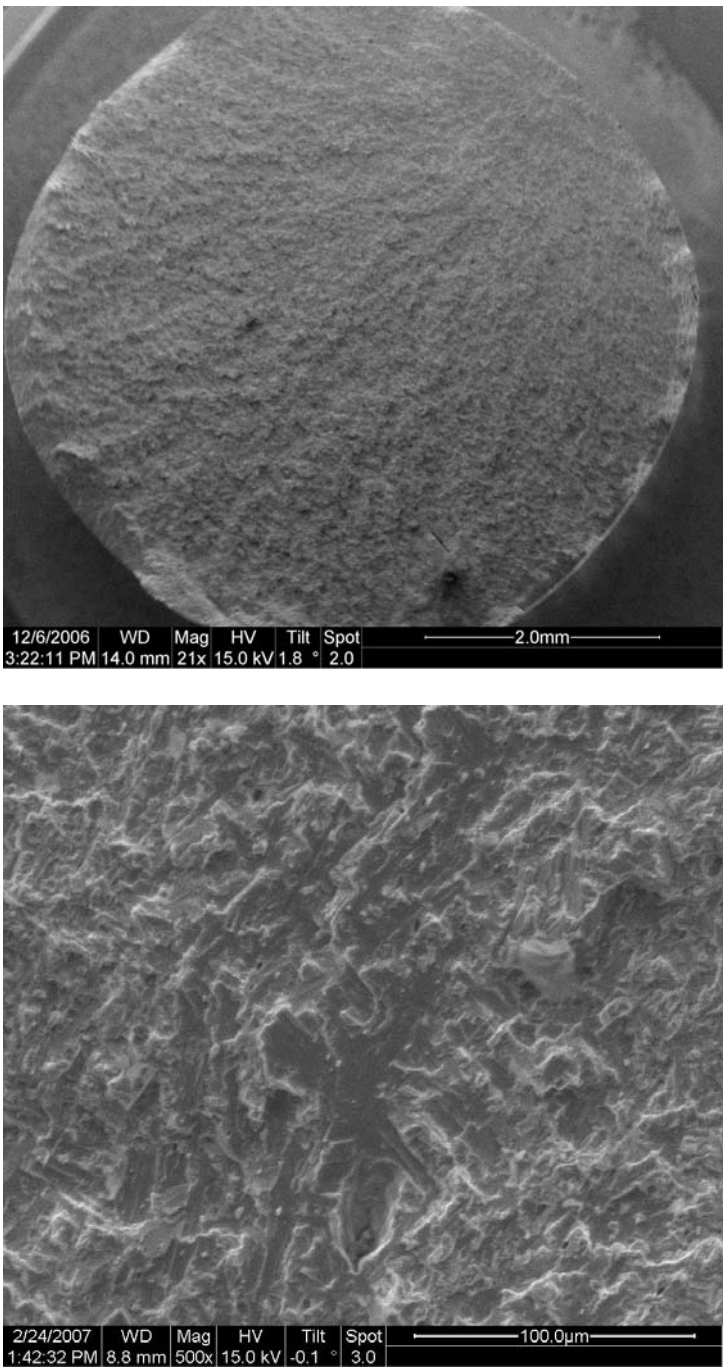

Top- 50x secondary image of specimen fracture surface with inclusion at initiation site at the bottom of the image, and bottom-500x close up of surface inclusion. The size of the elliptical flaw has dimensions no greater than 150 microns by 75 microns.

σ = 862 MPa, N_{Mid} = 46,198 (Not an Inclusion)

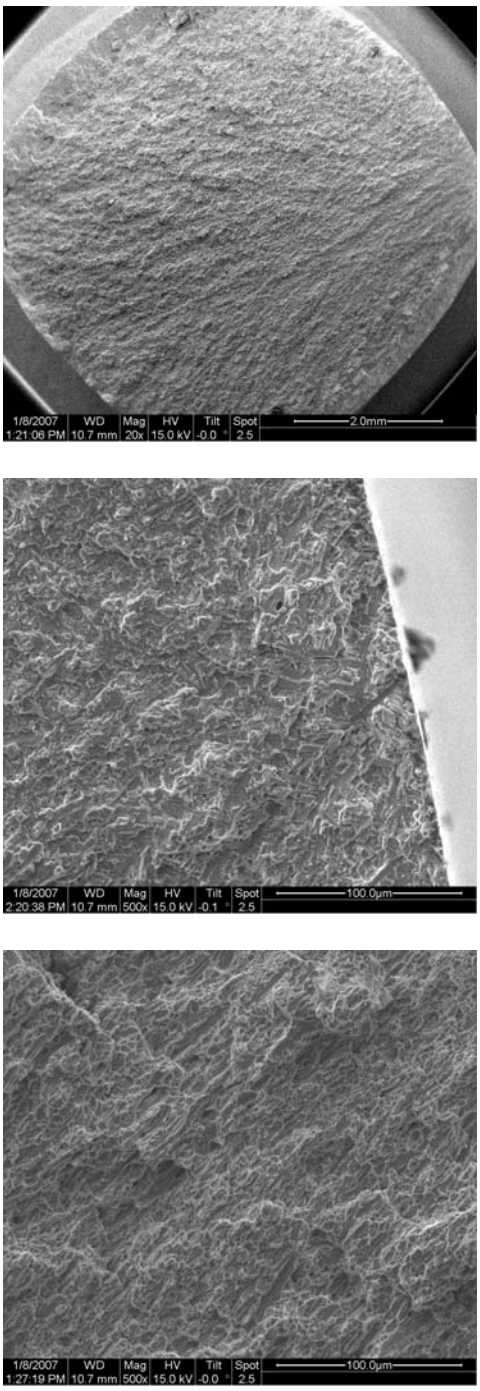

Top - 20x secondary image of specimen fracture surface with non-inclusion failure site on the right side of the image, middle – secondary image of initiation site near the machined surface of the specimen, and bottom – view of matrix material in middle of specimen away from the crack initiation; for the specimens with non-inclusion crack initiation sites, it was more difficult to find the initiation site and to discover what caused the crack initiation.

σ = 862 MPa, N_{High} = 54,434 (Not an Inclusion)

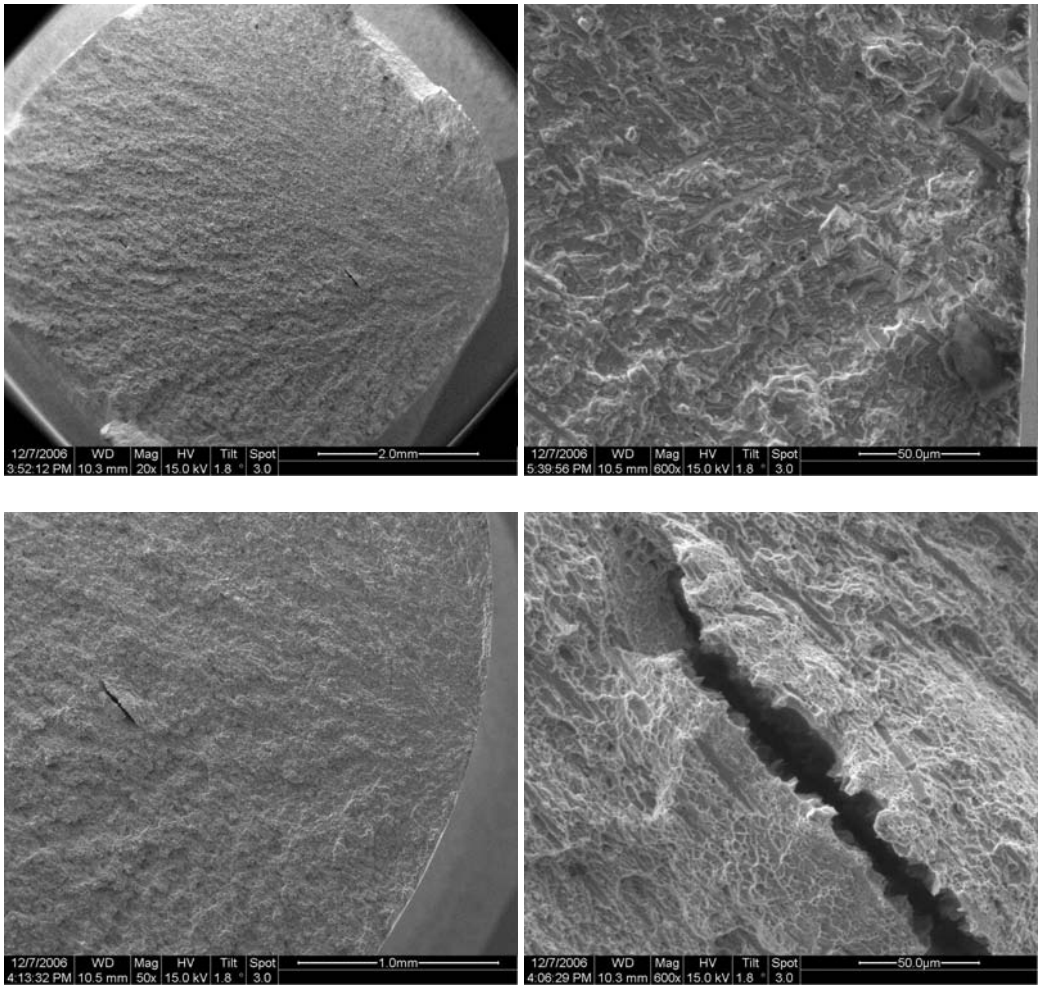

Top left – secondary image at 20x of specimen's fracture surface, top right – 600x view of possible initiation sites on right side of surface, bottom left – 50x image of fracture surface showing closer view of crevice, and bottom right – 600x close up of crack crevice near middle of fracture surface, which, upon careful examination, didn't affect the specimen during the initial crack growth.

σ = 896 MPa, N = 4,485 (Inclusion)

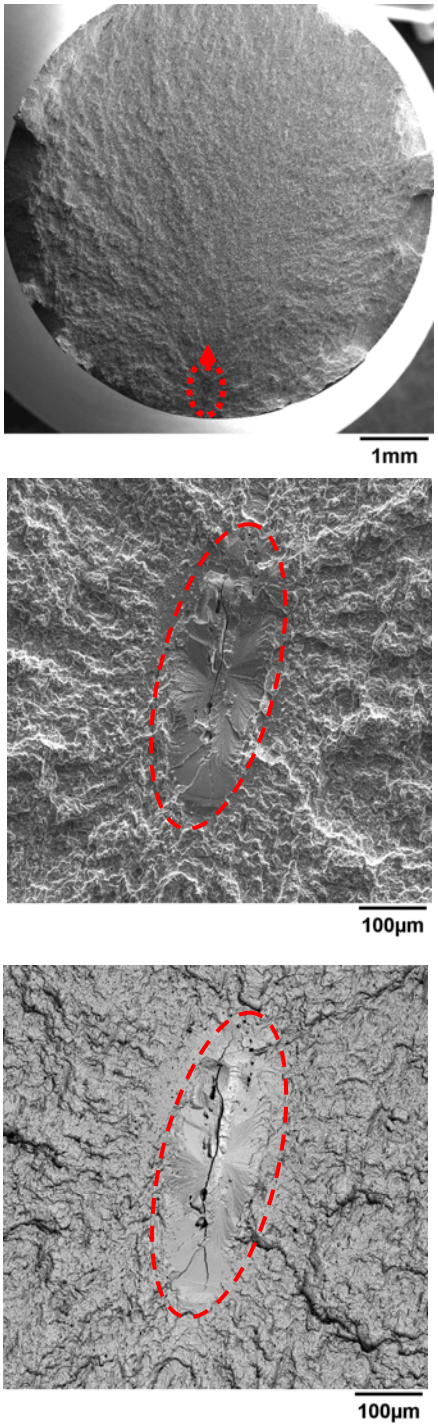

Top – fracture surface of specimen with inclusion at bottom of the 20x image, middle – secondary 1000x image of inclusion flaw measuring near 400 by 200 microns in size, bottom – back-scatter electron 1000x image.

Bibliography

Abkowitz, Susan M. and Stanley Abkowitz. "The Early Development and Recent Achievements in Properties and Applications of TiB Reinforced Titanium Alloy Matrix Composites ." Presentation (CD also available) at *A Workshop on Titanium Alloys Modified with Boron* held at UES, Inc. Dayton, OH. October 11-13, 2005.

Anderson, T.L. *Fracture Mechanics: Fundamentals and Applications* (3rd Edition). Florida: CRC Press, 2005.

Bannantine, Julie A., Jess J. Comer, and James L. Handrock. *Fundamentals of Metal Fatigue Analysis*. New Jersey: Prentice Hall, Inc., 1990.

Bhat, Radhakrishna B. and Daniel B. Miracle. "Hot Working Behavior of a Composite Ti-6Al-4V+20 Vol. % TiB –A Study Using a Processing Map." Presentation at The Materials Society (TMS) Conference held in Columbus, OH, October 7-10, 2002.

Box, George E.P., William G. Hunter, and J. Stuart Hunter. *Statistics for Experimenters*. New York: John Wiley & Sons, Inc., 1978.

Catalog Handbook of Fine Chemicals, 2003-2004. St. Louis, MO, Aldrich Chemical Co., 2002.

Christodoulou, L. and J.M. Larsen. "Materials Damage Prognosis: A Revolution in Asset Management." *Proceedings of a Materials Damage Prognosis symposium sponsored by the Structural Materials Division* (SMD) *of The Minerals, Metals, and Materials Society* (TMS). 3-10. Pennsylvania: TMS, 2005.

Collings, E.W. *The Physical Metallurgy of Titanium Alloys*. Ohio: American Society for Metals, 1984.

Dillon, Tom. "Metals R&D for a supersonic transport - research and development - Aerospace Metals and Materials." *American Metal Market,* 15 April 1991.

Donachie, Matthew J, Jr. *Titanium: A Technical Guide*. Ohio: ASM International, 2000.

Dowling, Norman E. *Mechanical Behavior of Materials*. New Jersey: Prentice-Hall Inc., 1999.

Dubey, S., Y. Li, K. Reece, W.O. Soboyejo, R.J. Lederich. "Fatigue Crack Growth in an In-Situ Titanium Matrix Composite." *Materials Science and Engineering*, A266: 303-309 (1999).

Dynamet Technology, Inc: The CHIP Process. 15 March 2007 http://www.dynamettechnology.com/

E 8—04. "Standard Test Methods for Tension Testing of Metallic Materials." *Annual Book of ASTM Standards*. Philadelphia, PA: ASTM. 2004: 1-24.

E 466—96 (Reapproved in 2002). "Standard Practice for Conducting Force Controlled Constant Amplitude Axial Fatigue Tests of Metallic Materials." *Annual Book of ASTM Standards*. Philadelphia, PA: ASTM. 2002: 541-545.

E 647—00. "Standard Test Method for Measurement of Fatigue Crack Growth Rates." *Annual Book of ASTM Standards*. Philadelphia, PA: ASTM. 2000: 615-627.

Eylon, D., R.E. Omlor, R.J. Bacon, and F.H. Froes. "Morphological and Microstructural Evaluation of Various Titanium Alloy Powders," *Proceedings of a symposium sponsored by the Powder Metallurgy Committee of the The Metallurgical Society of AIME at the 109th AIME annual meeting*. 71-81. New York: American Institute of Mining, Metallurgical, and Petroleum Engineers, Inc., 1980.

Eylon, D., Y. Mahajan, N.R. Ontko, and F.H. Froes. "Fatigue Crack Initiation of Titanium Alloy Powder Compacts," *Proceedings of a symposium sponsored by the Powder Metallurgy Committee of the The Metallurgical Society of AIME at the 109th AIME annual meeting*. 93-102. New York: American Institute of Mining, Metallurgical, and Petroleum Engineers, Inc., 1980.

Forman, R.G., and S.R. Mettu, "Behavior of Surface and Corner Cracks Subjected to Tensile and Bending Loads in Ti-6Al-4V Alloy," Fracture Mechanics 22nd Symposium, Vol. 1, ASTM STP 1131, H.A. Ernst, A. Saxena and D.L. McDowell, eds., American Society for Testing and Materials, Philadelphia, 1992.

Froes, F.H. and D. Eylon. "Powder Metallurgy of Ti Alloy." *Int. Mat. Rev.*, Vol. 35 (No.3), 1990.

Gallagher, J. and T. Nicholas (Program Managers) et al. *Advanced High Cycle Fatigue Life Assurance Methodologies*. Final Report for USAF Contract F49620-99-C-0007. University of Dayton Research Institute, Dayton, OH: July 2004.

Gorsse, Stefan and Daniel B. Miracle. "Mechanical properties of Ti-6Al-4V/TiB composites with randomly oriented and aligned TiB reinforcements", *Acta Materialia*, 51: 2427-2442 (2003) .

Government Contract No. NASI-20220. *High Speed Research-Airframe Technology Report: Airframe Materials & Structures-4.2, 4.2.1.1 Metallic Materials*. Yearly Report: Data Package to Support Selection of Alternative Alloys, Principally High Modulus Materials – Extrusion Applications. Prepared by the McDonnel Douglas Corporation for the Boeing Company, Seattle, WA. 1997:1-26.

Harter, James A. "AFGROW User's Guide and Technical Manual, Version 4.0011.14, Final Report," AFRL-VA-WP-TR-2006-XXXX, Air Vehicles Directorate, Air Force Research Laboratory, Air Force Materiel Command, Wright-Patterson, AFB, 22 June 2006.

Harter, James A., "MODGRO Users manual, Version 1.2, Technical Memorandum," AFWAL-TM-88-157-FIBE, AFWAL Flight Dynamics Laboratory, Wright-Patterson AFB, OH, Revised in July 1994.

Hertzberg, Richard W. *Deformation and Fracture Mechanics of Engineering Materials*. New York: John Wiley & Sons, Inc., 1983.

International Patent Application of Miracle, et al for "Titanium Alloy Microstructural Refinement Method and High Temperature, High Strain Rate Superplastic Forming of Titanium Alloys." Filed in the United States Receiving Office on December 13, 2004. Serial No.: 60/528,660. 1-36.

Jha, S.K., M.J. Caton, J.M. Larsen, A.H. Rosenberger, K. Lhi, and W.J. Porter. "Superimposing Mechanisms and Their Effect on the Variability in Fatigue Lives of a Nickel-based Superalloy." *Proceedings of a Materials Damage Prognosis symposium sponsored by the Structural Materials Division* (SMD) *of The Minerals, Metals, and Materials Society* (TMS). 343-350. Pennsylvania: TMS, 2005.

Jha, S.K., J.M. Larsen, A.H. Rosenberger, and C. Annis. "Prediction of the Worst-Case Fatigue Failures in $\alpha+\beta$ Titanium Alloy." *Proceedings of a Materials Damage Prognosis symposium sponsored by the Structural Materials Division* (SMD) *of The Minerals, Metals, and Materials Society* (TMS). 143-150. Pennsylvania: TMS, 2005.

Jha, S.K., J.M. Larsen, A.H. Rosenberger, and G.A. Hartman. "Dual Fatigue Failure Modes in Ti-6Al-2Sn-4Zr-6Mo and Consequences on Probabilistic Life Prediction." *Scripta Materialia*, 48: 1637-1642 (2003).

Jha, S.K., J.M. Larsen, and A.H. Rosenberger. "The Role of Competing Mechanisms in the Fatigue Life Variability of a Nearly Fully-Laminar γ-TiAl Based Alloy." *Acta Materialia*, 53: 1293-1304 (2005).

Jha, S.K., J.M. Larsen, and A.H. Rosenberger. "The Role of Fatigue Variability in Life Prediction of an α+β Titanium Alloy," *Proceeding of the 8th International Conference on Numerical Methods in Industrial Forming Processes sponsored by the American Institute of Physics (AIP)*. 1955-1960. New York: AIP, June, 2004.

Kelto, C.A., B.A. Kosmal, D. Eylon, and F.H. Froes. "Titanium Powder Metallurgy: A Perspective," *Proceedings of a symposium sponsored by the Powder Metallurgy Committee of the The Metallurgical Society of AIME at the 109th AIME annual meeting*. 1-19. New York: American Institute of Mining, Metallurgical, and Petroleum Engineers, Inc., 1980.

Kalpakjian, Serope and Steven R. Schmid. *Manufacturing Engineering and Technology* (Fourth Edition). New Jersey: Prentice Hall, 2001.

Lieberman, Scott, Arun Sreeranganathan, Harpreet Singh, Yuxiong Mao, Arun Gokhale, and Sesh Tamirisakandala. "Development of Materials Design Methodologies for Boron-Modified Ti-6Al-4V Alloys." Presentation at *The 138th Annual Meeting and Exhibition of the Minerals, Metals, and Materials Society* (TMS) held in Orlando, FL. February 25 to March 1, 2007.

Luetjering, G. "Influence on Microstructure and Mechanical Properties of (α+β) Titanium Alloys." *Materials Science and Engineering*, A243: 32-45. (1998).

McEldowney, Dale. *Heat Treatment Study of Titanium-Boron Alloys and Thermal Stability of the TiB Phase*. PhD Dissertation, University of Dayton, Dayton, OH, 2006.

Miracle, Daniel B., Sesh Tamirisakandala, Radhakrishna B. Bhat, Raghu Srinivasan, and Kevin Schwendiman. "Ti-B Alloy Technology: An Introduction and Overview." Presentation (CD also available) at *A Workshop on Titanium Alloys Modified with Boron* held at UES, Inc. Dayton, OH. October 11-13, 2005.

Peebes, R.E. and C.A. Kelto. "Investigation of Methods for the Production of High Quality, Low Cost Titanium Alloy Powders," *Proceedings of a symposium sponsored by the Powder Metallurgy Committee of the The Metallurgical Society of AIME at the 109th AIME annual meeting*. 51-58. New York: American Institute of Mining, Metallurgical, and Petroleum Engineers, Inc., 1980.

Peters, Manfred, Joerg Kumpfert, Charles H. Ward, and Christoph Leyens. "Titanium Alloys for Aerospace Applications," *Advanced Engineering Materials*, 6: 419-427 (2003).

Polasik, A.K., S.K. Jha, M.J. Millis, J.M. Larsen, and H.L. Fraser "The Role of Microstructure on Fatigue Life Variability in β-Processed Ti-6Al-4V."

Proceedings of a Materials Damage Prognosis symposium sponsored by the Structural Materials Division (SMD) *of The Minerals, Metals, and Materials Society* (TMS). 121-128. Pennsylvania: TMS, 2005.

Russ, Stephan M. "Effect of LCF on HCF Crack Growth of Ti-17." *International Journal of Fatigue*, 27: 1628-1635 (August 2005).

Saito, Takashi. "The Automotive Application of Discontinuously Reinforced TiB-Ti Composites," *Journal of Metals*, 33-36 (May 2003).

Shademan, S., A.B.O. Soboyejo, J.F. Knott, and W.O. Soboyejo. "A Physically-Based Model for the Prediction of Long Fatigue Crack Growth in Ti-6Al-4V." *Materials Science and Engineering*, A315: 1-10 (2001).

Soboyejo, W.O., R.J. Lederich, T.S. Srivatsan, and K. Reece. "Mechanical Properties of Damage Tolerant TiB Whisker Reinforced In-Situ Titanium Matrix Composites," *Proceedings of a symposium on Intrinsic and Extrinsic Fracture Mechanisms in Inorganic Composite Systems symposium sponsored by The Minerals, Metals, and Materials Society* (TMS). 167-182. Pennsylvania: TMS, 1995.

Soboyejo, W.O., W. Shen, and T.S. Srivatsan. "An Investigation of Fatigue Crack Nucleation and Growth in a Ti-6Al-4V/TiB In Situ Composite." *Mechanics of Materials*, 36:141-159 (2004).

Tamirisakandala, S., RadhakrishnaB Bhat, V.A. Ravi, and Daniel B. Miracle. "Powder Metallurgy Ti-6Al-4V-xB Alloys: Processing, Microstructure, and Properties," *Journal of Metals*, 60-63 (May 2003).

Tamirisakandala, S. "Rolling of Ti64-1B Plates." Presentation given at FMW Composites, Inc., April 2006.

Yolton, Fred. "The Pre-Alloyed Powder Metallurgy of Titanium with Boron and Carbon Additions." *Journal of Metals*, 56-59 (May 2003).

Yolton, Fred. "Atomization of Titanium Alloys Containing Boron." Presentation at *The 138th Annual Meeting and Exhibition of the Minerals, Metals, and Materials Society* (TMS) held in Orlando, FL. February 25 to March 1, 2007.

Vita

Lieutenant Kevin A. Schwendiman graduated from East Greenwich High School in East Greenwich, RI in 1997. Following a fourth summer on staff at a local scout camp that same year, he began undergraduate studies at Brigham Young University (BYU) in Provo, Utah. From May 1998 to May 2000, Lt Schwendiman deferred his education to serve as a missionary for the Church of Jesus Christ of Latter Day Saints in the Duesseldorf, Germany area. He returned to BYU immediately after his mission and graduated with a Bachelor of Science degree in Mechanical Engineering in April 2003. Lt Schwendiman complemented his graduation from BYU with University Honors distinction, placing him in the top 1% of 6000+ graduates in the year 2003. He applied for Air Force Officer Training School after graduation.

Lt Schwendiman was commissioned as a second lieutenant in the United States Air Force in May 2004 and was assigned to the Air Force Research Laboratory's (AFRL) Materials and Manufacturing Directorate at Wright-Patterson Air Force Base (WPAFB) where he works presently as a program manager and researcher for up-and-coming Titanium Composite Materials. Seeing an opportunity to push his career and make a greater impact, Lt Schwendiman qualified for the DAGSI scholarship and enrolled part time at the Air Force Institute of Technology in the Graduate School of Engineering in October 2004. Upon graduation with a Master's Degree in Aeronautical Engineering, he will continue to work at AFRL while pursuing further program management, research, and educational opportunities.

REPORT DOCUMENTATION PAGE

Form Approved
OMB No. 074-0188

1. REPORT DATE *(DD-MM-YYYY)*	**2. REPORT TYPE**	**3. DATES COVERED** *(From – To)*
14 Jun 07	**Master's Thesis**	**– Jun 2007**

4. TITLE AND SUBTITLE

Critical Life Prediction Research on Boron-enhanced Ti-6Al-4V

5a. CONTRACT NUMBER

5b. GRANT NUMBER

5c. PROGRAM ELEMENT NUMBER

6. AUTHOR(S)

Schwendiman, Kevin A., First Lieutenant, USAF

5d. PROJECT NUMBER

5e. TASK NUMBER

5f. WORK UNIT NUMBER

7. PERFORMING ORGANIZATION NAMES(S) AND ADDRESS(S)
Air Force Institute of Technology
Graduate School of Engineering and Management (AFIT/EN)
2950 Hobson Way
WPAFB OH 45433-7765

8. PERFORMING ORGANIZATION REPORT NUMBER

AFIT/GAE/ENY/07-J24

9. SPONSORING/MONITORING AGENCY NAME(S) AND ADDRESS(ES)
AFRL/MLLMD
Attn: Dr. Stephan M. Russ
2230 10th St, Bldg. 655, Rm. 72
Wright-Patterson AFB OH 45433 DSN: 785-1356

10. SPONSOR/MONITOR'S ACRONYM(S)

11. SPONSOR/MONITOR'S REPORT NUMBER(S)

12. DISTRIBUTION/AVAILABILITY STATEMENT
APPROVED FOR PUBLIC RELEASE; DISTRIBUTION UNLIMITED.

13. SUPPLEMENTARY NOTES

14. ABSTRACT

Research on boron-enhanced Ti-6-4 has demonstrated the following improvements to the Ti-6-4 alloy: up to 40% increase in ultimate tensile strength, up to 30% increase in modulus/stiffness, while maintaining greater than 10% ductility at RT conditions. The increased properties are attributed to small additions of boron (≤1 wt %), which refine the microstructure and result in a small volume fraction (~6 vol %) of fine TiB whiskers. Previous research indicates potential for substantial improvements in fatigue, fatigue crack growth, and fracture toughness. However, uncertainty regarding these "second-tier" mechanical properties is currently limiting implementation of this class of titanium alloys. This study of fatigue variability of a powder-metallurgy, boron-enhanced Ti-6-4 alloy identifies the most prevalent damage mechanism and elucidates the impact on fatigue design limits. The alloy was produced via a unique prealloyed powder-metallurgy process. The powder mesh size used was -35, which equates to powder particles with a diameter of 500 μm and smaller. Specimens were ultimately machined from a rolled plate. The mean fatigue behavior compared favorably with available data on conventional Ti-6-4, both wrought and powder-metallurgy product forms. However, inclusions in the material were responsible for a few poor fatigue results, which ultimately govern the fatigue design limits. Variability assessment and fatigue crack growth analyses indicate that if the frequency and size of inclusions can be reduced, this material could become a more viable alternative for select turbine engine and aircraft applications.

15. SUBJECT TERMS
Ti-6Al-4V, discontinuous titanium matrix composites, titanium alloys, mechanical properties, fatigue variability, fatigue stress life, fatigue crack growth, powder metallurgy, aircraft applications, damage mechanism, fractography, lower limit prediction

16. SECURITY CLASSIFICATION OF:			**17. LIMITATION OF ABSTRACT**	**18. NUMBER OF PAGES**	**19a. NAME OF RESPONSIBLE PERSON**
REPORT	**ABSTRACT**	**c. THIS PAGE**			Dr. Shankar Mall (AFIT/ENY)
U	**U**	**U**	**UU**	142	**19b. TELEPHONE NUMBER** *(Include area code)* (937) 255-3636, ext 4587; e-mail: Shankar.Mall@afit.edu

Standard Form 298 (Rev: 8-98)
Prescribed by ANSI Std. Z39-18